ISSN 2074-272X

науково-практичний журнал

2020/1

Електротехніка і Електромеханіка

Electrical Engineering & Electromechanics

Електричні машини та апарати
Теоретична електротехніка та електрофізика
Техніка сильних електричних та магнітних полів. Кабельна техніка
Електричні станції, мережі і системи
Електричний транспорт

З 2015 р. журнал індексується у міжнародній наукометричній базі Web of Science Core Collection: Emerging Sources Citation Index

«ELECTRICAL ENGINEERING & ELECTROMECHANICS»

SCIENTIFIC & PRACTICAL JOURNAL
Journal was founded in 2002
Founders:
National Technical University «Kharkiv Polytechnic Institute» (Kharkiv, Ukraine)
State Institution «Institute of Technical Problems of Magnetism of the NAS of Ukraine» (Kharkiv, Ukraine)

ISSUE 1 / 2020

TABLE OF CONTENTS

Editorial office address: Dept. of Electrical Apparatus, NTU «KhPI», Kyrpychova Str., 2, Kharkiv, 61002, Ukraine
phones: +380 57 7076281, +380 67 3594696, **e-mail:** a.m.grechko@gmail.com (**Grechko O.M.)**

ISSN (print) 2074-272X
ISSN (online) 2309-3404

Printed 19 February 2020. Format 60 x 90 ⅛. Paper – offset. Laser printing. Edition 200 copies.
Printed by Printing house «Madrid Ltd» (18, Gudanova Str., Kharkiv, 61024, Ukraine)

UDC 621.3.04: 621.316 **doi: 10.20998/2074-272X.2020.1.01**

E.I. Baida, V.V. Lytvynenko, A.A. Chepeliuk

PECULIARITIES OF DYNAMICS OF A FAST-DRIVEN INDUCTION-DYNAMIC DRIVE WITH A BISTABLE LATCH OF CONTACTS POSITION OF A CIRCUIT BREAKER BASED ON PERMANENT MAGNETS

Introduction. Recently, in the literature, inductive-dynamic mechanisms (IDMs), known in foreign literature as a Thomson-drive, as a drive for various electrical devices are often researched and developed. The simplicity and reliability of the design, high speed make such devices indispensable in high-speed electrical devices standing in DC networks, in which emergency overcorrects are not limited by the reactance and can reach significant values. The novelty of the proposed work consists in the development of a mathematical model and the study of the Thompson drive, in which a bistable two-position mechanism consisting of a magnetic system with permanent magnets, is used as the final position latches. The movement of objects is carried out by deforming the computational mesh. The problem is a multiphysical one, in which a parallel solution of several tasks of different nature is considered. Purpose. Analysis of the fundamental possibility of creating a switching device with an induction-dynamic drive on the basis of a mathematical model which allows to increase the reliability of the entire mechanism operation and significantly simplify the design. Methods. The solution of the problem was carried out by the Finite Element Method in the COMSOL package in a cylindrical coordinate system. Results. A mathematical model of a new fast-driven induction-dynamic drive with a bistable mechanism, based on the equations of the electromagnetic field, electric circuit, equations of motion, was developed and partially studied. The model allows to calculate the dynamic parameters of the drive based on the initial data. Conclusions. The principal possibility of creating a high-speed actuator of switching devices based on an induction-dynamic mechanism and a polarized bistable mechanism based on permanent magnets is demonstrated. The research directions of the model were determined for the subsequent implementation of the results in experimental samples. References 11, table 1, figures 13.
Key words: **induction-dynamic drive, bistable latch, permanent magnets.**

У статті досліджено оригінальну математичну модель швидкодіючого індукційно-динамічного приводу вимикача з бістабільним фіксатором з двома котушками на базі постійних магнітів. Індукційно-динамічні механізми, відомі в іноземній літературі як Thomson-drive, використовуються в якості приводу вимикачів постійного струму завдяки високій швидкодії, простоті і надійності конструкції. Метою статті є аналіз принципової можливості створення комутаційного апарату з індукційно-динамічним приводом на базі математичної моделі, що дозволяє підвищити надійність роботи всього механізму і істотно спростити конструкцію. Розглядається можливість створення пропонованого комбінованого приводного механізму і визначення основних напрямків подальших досліджень з метою отримання дослідних зразків. Конструкція досліджуваного індукційно-динамічного приводу раніше в літературі не розглядалась. Вирішувана задача є мультифізичною, що включає розрахунок: статичного магнітного поля; електричного кола з урахуванням зміни напруги на конденсаторі і наведеної в котушках проти-ЕРС; динаміки руху якорів бістабільного фіксатора і привода з урахуванням зміни маси; нестаціонарного електромагнітного поля в неоднорідному нелінійному середовищі з урахуванням постійних магнітів і руху струмопровідних тіл в електромагнітному полі. Напрямки подальших досліджень представляються у вигляді оптимізації геометрії, параметрів котушок привода і конденсаторів, геометрії бістабільного фіксатора, об'єму і залишкової індукції постійних магнітів для забезпечення необхідних значень швидкодії, контактного натискання і габаритів апарата. Бібл. 11, табл. 1, рис. 13.
Ключові слова: **індукційно-динамічний привод, бістабільний фіксатор, постійні магніти.**

В статье исследована оригинальная математическая модель быстродействующего индукционно-динамического привода выключателя с бистабильным фиксатором с двумя катушками на базе постоянных магнитов. Индукционно-динамические механизмы, известные в иностранной литературе как Thomson-drive, применяются в качестве привода выключателей постоянного тока благодаря высокому быстродействию, простоте и надежности конструкции. Целью статьи является анализ принципиальной возможности создания коммутационного аппарата с индукционно-динамическим приводом на базе математической модели, что позволяет повысить надежность работы всего механизма и существенно упростить конструкцию. Рассматривается возможность создания предлагаемого комбинированного приводного механизма и определение основных направлений дальнейших исследований с целью получения опытных образцов. Конструкция исследуемого индукционно-динамического привода ранее в литературе не рассматривалась. Решаемая задача является мультифизической, включающей расчет: статического магнитного поля; электрической цепи с учетом изменения напряжения на конденсаторе и наведенной в катушках противо-ЭДС; динамики движения якорей бистабильного фиксатора и привода с учетом изменения массы; нестационарного электромагнитного поля в неоднородной нелинейной среде с учетом постоянных магнитов и движения проводящих тел в электромагнитном поле. Направления дальнейших исследований представляются в виде оптимизации геометрии, параметров катушек привода и конденсаторов, геометрии бистабильного механизма, объема и остаточной индукции постоянных магнитов для обеспечения требуемых значений быстродействия, контактного нажатия и габаритов аппарата. Библ. 11, табл. 1, рис. 13.
Ключевые слова: **индукционно-динамический привод, бистабильный фиксатор, постоянные магниты.**

Introduction. Recently, in the literature quite often induction-dynamic mechanisms (IDMs) are investigated and developed, known in foreign literature as a *Thomson-drive*, used as a drive for various electrical devices [1-4]. The simplicity and reliability of the design, high speed

make such devices indispensable in electrical devices installed in DC networks, in which emergency overcurrents are not limited by reactance and can reach tens of kiloamperes.

Despite the obvious advantages, such devices have a number of significant disadvantages: significant shock load on the structural elements; the need to fix the position of the mechanism at the start and end points of the movement trajectory with the possibility of returning to the starting position. The solution to the first problem is either to use damping devices at the final stage of movement, or using optimal control of the movement by connecting a braking coil. The second problem is solved through the use of bistable mechanical latches, known for a long time [3-5]. A mathematical model of the drive with optimal control of the IDM armature speed and mechanical bistable latch was considered in [4] and investigated in [6], where the main disadvantages of such a model are shown. In [7], a Thompson-drive was considered, and an electromagnetic latch is used as a position latch. But, according to the authors, the most promising drive designs for high-speed circuit breakers are drives that combine the speed of induction-dynamic systems and the reliability of magnetic systems with permanent magnets [8, 9]. For example, in [8] the calculation of such a drive consists of two parts: static calculation of the flux and electromagnetic force; dynamics calculation based on the ordinary differential equations of the motion and the electrical circuit. This approach is not new [10] and has a number of significant drawbacks associated with the determination of the braking effect of eddy currents in the system, especially in high-speed systems. In addition, the system is quite complex: two IDM coils are located inside two magnetic cores; the actuator also has two coils and consists of two magnetic cores with permanent magnets.

The IDM design flaws identified during the review significantly affect the reliability of the switching device. One way to solve the problem is the possibility of creating a drive mechanism with a bistable position latch based on permanent magnets.

The goal of the paper is analysis of the fundamental possibility of creating a switching device with an induction-dynamic drive on the basis of a mathematical model which allows to increase the reliability of the entire mechanism operation and significantly simplify the design.

Subject of investigations. This paper carries out a comprehensive study of the Thompson-drive with optimal control of the closing speed of electrical contacts, which uses a magnetic device consisting of a magnetic system, an armature with a non-magnetic rod and permanent magnets as the bistable latch of the movable system of the apparatus in the initial and final positions.

The mathematical model of the mechanism under study is solved by deformation of the computational mesh. The deformation of the mesh depends on the travel and speed of the armatures, which, in turn, determine the parameters of the system (electromagnetic forces, air gaps, etc.). This problem is multiphysical, i.e. the task of sequentially-parallel solution of several different in nature problems: calculation of static magnetic field; calculation of the electric circuit, taking into account the change in voltage on the capacitor and taking into account the counter-EMF induced in the coils; calculation of the dynamics of movement of the armatures of a bistable latch and drive taking into account the change in mass; calculation of transient electromagnetic field in an inhomogeneous nonlinear medium taking into account permanent magnets and the motion of conductive bodies in the electromagnetic field. The algorithm for solving the defined problem lies in the fact that at the initial stage, the stationary field of permanent magnets is calculated and the results obtained are used as initial conditions for the remaining parallel problems.

This paper can be classified as debatable, since it explores the very possibility of creating a new type of drive.

Basic calculation relationships and assumptions. Figure 1 shows a diagram of an apparatus with a drive system (in a cylindrical coordinate system) and overall dimensions in mm are indicated. The coils of the induction-dynamic drive 1, 2 perform the function of switching on and off the device on and off, as well as the function of optimally controlling the movement of the drive armature and bistable latch (reducing the speed of the contacts before closing).

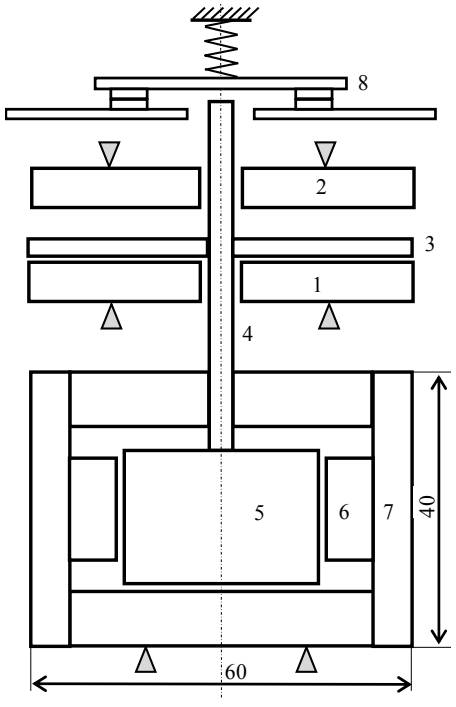

Fig. 1. Diagram of a switching device with an induction-dynamic drive and a bistable magnetic latch: 1, 2 – drive coils; 3– drive armature (conductive disk); 4 – non-magnetic rod; 5 – armature of the latch connected by a non-magnetic rod to the drive armature; 5 – permanent magnets located around the perimeter of the armature of the latch; 7 – fixed magnetic system; 8 – contact system of the switching device

The armature of the induction-dynamic drive 3, made in the shape of a disk, is connected to the armature

of the bistable latch 5 by a non-magnetic rod 4. The armatures 3 and 5 are fixed in the extreme positions (lower and upper) due to the action of permanent magnets 6 fixed in the housing. Such a drive mechanism consumes energy only during operation. To reduce the speed of contact closure when switched on, a reverse polarity (relative to coil 1) voltage is applied to the coil of winding 2, which slows down the speed of the system before touching the rod with contacts 8.

In the calculation, the following assumptions were made: a uniform distribution of the current density over the area of the coil winding space (the coil is wound with a wire whose cross-sectional area is much smaller than the coil winding space); the absence of hysteresis in ferromagnetic.

The main calculation relation is the equation of transient electromagnetic field written in the term of the magnetic vector potential [11] under the condition that there is no field at the outer boundary of the calculation domain

$$\sigma_k \cdot \frac{\mathrm{d}\boldsymbol{A}_k}{\mathrm{d}t} + \cdot\nabla\times\left(\frac{1}{\mu_k}\cdot\left(\nabla\times\boldsymbol{A}_k - \boldsymbol{B}_\mathrm{r}\right)\right) = \boldsymbol{\delta}_k\,, \qquad (1)$$

where σ_k is the electrical conductance of the material; $\boldsymbol{A}_k$ is the magnetic vector potential; μ_k is the absolute magnetic permeability; $\boldsymbol{B}_\mathrm{r}$ is the residual magnetic flux density of the permanent magnet; $\boldsymbol{\delta}_k = (i\cdot N/S)\cdot\mathbf{1}_\varphi$ is the current density of the external source; $\mathbf{1}_\varphi$ is the azimuthal unit vector – a unit vector directed perpendicular to the plane in which the calculation area is located; i is the current in the coil winding; N is the number of turns of the winding; S is the area of the winding space of the coil.

The form of the system of equations (1) is determined by the computational domain (air, coils, conductive disk, magnetic circuit, permanent magnet). In (1), the total time derivative is indicated in the case of calculation of the field in the moving domain (drive armature and bistable latch).

Electrical circuit equations

$$\begin{aligned} &L_1\cdot\frac{\mathrm{d}i_1}{\mathrm{d}t} + R_1\cdot i_1 + E_1 = \left(E_{C01} - \frac{1}{C_1}\cdot\int_t i_1\cdot\mathrm{d}t\right)\cdot\eta_1; \\ &L_2\cdot\frac{\mathrm{d}i_2}{\mathrm{d}t} + \left(R_2 + R_\mathrm{d}\cdot\eta_2\right)\cdot i_2 + E_2 = \\ &= \left(-E_{C02} - \frac{1}{C_2}\cdot\int_t i_2\cdot\mathrm{d}t\right)\cdot\eta_1, \end{aligned} \qquad (2)$$

where L_1, L_2 are the external circuit leakage inductances; R_1, R_2 are the resistances of windings of drive coils; $E_{1,2}$ are the counter-EMF of windings:

$$E_{1,2} = \frac{N}{S}\cdot\int_V\frac{\partial A_\varphi}{\partial t}\cdot\mathrm{d}V\,, \qquad (3)$$

where V is the volume of the coil winding (1 or 2); E_{C0} is the initial voltage on the capacitance; i_1, i_2 are the currents in the windings of the coils; R_d is the additional resistance; η_1, η_2 are the unit functions simulating the aperiodic discharge of the capacitor and the beginning of the discharge of the second capacitance to the winding of the braking coil.

$$\eta_1 = \begin{cases}1, U_c > 0\\ 0, U_c < 0\end{cases},\quad \eta_2 = \begin{cases}1, z(t) > z_1\\ 0, z(t) \le z_1\end{cases}. \qquad (4)$$

The equations of motion are equations of the dynamics of a body with a variable mass, because after the contacts are closed, the mass reduced to the IDM armature changes

$$\begin{cases}\dfrac{\mathrm{d}}{\mathrm{d}t}\cdot\left(m(z(t))\cdot v(t)\right) = \left[F_\mathrm{em} - F_0\cdot\eta_4 + F\left(z(t)\right)\right]\cdot\eta_3;\\ \dfrac{\mathrm{d}z(t)}{\mathrm{d}t} = v(t)\end{cases}, \qquad (5)$$

where $m(z(t))$ is the changing mass of the system; $v(t)$ is the speed of the movable system; $F_\mathrm{em} - F_0\cdot\eta_4 + F\left(y(t)\right)$ is the total force; η_3 is the function that prohibits movement beyond permissible limits (stops); η_4 is the function that determines the beginning of the collision of contacts and the beginning of the action of the force of contact pressing; $F\left(z(t)\right)$ is the force acting on the bistable latch's armature reduced to the drive armature.

The system of equations (1)-(5) is a mathematical model of a high-speed induction-dynamic drive with a bistable latch with permanent magnets.

Initial conditions and input data. As the input data, the masses moving along with the drive armature and the mass of contacts were specified. The moment of impact is extended by 0.3 ms in time, and the derivative of the mass along the coordinate was selected based on the law of conservation of moment of momentum.

Based on the geometry of the coils (Fig. 1) and the cross section of the winding wire, the resistances of the windings and the number of turns were determined taking into account the fill factor. Since each of the coils can be either accelerating or braking, the initial voltage and capacitance of the capacitors were chosen the same: 600 V, 400 μF.

Graphs of changes in mass and its derivative are shown in Fig. 2.

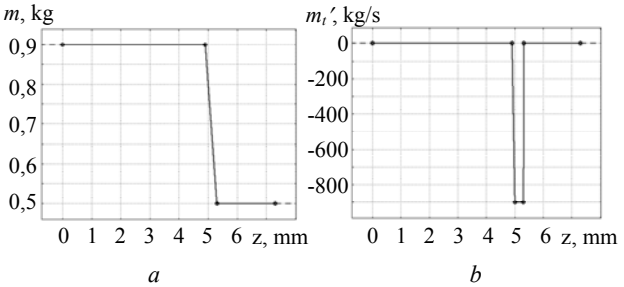

Fig. 2. Graphs of change in mass (*a*) and its derivative (*b*)

The software allows optimization calculations with a change in the cross section of the winding wire. One of the main parameters to be set is the full stroke of the system's armatures equal to 7 mm [6] and the stroke to the contact touch of 5 mm. The force of contact pressing

was assumed to be constant and equal to 200 N, the initial mass is 0.9 kg (see Fig. 2).

Results. Static calculations. These calculations are necessary for the following reasons: 1) the results obtained are the initial values for calculating the dynamics; 2) they make it possible to obtain a static power characteristic of a bistable latch as a function of the magnetic flux density of a permanent magnet. Figure 3 shows a picture of the magnetic field in the extreme positions of the bistable latch's armature.

Obviously, the redistribution of the magnetic field (Fig. 3) leads to a change in the sign of the electromagnetic force (Fig. 4). Changing the sign of the electromagnetic force of the latch provides bistable operation of the drive.

The static traction characteristic of the bistable latch as a function of the armature stroke is given for the value of the permanent magnet residual magnetic flux density B_r = 0.5 T. The values of the initial force depending on the value of the residual magnetic flux density of the permanent magnet are given in Table 1. Moreover, when the value of the residual magnetic flux density changes, the form of the characteristic does not change, but only the force values change.

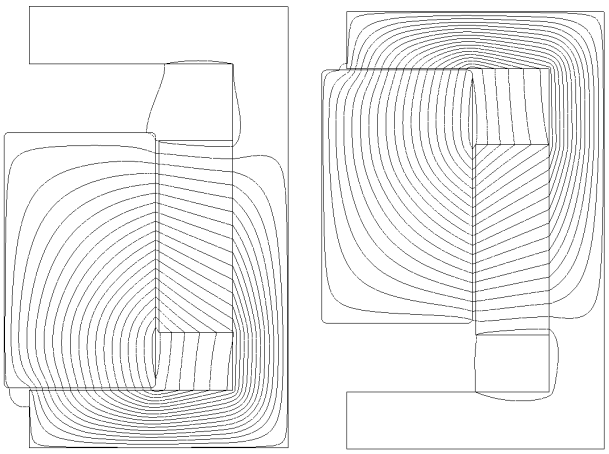

Fig. 3. Picture of the magnetic field of the bistable latch in the extreme positions of the armature (in static)

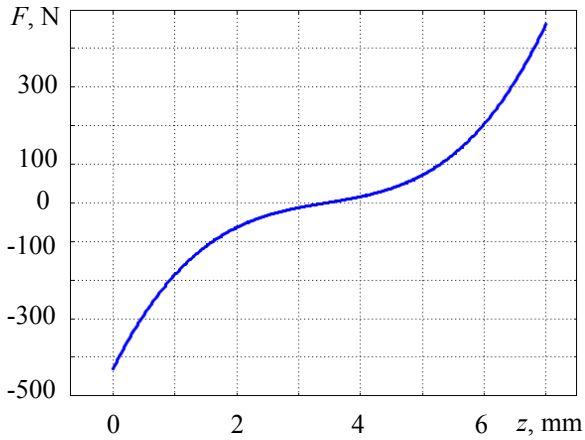

Fig. 4. Static traction characteristic of the bistable latch as a function of the armature stroke

Table 1

Values of initial force as a function of B_r

B_r, T	0.5	0.6	0.7	0.8	0.9	1.0
$F(0)$, N	429	571	689	776	844	899

The calculation of the dynamics. Switching on. Calculations show that the fields of the drive coils are closed through the magnetic circuit of the bistable latch which significantly affects the processes in it. Figure 5 shows the dependencies of the stroke of the bistable clatch's armature as a function of time for various types of magnetic circuit – solid and burnt ones. In the case of a solid magnetic circuit of a bistable clatch due to the demagnetizing effect of eddy currents that coincide in direction with the currents of the braking coil, there is a significant decrease in speed and the reverse movement of the armatures of the drive and bistable latch and no operation (curve 1). An increase in the resistance to eddy currents, for example, due to the use of steel with high specific resistance, lamination of the magnetic circuit or making radial cuts in it, ensures a clear operation of the switching device (curve 2).

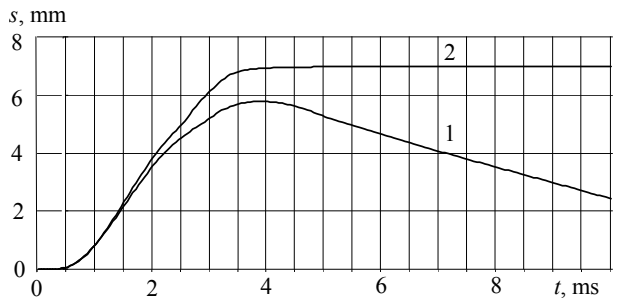

Fig. 5. Armature stroke for various types of magnetic circuit: 1 – solid; 2 – laminated

Figure 6 shows the field lines at the instant of maximum current in the «braking» coil of the induction-dynamic drive. As can be seen from Fig. 6, with the solid magnetic circuit, the field of the permanent magnet practically does not penetrate into the upper part of the latch's magnetic circuit (there is no redistribution of the flux and a change in the sign of force), in contrast to the laminated magnetic circuit, where the redistribution of the flux of the permanent magnet is clearly visible. This is confirmed by the calculated values of forces. At time of ≈1 ms (the field picture is shown in Fig. 6), the force acting on the bistable latch's armature in the case of the solid magnetic circuit is minus 130 N, for the laminated one is is plus 10 N (the force changed its sign).

The diameter of the winding wire (for fixed coil sizes) affects the nature of the movement and in the case of the solid magnetic circuit, the reverse movement of the bistable latch's armature may not be present. However, due to the action of eddy currents, the magnetic force of the bistable latch with the solid magnetic circuit in the final position of the armature is much less (about two times) than that of the bistable latch with the laminated magnetic circuit.

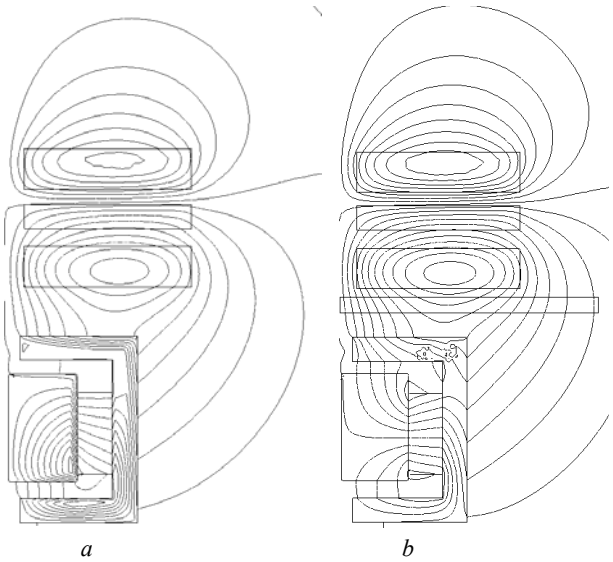

a *b*

Fig. 6. Picture of the field at the moment of maximum current in the «braking» coil: *a* – the solid magnetic circuit; *b* – the laminated magnetic circuit

The influence of the cross section of the winding wire of the coils on the contact closure speed is shown in Fig. 7. The speed graph consists of several sections: acceleration; braking before touching the contacts (the moment of touching is marked with a bold dot on the graphs); an increase in speed at a dip due to a decrease in the total moving mass (by the value of the mass of contacts); stop. In the examples considered, the time before touching the contacts differs by approximately 30 % (from 2.3 to 3 ms).

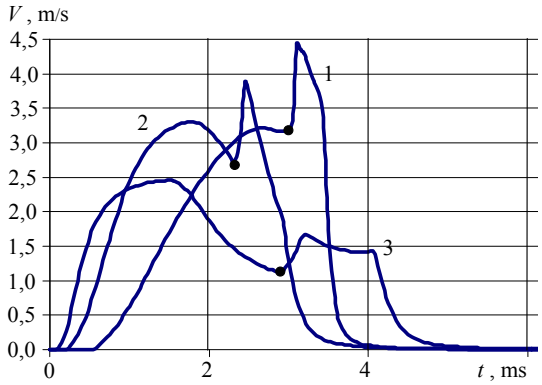

Fig. 7. Dependence of the contact closure speed on wire section: 1 – 0.66 mm^2 (N = 550); 2 – 1 mm^2 (N = 240); 3 – 1.5 mm^2 (N = 106)

As a result of the calculations, it was found that the stroke at which the discharge of the capacitor to the braking coil begins with the path taken and the contact failure affects the response time of the drive (Fig. 8).

Characteristic 1 corresponds to the beginning of the discharge of the capacitor to the braking coil when the armature stroke of the induction-dynamic drive is 0.5 mm (earlier braking). Characteristic 2 is later braking of the armature (2.5 mm stroke).

It can be seen from the graph (Fig. 8) that the operations time differs by about 25 %, which indicates a small effect of the braking coil on the movement of the drive armature (effect is significant with small gaps between the drive armature and the coil).

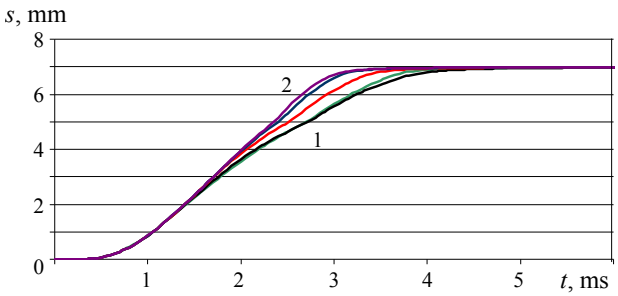

Fig. 8. Changing the value of the armature stroke in the function of the beginning of the signal supply to the braking coil (the beginning of the capacitor discharge): 1 – when the armature reaches the stroke value of 0.5 mm; 2 – when the armature reaches the stroke value of 2.5 mm; other values are intermediate

Further, all calculations of physical processes are carried out for the following values: the beginning of the braking process of the drive armature corresponds to the stroke of 0.5 mm with the coil wire cross section of 1.5 mm^2 (N = 106).

Figure 9 is a graph of the acting forces. As follows from Fig. 9, the force acting on the drive armature and the magnetic force of the bistable latch change their sign depending on the stroke. Characteristic 1 changes its sign due to the discharge of the capacitor to the braking coil, characteristic 2 – due to the redistribution of fluxes in the magnet.

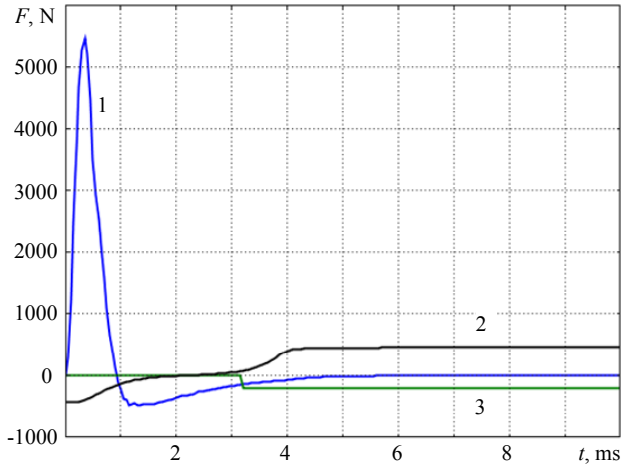

Fig. 9. Graphs of acting forces: 1 – force acting on the drive armature; 2 – magnetic force of the bistable latch; 3 – contact pressure force

Figure 10 shows the current values in the coils of the high-speed drive. As calculations show, coil currents have virtually no effect on each other. The aperiodic shape of the discharge (as the most optimal for using the energy of a capacitive storage and the safest for an electrolytic capacitor) is provided by diodes connected in parallel with the coils. Despite the identical

parameters of the coils and capacitive storage, the currents are different in maximum values and the decay rate (Fig. 10), which is associated with the position of the drive armature in the intercoil space (the equivalent inductance of the electrical circuits of the first and second coils is different).

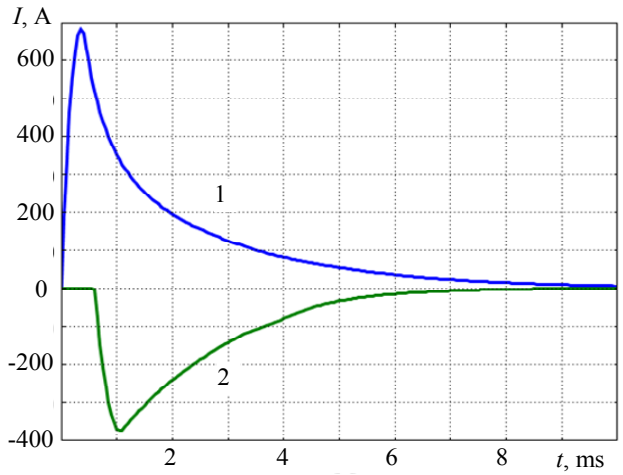

Fig. 10. Currents of the coils: 1 – switching on; 2 – braking

Figure 11 shows the dependencies of the stroke and speed of the drive armature and the bistable latch armature as a function of time during contact closure.

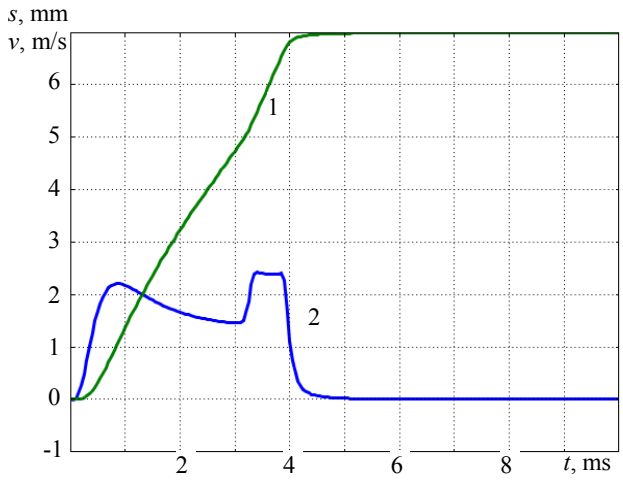

Fig. 11. Drive dynamics during contact closure: 1 – stroke; 2 – speed

The dynamics of the switching off. For high-speed switching devices, an important parameter is the time interval from the moment the signal is sent to the switching off to the moment the beginning of the contacts opening. Since the drive coils are identical, the changes in the model will relate to equations describing the mechanics of movement: – the force of contact pressure on the value of the contact failure will be not opposing, but driving; – the mass change graph will be mirrored with respect to the graph in Fig. 2,*a*, and the derivative of the mass with respect to the displacement (Fig. 2,*b*) will be positive.

Figure 12 shows the drive's switching off dynamics. As follows from Fig. 12, the opening of the contacts occurs in a time of the order of 1 ms, which confirms its speed.

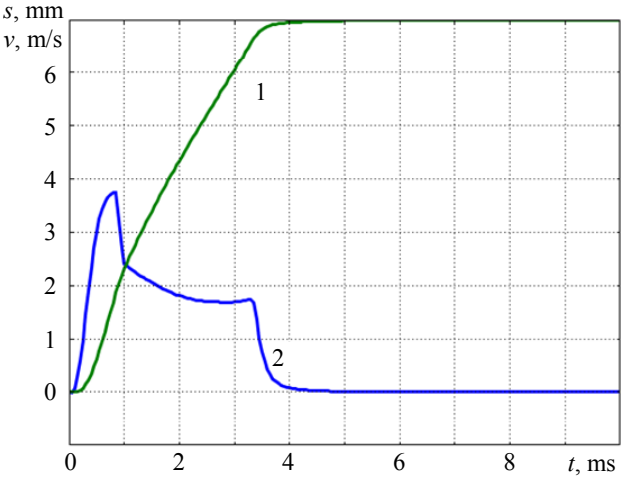

Fig. 12. Switching off dynamics: 1 – stroke; 2 – speed

Figure 13 shows the current in the armature of the induction-dynamic drive during the «switching off» operation.

Despite the current value of 45 kA, the temperature of the armature of the induction-dynamic drive during the movement increases slightly (by 0.8 °C) due to the short duration of its thermal effect.

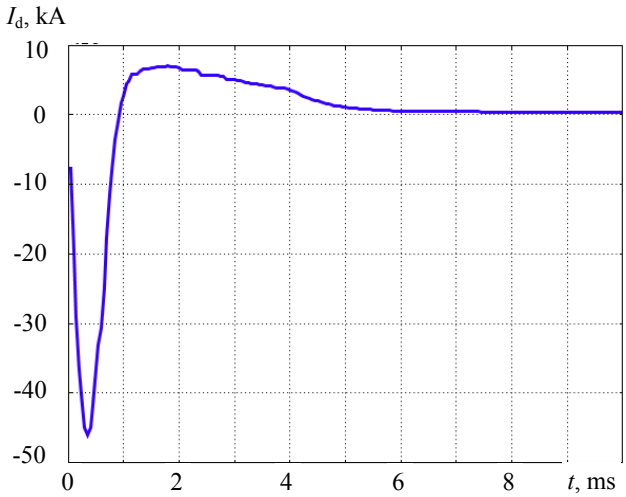

Fig. 13. Drive armature current as a function of time

Conclusions.

1. A mathematical model of a new high-speed induction-dynamic drive with a bistable latch based on permanent magnets based on the equations of the electromagnetic field, the electric circuit and the equations of motion has been developed and partially investigated. The model allows to calculate the dynamic parameters of the drive based on the source data.

2. The fundamental possibility of creating a high-speed drive of this type is shown.

3. Directions for further research may be the following: optimization of the geometry, parameters of the drive coils and capacitors, the geometry of the bistable latch, the volume and residual magnetic flux density of

permanent magnets to ensure the required values of speed, contact pressure and dimensions of the apparatus. A further area of research may also be the study of processes at the contacts of the circuit breaker depending on the parameters of the drive and the calculation of the mechanical forces arising in the drive during starting, movement and braking.

REFERENCES

1. Bolyukh V.F., Schukin I.S. Investigation of thermal processes in a linear pulse-induction electromechanical converter of cyclic action. *Electrical engineering & electromechanics*, 2017, no.5, pp. 14-22. **doi: 10.20998/2074-272X.2017.5.02.**

2. Baida E.I. Mathematical modeling of induction-dynamic systems. *Electrical engineering & electromechanics*, 2009, no.5, pp. 13-16. (Rus).

3. Bissal A. *On the design of ultra-fast electromechanical Actuators. Licentiate thesis, monograph*. Electromagnetic Engineering School of Electrical Engineering, Stockholm, Sweden, 2013. 68 p.

4. Wen W., Huang Y., Al-Dweikat M., Zhang Z., Cheng T., Gao S., Liu W. Research on operating mechanism for ultra-fast 40.5-kV vacuum switches. *IEEE Transactions on Power Delivery*, 2015, vol.30, no.6, pp. 2553-2560. **doi: 10.1109/tpwrd.2015.2409122.**

5. Aleksandrov G.N., Borisov V.V., Ivanov V.A. *Teoriia elektricheskikh apparatov* [Theory of electrical apparatus]. Moscow, Vysshaia shkola Publ., 1985. 312 p. (Rus).

6. Baida E.I., Volkova O.G. Mathematical model of a quick-driving actuator of an automatic switch with an instant-dynamic and bistable mechanism. *Electrical Engineering and Power Engineering*, 2018, no.1, pp. 30-39. **doi: 10.15588/1607-6761-2018-1-4.**

7. Meyer J.-M., Rufer A. A DC hybrid circuit breaker with ultra fast contact opening and integrated gate-commutated thyristors (IGCT). *IEEE Transactions on Power Delivery*, 2006, vol.21, no.2, pp. 646-651. **doi: 10.1109/tpwrd.2006.870981**.

8. Wang Z., Sun L., He S., Geng Y., Liu Z. A permanent magnetic actuator for 126 kV vacuum circuit breakers. *IEEE Transactions on Magnetics*, 2014, vol.50, no.3, pp. 129-135. **doi: 10.1109/tmag.2013.2284251**.

9. Young-woo Jeong, Seok-won Lee, Young-geun Kim, and Hyun-wook Lee. High-speed AC circuit breaker and high-speed OCR. *22nd International Conference and Exhibition on Electricity Distribution (CIRED 2013)*. Stockholm, 2013. pp. 1215-1218. **doi: 10.1049/cp.2013.0834**.

10. Klymenko B.V. *Forsirovannye elektromagnitnye sistemy*. [Forced electromagnetic systems]. Moscow, Energoatomizdat Publ., 1989. 160 p. (Rus).

11. Baida E.I. A mathematical model of calculation the dynamics of two-position electromagnetic actuators of medium voltage vacuum circuit breakers. *Journal of scientific publications of graduate students and doctoral students*, 2013, no.1, pp. 136-141. (Rus).

Received 15.04.2019

E.I. Baida[1]*, Doctor of Technical Science, Associate Professor,*
V.V. Lytvynenko[1]*, Senior Instructor,*
A.A. Chepeliuk[1]*, Candidate of Technical Science, Associate Professor,*
[1] National Technical University «Kharkiv Polytechnic Institute», 2, Kyrpychova Str., Kharkiv, 61002, Ukraine,
e-mail: baida.kpi@gmail.com, vikalitv21082@gmail.com, chep1@i.ua

How to cite this article:
Baida E.I., Lytvynenko V.V., Chepeliuk A.A. Peculiarities of dynamics of a fast-driven induction-dynamic drive with a bistable latch of contacts position of a circuit breaker based on permanent magnets. *Electrical engineering & electromechanics*, 2020, no.1, pp. 3-9. **doi: 10.20998/2074-272X.2020.1.01.**

UDC 621.313.322 **doi: 10.20998/2074-272X.2020.1.02**

Yu.M. Vaskovskyi, O.A. Geraskin

TURBOGENERATOR ROTOR HEATING IN PRESENCE OF ROTOR WINDING DEFECTS AND EXCITATION CURRENT FORCING

Purpose. ***Research of the TGV-200 turbogenerator rotor heating in case of rotor winding damages, which occur as a result of prolonged operation of the turbogenerator, namely - clogging of the ventilation channels of the rotor winding and the occurrence of short circuits of the rotor windings. Particular attention is paid to heating during short-term increasing of the excitation current, which is performed to keep the generator in synchronous mode of operation.*** ***Methods.*** ***Field mathematical models are used.*** ***Results.*** ***It is determined that the clogging of the rotor winding ducts has a greater effect on the rotor heating compared to the short circuits of the individual windings of the rotor winding. It was defined that increasing of the excitation current within the limits regulated by the current standards of the turbogenerators operation becomes impossible with clogging of a small number of ventilation channels of the rotor winding, which impairs the efficiency of the turbogenerator and requires its output to repair.*** ***Scientific novelty.*** ***A mathematical model of rotor heating is developed in case of typical damages of the rotor winding.*** ***Practical value.*** ***The areas in the rotor where the temperatures and temperature gradients reach the highest values was determined, which allows to recommend the locations of the optimal temperature sensors placements.*** References 10, figures 11.

Key words: **turbogenerator, rotor winding, temperature, temperature gradient, short circuit, clogging of cooling channels, excitation forcing.**

Мета. ***Дослідження нагріву ротора турбогенератора типу ТГВ-200 за наявності ушкоджень обмотки ротора, які виникають внаслідок тривалої експлуатації турбогенератора, а саме – засмічення (закупорка) вентиляційних каналів обмотки ротора і виникнення коротких замикань витків обмотки ротора. Особлива увага приділяється нагріву при короткочасному форсуванні струму збудження, яке виконується для утримання генератора в синхронному режимі роботи.*** ***Методика.*** ***Використовуються польові математичні моделі.*** ***Результати.*** ***Визначено, що засмічення вентиляційних каналів обмотки ротора в більшій мірі впливає на нагрів ротора у порівнянні з коротким замиканням окремих витків обмотки ротора. Встановлено, що форсування струму збудження в межах, які регламентовані діючими стандартами експлуатації турбогенераторів, стає неможливим при засміченні невеликої кількості вентиляційних каналів обмотки ротора, що погіршує ефективність роботи турбогенератора і потребує його виводу в ремонт.*** ***Наукова новизна.*** ***Розроблено математичну модель нагріву ротора при наявності типових ушкоджень обмотки ротора.*** ***Практичне значення.*** ***Визначено ділянки в роторі, де температури і температурні градієнти досягають найбільших значень, що дозволяє рекомендувати місця оптимального розташування датчиків температури.*** Бібл. 10, рис. 11.

Ключові слова: **турбогенератор, обмотка ротора, температура, градієнт температури, коротке замикання, засмічення охолоджуючих каналів, форсування збудження.**

Цель. ***Исследование нагрева ротора турбогенератора типа ТГВ-200 при наличии повреждений обмотки ротора, которые возникают в результате длительной эксплуатации турбогенератора, а именно – засорение (закупорка) вентиляционных каналов обмотки ротора и возникновения коротких замыканий витков обмотки ротора. Основное внимание уделяется нагреву при кратковременном форсировании тока возбуждения, которое выполняется для удержания генератора в синхронном режиме работы.*** ***Методика.*** ***Используются полевые математические модели.*** ***Результаты.*** ***Установлено, что засорение вентиляционных каналов обмотки ротора в большей степени влияет на нагрев ротора по сравнению с коротким замыканием отдельных витков обмотки ротора. Установлено, что форсирование тока возбуждения в пределах, которые регламентированы действующими стандартами эксплуатации турбогенераторов, становится невозможным при засорении небольшого количества вентиляционных каналов обмотки ротора, что ухудшает эффективность работы турбогенератора и требует его вывода в ремонт.*** ***Научная новизна.*** ***Разработана математическая модель нагрева ротора при наличии типовых повреждений обмотки ротора.*** ***Практическое значение.*** ***Определены участки в роторе, где температуры и температурные градиенты достигают наибольших значений, что позволяет рекомендовать места оптимального расположения датчиков температуры.*** Библ. 10, рис. 11.

Ключевые слова: **турбогенератор, обмотка ротора, температура, градиент температуры, короткое замыкание, засорение охлаждающих каналов, форсирование возбуждения.**

Introduction. The reliability of the turbogenerator (TG) largely determines the reliability of the power plant as a whole. Unforeseen damage of TG leads to significant economic losses, and therefore ensuring the reliable operation of power units of the power plant and, in particular, TG remains an urgent scientific and technical task. Its relevance is especially increasing recently due to the aging of the existing TG park.

The reliability of the TG depends largely on the heating of the structural parts of its design, and in particular the design of the rotor. During the operation of a proper TG, significant overheating of the rotor can occur for various reasons: prolonged operation of the TG in asynchronous or asymmetric modes, long-term forcing of the excitation current, etc. Such overheating is predictable and is taken into account in the calculations when designing TG. However, in the process of long-term operation of the TG, the gradual degradation of the structure causes damage that causes unacceptable overheating. Thus, significant unacceptable overheating of the rotor winding (RW) occurs in case of disturbances in the cooling system, damage of the electrical insulation of the winding and turn's short circuits, etc. Short circuits

of the winding turns of the TG may occur as a result of overheating or gradual mechanical grinding of the insulation of the turns when the temperature extensions vary over time. Significant overheating of the RW occurs as a result of overlapping of the ventilation ducts of the RW turns due to their clogging (dirt appearance) or due to the displacement of insulating gaskets between the turns at the TG starts and stops. Particularly critical is overheating when the excitation current is forced to flow in the damaged RW.

In order to avoid significant economic losses due to the damage to the RW to replace the planned and preventive repairs, repairs are made according to the results of the assessment of the actual technical condition, based on the utilization of systems of control and monitoring of the technical condition of the TG rotor elements, including the temperature sensors. Modern methods of non-destructive testing of the thermal state of the TG rotor involve the use of control equipment for heating of electrical equipment with the use of various measurement methods based on the fixation of readings of: thermometer, ohmmeter, thermocouple and the level of infrared radiation. Real-time monitoring and analysis of heating of the TG rotor elements is performed with the help of temperature sensors embedded in different TG points during its production.

To improve the efficiency of intellectual control of the thermal condition of the rotor, the results of mathematical modelling of its heating in different modes of operation of TG and different variants of damage to the RW are required. The study of the temperature field in TG was carried out in [1-10]. In particular, [1] investigated the effect of clogging of the cooling channels of the RW on the temperature field and local overheating of the TG rotor, which depend on the number of clogged channels of the RW. These studies were conducted at the nominal value of the excitation current. But, as already noted, unacceptable heating of the RW occurs during the forcing of the excitation current, which in order to keep the TG in synchronism at the occurrence of short circuits in the network is temporarily performed by the excitation system. The combination of the effects of these two factors – the presence of RW clogged cooling channels and forcing the excitation current leads to unacceptable overheating of the RW even with a small number of clogged channels. The possible presence of short-circuited (SC) turns of the RW also influences on this. Studies in this formulation of the problem have not been conducted so far, but the relevance of such consideration is increasing in view of the reduction of the residual life of the powerful TGs currently being used at Ukrainian power plants.

The goal of the work is the investigation of the temperature state of the TG rotor in the appearance of typical damage of the RW: the presence of clogged cooling channels of the RW turns and a short circuit of the part of the RW turns, both in the rated mode of operation of the TG, and at forcing its excitation current.

Object of study. For the study of the temperature field the turbogenerator TGV-200 of power of 200 MW with hydrogen cooling was selected, having the following parameters: the outer diameter of the rotor barrel D_R = 1.075 m, the length of the rotor barrel L_R = 5.1 m, the number of slots/ tooth division of the rotor Z_2/Z_Z = 36/52, the rotor rotation speed n = 3000 rpm, the excitation voltage U_f = 440 V, the nominal value of power factor $\cos\varphi_n$ = 0.85 (over-excitation), the heat resistance class of rotor winding insulation – F (155 ºC).

The thermal conductivity of the materials of the TG rotor were taken as follows: a) the equivalent thermal conductivity of the slot insulation of the rotor winding (taking into account the presence of small gaps between the insulation and the slot walls) λ_{is} = 0.25 W/(m·°C); b) the thermal conductivity of the duralumin wedges of the rotor λ_0 = 155 W/(m·°C); c) the thermal conductivity of copper conductors of the RW λ_{Cu}=400 W/(m·°C) [4].

The coefficients of heat transfer from different design surfaces of the rotor to the cooling medium α have different numerical values for different surfaces, namely for the outer surface of the rotor barrel, the surfaces of the ventilation channels in the copper conductors of the RW. The following numerical values of the coefficients of heat transfer between these surfaces and hydrogen were adopted [1, 4]: a) the coefficient of heat transfer between the outer surface of the rotor barrel and cooling hydrogen α = 1100 W/(m^2·°C); b) the coefficient of heat transfer between copper conductors of turns and hydrogen in ventilation ducts of the RW α_v = 450 W/(m^2·°C).

The mathematical model of the TG rotor temperature field in steady-state modes is based on the stationary differential equation of thermal conductivity, which in Cartesian coordinates in 2D formulation has the following form [4]:

$$\lambda\left[\frac{\partial^2\theta(x,y)}{\partial x^2}+\frac{\partial^2\theta(x,y)}{\partial y^2}\right]=Q(x,y), \qquad (1)$$

where $\theta(x, y)$ is the unknown temperature distribution function; λ is the thermal conductivity; $Q(x, y)$ are the volumetric specific heat field sources, W/m^3 which are the power losses in the elements of the TG rotor when operating in the nominal synchronous mode and during the excitation. In particular, the following sources of heat dissipation were taken into account: a) Joule power losses in copper of the RW $Q_{RW}=i_{RW}^2\cdot r_{RW}$, where i_{RW} and r_{RW} are the current and active resistance of the RW, respectively; b) the ventilation losses on the rotor surface during its rotation, which were determined by known formulas in the TG design manuals.

On the outer surface of the rotor and on the inner surfaces of the ventilation channels of the rotor winding boundary conditions of the third kind were set:

$$\lambda\frac{\partial\theta}{\partial n}=-\alpha(\theta-\theta_M), \qquad (2)$$

where α is the above coefficient of heat transfer; θ_M is the temperature of the cooling refrigerant (hydrogen). The average hydrogen temperature was assumed to be θ_M = 45 °C with regard to its heating during the passage of long ventilation ducts of the RW turns.

The found stationary temperature distribution is used as the initial temperature distribution in solving the problem of transient thermal conductivity in the modes of

forcing the excitation current, which is described by the following equation [4]:

$$\lambda\left[\frac{\partial^2\theta(x,y,t)}{\partial x^2}+\frac{\partial^2\theta(x,y,t)}{\partial y^2}\right]-c\rho\frac{\partial\theta(x,y,t)}{\partial t}=-Q(x,y,t), \quad (3)$$

where $Q(x, y, t)$ are the volumetric specific power losses for the problem of transient thermal conductivity, W/m^3; c is the heat capacity, ρ is the specific density of the material, t is the time. Equation (3) is solved together with conditions (2).

Modelling of damage of the RW has been carried out as follows. With a short circuit of the turns of the RW, the specific losses in SC turns are zero due to the lack of excitation current in them. The presence of clogged ventilation ducts in the RW turns was modelled by the absence of heat transfer from the inner surface of the ventilation ducts: the heat transfer coefficient between the turns' conductors in the rotor slot and the clogged ventilation duct was assumed $\alpha_v = 0$.

Results of investigations. For the purpose of comparative analysis, the results of simulation and study of the temperature field in the rotor with different technical condition and operating mode of the TG are presented below.

1. Heating of the intact rotor in the nominal TG operation mode. The simulation results are obtained in Comsol Multiphysics 5.4 and reflect the TG rotor temperature field in nominal mode. The picture of the field is shown in Fig. 1.

According to the results of the analysis we can draw the following conclusions:

1. The maximum RW copper temperature is observed in the slots of the rotor, which are located around the q axis of the rotor. In particular, the maximum conductor temperature is 87.2 ºC and is observed in the 3rd OR turn from the bottom of the slot which is located near the q axis.

2. The highest heating in the TG rotor steel is observed in the middle teeth on the q axis and in the rotor yoke. Figure 2 shows the temperature distribution in the rotor steel along the diameter along the q and d axes.

3. The least heated are duralumin wedges and large rotor teeth (45.3 ºC), which is conditioned by their cooling conditions.

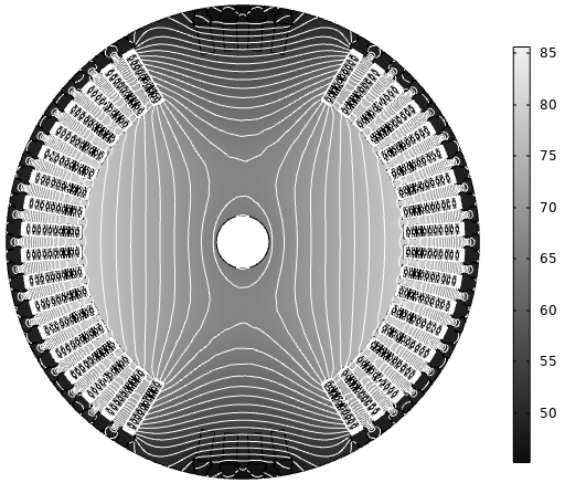

Fig. 1. Temperature distribution in the rotor of the intact TG

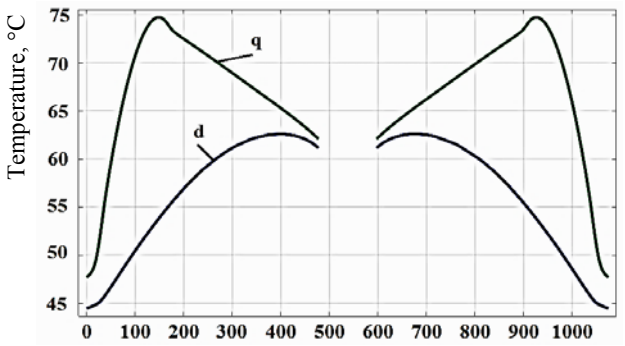

Fig. 2. Temperature distribution in the rotor steel of the intact TG along the radius along the d and q axes

The study of the temperature gradient distribution in the TG rotor makes it possible to determine the areas where the highest thermomechanical stresses occur. It is established that:

1. Temperature gradients on the steel sections near the bottom of the slots adjacent to the large teeth are greater (300 ºC/m) compared to the temperature gradients on the rotor steel sections located near the bottom of the slots around the q axis (126 ºC/m).

2. Relatively large values of temperature gradients in steel are observed at the top of the teeth near the rotor wedges (565 ºC/m).

3. The temperature gradients in the electrical insulation of the slots reach much higher values, in particular: in the fiberglass insulation under the wedges (11627 ºC/m),; in the fiberglass insulation in the base of slots (9913 ºC/m); in the fiberglass insulation adjacent to the walls of the large tooth (17006 ºC/m); in the fiberglass insulation adjacent to the walls of the remaining slots (18542 ºC/m).

This is due to the fact that the RW turns are the most heated elements, and the duralumin wedges and the rotor steel are the most cooled. Therefore, when choosing a material for insulating pads under the wedge and at the base of the slot, it is advisable to give preference to materials having a lower coefficient of thermal expansion to prevent significant thermomechanical stresses.

A separate question arises when choosing the thermophysical parameters of the RW insulation of the TG. The temperature fields in the rotor were investigated when replacing the existing regular insulation of the RW, which has the thermal conductivity λ_{is} = 0.25 W/(m·°C), with a more thermally conductive insulation of the Micadur type with the thermal conductivity λ_{is} = 0.58 W/(m·°C), which was proposed in [2].

According to the results of numerical calculations, it was found that the temperature gradient in the fiberglass insulation adjacent to the walls of the small tooth near the q axis decreased by 16.8 %, and in the sub-wedge laying of the slot located near the large TG tooth decreased by 36.2 %. But overall, the maximum temperature in the intact rotor decreased by only 1.5 °C (1.7 %) to 85.7 °C. This result is explained by the fact that 85 … 90 % of the heat dissipation in the RW is transferred through the ventilation ducts in the turns and only 10 … 15 % of the heat dissipation passes through the insulation and is transferred from the rotor surface.

2. Heating of the rotor with a short circuit of the RW turns. At a short circuit of a part of the turns of the RW, the excitation current bypasses the SC turns. Therefore, the electrical resistance of the RW decreases and the excitation current increases, which increases the heating of the other turns of the RW. Figure 3 shows the dependence of the RW temperature on the number of SC turns that are in the same coil in one slot of the rotor.

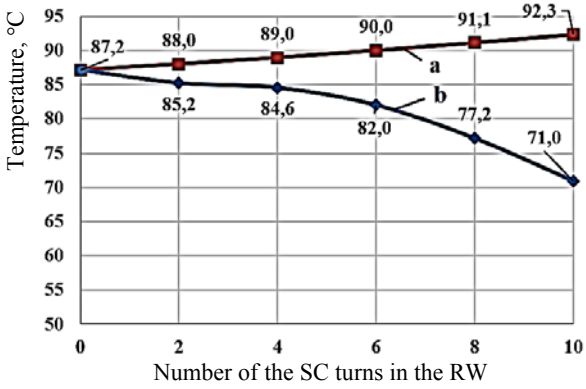

Fig. 3. Maximum temperature depending on the number of the SC turns in the slot of the RW: *a*) over the entire area of the rotor; *b*) in the damaged slot of the rotor on the *q* axis of the rotor

For example, with the short circuit of all 10 turns of the RW coil located in one slot, the maximum temperature of the other turns of the RW increases by only 6 % (Fig. 3,*a*). The temperature in the slot with SC turns is slightly reduced because the damaged turns are not loaded with current (Fig. 3,*b*). From Fig. 3 it can be concluded that, even with a short circuit of even 10 turns of the RW (5.56 % of the total number of turns of the RW), the rotor heating increases slightly.

The rotor heating leads to an increase in the temperature gradient in the RW insulation of the TG (Fig. 4).

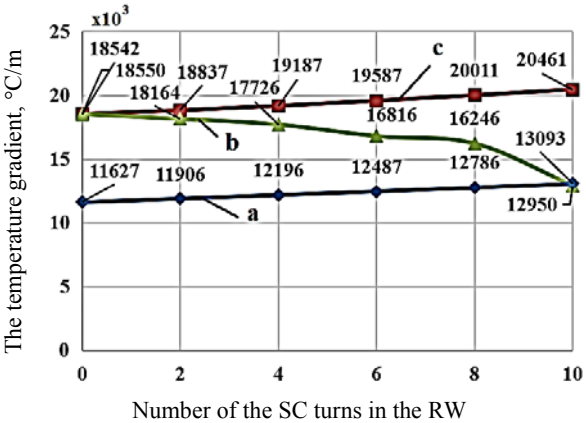

Fig. 4. Maximum value of the temperature gradient, depending on the number of the SC turns of the RW: *a*) in the sub-wedge laying of the slot; *b*) in the fiberglass insulation adjacent to the walls of the small tooth; *c*) throughout the rotor area

3. Rotor heating during clogging of the cooling channels of the RW turns. Figure 5 shows the maximum temperature in the RW in the presence of clogged cooling channels of the RW turns located in one slot.

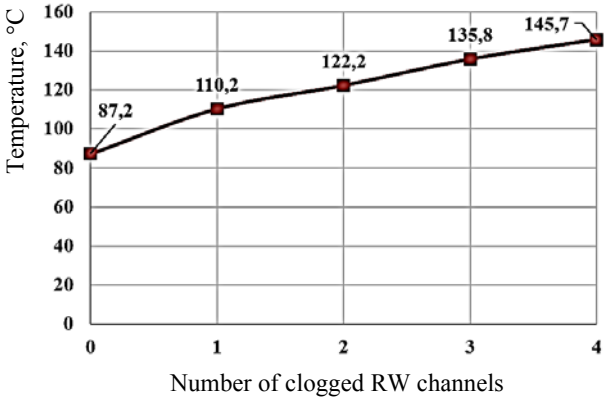

Fig. 5. Maximum temperature in the slot of the rotor depending on the number of clogged RW channels

Figure shows that when clogging in the slot of 4 of the 10 existing ventilation channels, the maximum temperature in this slot increases by 56 % and approaches the critical permissible insulation temperature of class F, and with more clogged channels it exceeds the permissible temperature. Figure 6 shows the increase of the temperature gradient in the insulation of the RW during clogging of the cooling channels. From Fig. 6 it can be seen that when the 4 channels are clogged, the temperature gradient in the insulation of the RW increases 2.2 times. Thus, unlike short circuits of turns, the clogging of their ventilation channels causes significantly dangerous overheating of the RW.

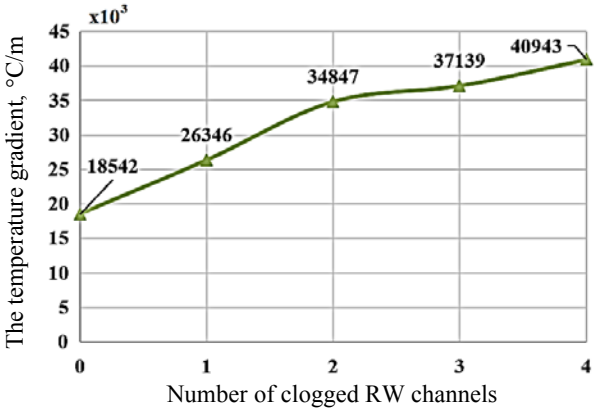

Fig. 6. Maximum value of the temperature gradient in the fiberglass insulation as a function of number of the clogged channels of the RW

4. Heating of the rotor when forcing the excitation current. In accordance with the requirements of item 4.17 of the Standard GOST 21558-2000, the direct-cooled TG excitation system must withstand a double rated excitation current for at least 20 s. The calculated heating of the rotor during the following process of forcing the excitation current was considered: for a time of 1 s, the excitation current according to a linear law increases from the nominal value to the forced value, which is determined by the coefficient of forcing

$$k_f = \frac{i_{ff}}{i_{fn}},$$

where i_{ff}, i_{fn} are, respectively, the forced and nominal value of the excitation current (in the calculations the

coefficient varies within 1.25 … 2). For a further 19 seconds, the forced current value remains unchanged. The temperatures acquired by the rotor at the end of the specified forcing process are presented below.

Dependencies of maximum values of the temperature and temperature gradient in the rotor on the value of the forcing factor k_f are shown, respectively, in Fig. 7, 8. For comparison, Fig. 7 also shows a line of the allowed temperature value.

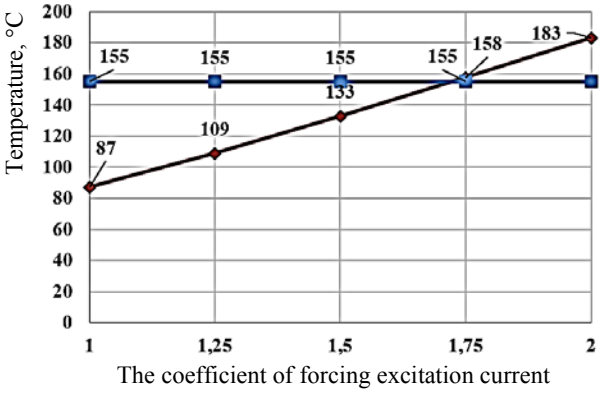

Fig. 7. Maximum temperature in the slot of the rotor of the intact TG, depending on the coefficient of forcing excitation current

From Fig. 7 it can be seen that already at k_f = 1.75 the maximum temperature in the rotor reaches the maximum permissible value. There are also significant temperature gradients in the insulation of the RW (Fig. 8), which are 3.1 times higher than their values in the nominal mode, which makes it possible to damage the insulation of the RW not only due to overheating, but also due to significant thermomechanical deformations.

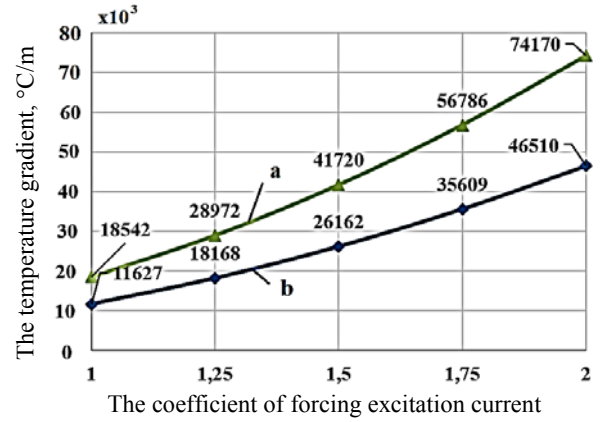

Fig. 8. Maximum values of the temperature gradient depending on the coefficient k_f:
a) in the fiberglass slot insulation;
b) under the wedge insulation

5. Heating of the rotor during clogging of the ventilation channels of the RW, forcing of the excitation current and short circuits of the RW turns. It is unacceptable to heat in the case of forcing the excitation current if the RW contains the damage discussed above. Figure 9 depicts the temperature dependence of the forcing coefficient of the excitation current of at the different number of the SC turns of the RW and in the absence of clogged ventilation channels. Figure 10 shows the dependence of the rotor temperature on the coefficient of forcing the excitation current at the different number of clogged ventilation channels (varies from 0 to 3) and in the absence of the SC turns of the RW. In Fig. 9, 10, the lower graph corresponds to the intact rotor, and as the number of damaged turns increases, the graphs pass higher. From Fig. 9 it is shown to what extent, depending on the number of the SC turns the admissible value of the coefficient k_f decreases.

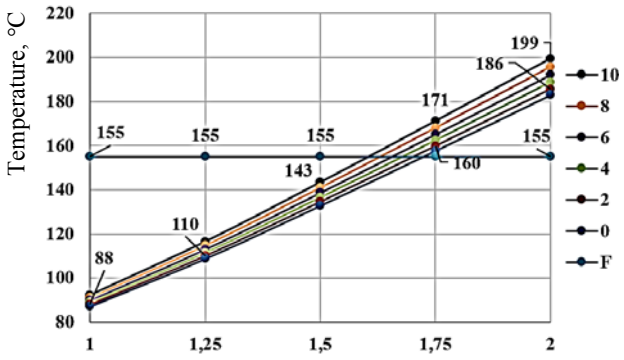

Fig. 9. Maximum temperature in the TG rotor, depending on the coefficient of forcing of the excitation current and the different number of the SC turns of the RW (in the absence of clogged channels)

From Fig. 10 it can be seen that when the 3 channels are clogged when the excitation current is forced twice, the maximum temperature rises to 337 °C, which is unacceptable. Thus, damage of the cooling system of the RW during the clogging of the ventilation channels significantly affects the possibility of forcing the excitation current, provided that the permissible heating of the RW is maintained. Regulated forcing becomes impossible, since even at the 1st clogged channel, the allowed k_f value is only 1.35, which does not meet the requirements of the existing TG operating standards.

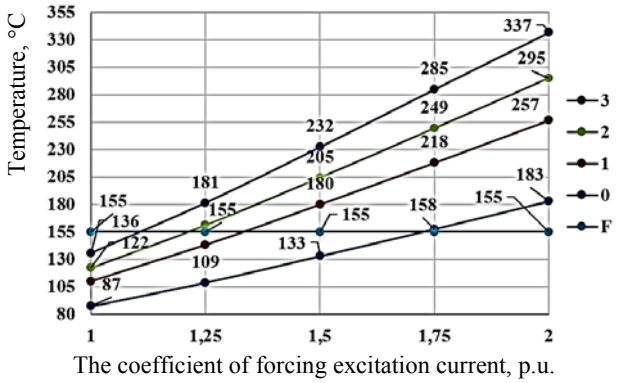

Fig. 10. Maximum temperature in the TG rotor, depending on the k_f coefficient with different number of clogged channels and the absence of the SC turns of the RW

Figure 11 depicts similar dependencies for one of the probable variants of combined damage: at one clogged channel and at two SC turns of the RW in forcing excitation. From Fig. 11 it can be seen that such combined damage is also dangerous for the TG.

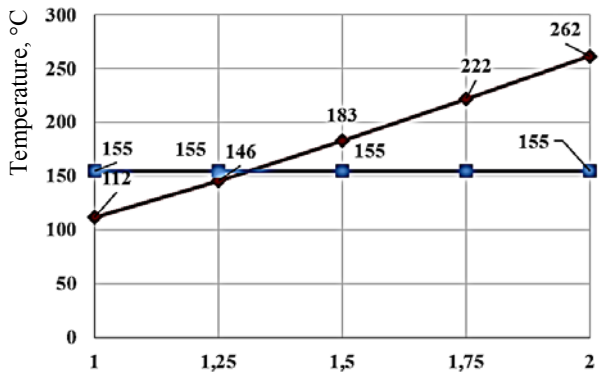

Fig. 11. Maximum temperature in the rotor at one clogged channel and at two SC turns of the RW depending on the coefficient of forcing of the excitation current

Conclusions.

1. In the long-term operation of powerful TG, in the RW damages occur – clogging (blocking) of the ventilation channels and short circuits of the RW turns, as a result of which the heating of the RW is substantially increased both in the steady rated mode of operation, and, especially, when the excitation current is forced in dynamic modes.

2. Ventilation ducts clogging is particularly dangerous. Even with one clogged channel, the continuous forcing of the excitation current can occur with coefficient of not more than 1.4 (or it is necessary to significantly reduce the forcing time), and for 3 or more clogged channels the forcing becomes practically impossible and the TG needs to be removed for repair. Therefore, it is important to develop reliable methods and tools for diagnosing and timely elimination of clogging of the ventilation channelsof the RW turns of the TG.

3. Areas with the highest values of the temperature and temperature gradient are determined, which allows to reasonably place temperature sensors.

REFERENCES

1. Kuchinskiy K.A. Analysis of the temperature field of the of 300 MW turbogenerator rotor with asymmetry in the cooling of the slot zone. *Technical electrodynamics*, 2013, vol.4, pp. 59-66. (Rus).

2. Fedorenko G.M., Kolesnik G.A. High-voltage insulation system with increased thermal conductivity for turbogenerators. *Works of institute of electrodynamics National Academy of Sciences of Ukraine*, 2010, no.25, pp. 38-41. (Rus).

3. Fedorenko H.M., Vaskovskyi Yu.M., Saratov V.O. Temperature distribution in the rotor in case of excitation current forcing in the Q-winding of the modernizing TGV-300 turbogenerator. *News of power engineering*, 1998, no.4, pp. 33-39. (Ukr).

4. Filippov I.V. *Teploobmen v electrisnyh masynah* [Heat transfer in electric machines]. Leningrad, Energoizdat Publ., 1986. 256 p. (Rus).

5. Shulzhenko N.G., Gontarovsky P.P., Protasova T.V. Influence of non-uniformity of heat dissipation in the generator rotor on its thermal stress state. *Aerospace Engineering and Technology*, 2007, no.8(44), pp. 135-139.(Rus).

6. Lu Y., Li W., Ma X., Jin H.Y. Numerical simulation of temperature field in rotor of large turbogenerator with air-coolant. *Proceedings of the Chinese Society of Electrical Engineering*, 2007, vol.27, no.12, pp. 7-13.

7. Weili L., Xuefeng Y., Debao G., Yongli F. Calculation and analysis of fluid flow and heat transfer of air cooled turbogenerator with multipath ventilation. *Transactions of China Electrotechnical Society*, 2009, vol.24, no.12, pp. 24-31.

8. Singh A.N., Doorsamy W., Cronje W. Thermographical analysis of turbogenerator rotor. *Electric Power Systems Research*, 2018, vol.163, pp. 252-260. **doi: 10.1016/j.epsr.2018.06.019.**

9. Irwanto B., Eckert L., Prothmann T. Thermal unbalance behaviour of turbogenerator rotors. *Proceedings of the 9th IFToMM International Conference on Rotor Dynamics*. Springer, Cham, 2015, pp. 2231-2242. **doi: 10.1007/978-3-319-06590-8_183**.

10. Weili L., Chunwei G., Ping Z. Calculation of a complex 3-D model of a turbogenerator with end region regarding electrical losses, cooling, and heating. *IEEE Transactions on Energy Conversion*, 2011, vol.26, no.4, pp. 1073-1080. **doi: 10.1109/tec.2011.2161610**.

Received 11.11.2019

Yu.M. Vaskovskyi[1], *Doctor of Technical Science, Professor,*
O.A. Geraskin[1], *Candidate of Technical Science, Associate Professor,*
[1] National Technical University of Ukraine «Igor Sikorsky Kyiv Polytechnic Institute»,
37, Prospect Peremohy, Kyiv-56, 03056, Ukraine,
e-mail: vun157@gmail.com

How to cite this article:
Vaskovskyi Yu.M., Geraskin O.A. Turbogenerator rotor heating in presence of rotor winding defects and excitation current forcing. *Electrical engineering & electromechanics*, 2020, no.1, pp. 10-15. **doi: 10.20998/2074-272X.2020.1.02.**

UDC 621.313 **doi: 10.20998/2074-272X.2020.1.03**

V.V. Goman, S.Kh. Oshurbekov, V.M. Kazakbaev, V.A. Prakht, V.A. Dmitrievskii

COMPARISON OF ENERGY CONSUMPTION OF VARIOUS ELECTRICAL MOTORS OPERATING IN A PUMPING UNIT

Purpose. Comparative analysis of energy consumption of various types electric motors in fixed speed centrifugal industrial pump applications is carried out. The purpose of the analysis is to choose the most efficient motor in the considered application. It is assumed that hydraulic flow of the pump is adjusted by throttling. The rated power of the pump unit is 2.2 kW. Direct on line motors of various energy efficiency classes from various manufacturers are considered: induction motors with permanent magnets on the rotor of IE4 class and squirrel cage induction motors of IE3 and IE4 classes. Methodology. Assessment of energy consumption of the motors is carried out based on the catalogue data from manufacturers of the pump and the motors. Pump hydraulic equations, interpolation of motor catalogue data and statistical data are also used. Results. The following values have been obtained: annual and daily energy consumption of the motors and electricity cost savings comparing with the least effective motor considered. Practical value. The following practical consideration are presented based on the theoretical results: choosing the motor based only on its IE efficiency class according to IEC 60034-30-1 is not enough to ensure the minimum energy consumption of pump units with variable flow during the load cycle. In addition, the energy consumption may be higher in the case of permanent magnet motors of IE4 class in comparison with induction motors of IE4 or even IE3 class. Therefore, it is necessary to take into account efficiency of the motors at underload and it is needed to calculate the energy consumption during the actual load cycle. It should be noted, that the existing approach based on the Energy Efficiency Index (EEI) calculation does not provide information about absolute values of energy savings and cost savings, in contrast to the described approach. While choosing motors to run in the considered application it is also important to take into account that the motors with permanent magnets on the rotor have significantly higher price and very restricted starting capabilities comparing with induction motors. In addition, the production of rare earth magnets causes a significant environmental damage. References 40, tables 5, figures 6.
Key words: **centrifugal pump, induction motor, line-start permanent magnet synchronous motor (LSPMSM), efficiency class, energy efficiency, throttle control.**

Мета. Порівняльний аналіз енергоспоживання електродвигунів різних типів і класів енергоефективності в електроприводі відцентрового насоса потужністю 2,2 кВт системи водопостачання з дросельним регулюванням. Порівнювалися синхронні електродвигуни з прямим пуском і постійними магнітами на роторі класу енергоефективності IE4 і асинхронні електродвигуни класів енергоефективності IE4 і IE3 різних виробників. Методика. Розрахунок енергоспоживання проводився на основі даних насоса і електродвигунів, що надаються виробниками, і включав в себе розрахунок енергоспоживання відцентровим насосом в типовому робочому циклі, який передбачає роботу зі зниженими навантаженнями протягом тривалого часу. Результат. Отримано розрахункові дані по добовому і річному енергоспоживанню розглянутих електродвигунів в типовому робочому циклі насоса, річна вартість електроенергії виходячи з середньоєвропейського тарифу, економія в грошовому вираженні щодо найгіршого електродвигуна з розглянутих. Практичне значення. Показано, що вибір електродвигуна за КПД при найменшому навантаженні, тобто фактично на основі присвоєного відповідно до стандарту IEC 60034-30-1 класу енергоефективності IE, не призводить до мінімального енергоспоживання відцентрового насосного агрегату зі змінною подачею протягом типового робочого циклу. Також показано, що застосування в насосних агрегатах зі змінною витратою синхронних електродвигунів з прямим пуском і постійними магнітами класу IE4 в ряді випадків призводить до більшого енергоспоживання, ніж застосування асинхронних електродвигунів класу IE4, а іноді і класу IE3. Таким чином, при виборі класу енергоефективності електродвигуна як для насосного агрегату, так і для будь-якого іншого механізму, що працює значний час при знижених навантаженнях, слід проводити розрахунок енергоспоживання на підставі даних про типовий робочий цикл або з експериментальних даних. При цьому існуючий підхід, заснований на визначенні індексу енергетичної ефективності EEI, не дає інформації про економію електроенергії в натуральному і вартісному виразах, на відміну від описаного в роботі підходу. При виборі електродвигуна за принципом дії слід враховувати, крім енергоспоживання, те, що синхронні електродвигуни з постійними магнітами мають велику вартість, ніж асинхронні електродвигуни, є труднощі їх запуску при значному моменті інерції, а отримання магнітів з рідкоземельних металів пов'язане зі значним екологічним збитком. Бібл. 40, табл. 5, рис. 6.
Ключові слова: **відцентрові насоси, асинхронні електродвигуни, синхронні електродвигуни з прямим пуском і постійними магнітами, клас енергоефективності, коефіцієнт корисної дії, дросельне регулювання.**

Цель. Сравнительный анализ энергопотребления электродвигателей разных типов и классов энергоэффективности в электроприводе центробежного насоса мощностью 2,2 кВт системы водоснабжения с дроссельным регулированием. Сравнивались синхронные электродвигатели с прямым пуском и постоянными магнитами на роторе класса энергоэффективности IE4 и асинхронные электродвигатели классов энергоэффективности IE4 и IE3 различных производителей. Методика. Расчет энергопотребления проводился на основе данных насоса и электродвигателей, предоставляемых производителями, и включал в себя расчет энергопотребления центробежным насосом в типовом рабочем цикле, предполагающем работу с пониженными нагрузками в течение продолжительного времени. Результат. Получены расчетные данные по суточному и годовому энергопотреблению рассмотренных электродвигателей в типовом рабочем цикле насоса, годовая стоимость электроэнергии исходя из среднеевропейского тарифа, экономия в денежном выражении относительно наихудшего электродвигателя из рассмотренных. Практическое значение. Показано, что выбор электродвигателя по КПД при номинальной нагрузке, то есть

фактически на основе присвоенного в соответствии со стандартом IEC 60034-30-1 класса энергоэффективности IE, не приводит к минимальному энергопотреблению центробежного насосного агрегата с переменной подачей в течение типового рабочего цикла. Также показано, что применение в насосных агрегатах с переменным расходом синхронных электродвигателей с прямым пуском и постоянными магнитами класса IE4 в ряде случаев приводит к большему энергопотреблению, чем применение асинхронных электродвигателей класса IE4, а иногда и класса IE3. Таким образом, при выборе класса энергоэффективности электродвигателя как для насосного агрегата, так и для любого другого механизма, работающего значительное время при пониженных нагрузках, следует проводить расчет энергопотребления на основании данных о типовом рабочем цикле либо экспериментальных данных. При этом существующий подход, основанный на определении индекса энергетической эффективности EEI, не дает информации об экономии электроэнергии в натуральном и стоимостном выражениях, в отличие от описанного в работе подхода. При выборе электродвигателя по принципу действия следует учитывать помимо энергопотребления, то, что синхронные электродвигатели с постоянными магнитами имеют большую стоимость, чем асинхронные электродвигатели, имеются трудности их запуска при значительном моменте инерции, а получение магнитов из редкоземельных металлов сопряжено со значительным экологическим ущербом. Библ. 40, табл. 5, рис. 6.

Ключевые слова: **центробежные насосы, асинхронные электродвигатели, синхронные электродвигатели с прямым пуском и постоянными магнитами, класс энергоэффективности, коэффициент полезного действия, дроссельное регулирование.**

Introduction. The widely known advantages of variable frequency drives (VFDs) are high efficiency and high dynamic and static characteristics, such as stiffness, control range, and the accuracy of maintaining adjustable values.

However, the proportion of variable frequency drives according to the European Commission [1] for Germany was about 30 %, and for Switzerland according to the study described in [2] was about 20 %.

Thus, in many applications, electric motors powered directly from the electrical network are widely used.

In particular, such common mechanisms as centrifugal pumps, compressors and fans do not require a wide range of regulation, high starting torque and speed. Therefore, asynchronous electric motors (IMs), operating directly from the network, are widely used in the drives of the mentioned turbo-mechanisms. A number of manufacturers also propose the use of line-start permanent magnet synchronous motor (LSPMSMs) of high energy efficiency class, powered directly from the network. In this case, the pump performance is regulated by means of valves (throttle control), by means of a controlled change in the characteristics of the hydraulic network.

According to the International Energy Agency [3], electric motors consume 46 % of the electricity generated in the world. They account for about 70 % of total industrial electricity consumption. According to the report of the European Commission [3], pumping systems account for almost 22 % of the energy supplied by electric motors in the world, as shown in Fig. 1. Therefore, the study of the possibilities of increasing the energy efficiency of pumping units is an urgent task.

Improving the energy efficiency of the pumping unit is possible due to changes in the hydraulic network for which the unit is operating, the use of control systems, including VFD, load optimization and distribution (in the case of parallel-running units), as well as due to the proper selection of the unit's components, in particular the use of electric motors more high class energy efficiency [4]. The last mentioned method is studied in this paper, as the most relevant for pumps with throttle control.

The minimum level of energy efficiency of electric motors is defined in Appendix I to [5]. Energy efficiency classes are based on the values specified in [6]. In accordance with the EU regulation [5] since January 1, 2017, all electric motors with power from 0.75 to 375 kW must have an energy efficiency class of at least IE3 or IE2, if they are used as part of the VFD. Until 2030, according to Policy Option 4 [7], one should expect the introduction of the minimum acceptable energy efficiency class not lower than IE4.

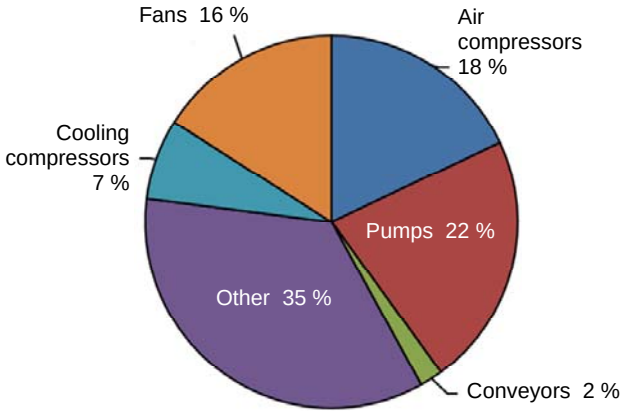

Fig. 1. Power consumption for various applications

The classification of electric motors in [5, 6] is based only on efficiency in the nominal operating mode, that is, at rated power on the shaft, but does not take into account the efficiency of electric motors at partial load, which is typical for electric motors in pumping units [8].

In practice, most of the time centrifugal pumping units are operated at low or medium loads which occurs due to changes in the number of people in buildings and/or atmospheric conditions, while the pumps are designed to satisfy maximum loads [9]. In [10], it was estimated that 75 % of centrifugal pumping units have an overestimated power, many of them more than 20 %. In [11] it was estimated that only 20 % of electric motors in pumps operate at rated power.

The publications [12, 13] compare the energy consumption of the pumping unit with electric motors of different types and classes IE with VFD, since frequency regulation achieves significant energy savings, especially under low loads. Nevertheless, in view of the mass application of unregulated electric drives that has been

preserved in many industries, a number of works compare the characteristics of electric motors that operate directly from the network. For example, in the paper [14], a comparative analysis of the energy efficiency class IE3 IM and LSPMSM as a part of the fan in start-up and in steady-state modes was carried out. This analysis showed that the efficiency and power factor of LSPMSM are significantly higher than that of IM. However, the analysis was carried out for nominal load conditions. The paper [15] discusses the operation of LSPMSM as part of the pumping unit. The characteristics of the proposed design of the electric motor are compared with the simulation results in the nominal mode of the pumping unit under start-up conditions with high moment of inertia. In paper [16], the design and the characteristics of the steady-state and transient modes of operation of the IM and LSPMSM with power of 2.2 kW in the nominal mode and at idle are considered. For the operating mode with rated power, an indicator of annual cost savings is determined in the case of using LSPMSM.

One of the main conclusions of publications [13-16] is the advantage of LSPMSM over IM in such parameters as efficiency and power factor. Note, however, that in these publications, the comparison of IM and LSPMSM was carried out mainly for operating modes with a nominal load. This paper discusses the modes of operation of IM and LSPMSM as part of a pumping unit with variable load, depending on water consumption, for example, in a large building. The work calculates the energy consumption of electric drives at loads different from the rated load of the electric motor, and the obtained data are compared to assess the energy saving potential of electric motors of energy efficiency classes IE3 and IE4.

Due to the fact that the energy efficiency class IE of the electric motor is assigned according to efficiency in nominal mode in accordance with IEC 60034-30-1 [6], but in HVAC (Heating, Ventilation, & Air Conditioning) applications an electric motor in this mode works only a small fraction of the time, the main goal of this paper is to determine the criterion for choosing electric motors under the condition of minimum energy consumption, taking into account the actual operating conditions of centrifugal pumping units.

Characteristics of the pumping unit and electric motors. The drive of the pumping unit with one electric motor, powered directly from the electric network, is shown in Fig. 2 [8]. It consists of a centrifugal pump, which is connected to an electric motor without intermediate mechanical gears.

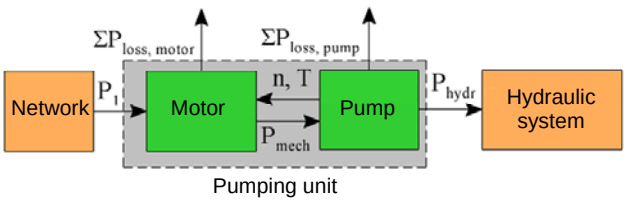

Fig. 2. Diagram of an unregulated pumping unit

The active power P_1 consumed by the drive is converted by the electric motor into the mechanical power P_{mech}. Power P_{mech} is less than P_1 by the value of losses in the electric motor [8]:

$$P_{mech} = P_1 - \Sigma P_{loss.m}, \quad (1)$$

where $\Sigma P_{loss.m}$ are the total losses of the electric motor.

The mechanical power of the electric motor P_{mech} is transmitted to the pump and, therefore, in the absence of intermediate mechanical gears, is equal to the input mechanical power of the pump. In the pump, the mechanical power P_{mech} is converted to the hydraulic power P_{hydr}. The difference between P_{mech} and P_{hydr} is the value of the total losses $\Sigma P_{loss.pump}$ in the pump [8]:

$$P_{hydr} = P_{mech} - \Sigma P_{loss.pump}. \quad (2)$$

The hydraulic power is determined by the flow rate Q and the pump head H_{pump}. The pump head depends on the flow rate in accordance with the Q–H characteristic of the pump at a given pump rotation speed n. Therefore, the required electric power P1 depends on the flow rate Q [8]:

$$P_1 = \rho g Q H_{pump} + \Sigma P_{loss.pump} + \Sigma P_{loss.m}, \quad (3)$$

where ρ is the fluid density, g is the acceleration of gravity.

To compare the energy consumption of the electric motors of the pumping unit when regulating the flow rate using a valve, the centrifugal pump NM4 40/25B (manufactured by Calpeda) with power of 2.2 kW and rated rotation speed n = 1450 rpm was considered [17]. Pump data are given in Table 1, where Q_{BEP} is the flow rate at the best efficient point (*BEP*), H_{BEP} is the pressure at *BEP*.

Table 1

Passport characteristics of the pump [17]

Parameter	Value
Type	NM4 40/25B
P, W	2200
n, rpm	1450
Q_{BEP}, m³/h	19
H_{BEP}, m	17.8
Efficiency, %	60

The calculation was carried out for 8 different 4-pole electric motors with power of 2.2 kW, namely: three IE4 class LSPMSMs powered from the network (Bharat Bijlee SynchroVERT [18], WEG [19], SEW-Eurodrive [20]), two class IE4 IMs (Siemens [21] and WEG [22]) and three class IE3 IMs (Siemens [21], WEG [23] and ABB [24]). Data on the value of the efficiency of electric motors are given in Table 2.

Table 2

Efficiency of 4-pole electric motors of power of 2.2 kW [18-24]

m	Type	Class	Efficiency, % at load, %		
			50 %	75 %	100 %
1	LSPMSM SEW DRU J	IE4	88.0	90.5	91.2
2	LSPMSM SynchroVERT	IE4	88.6	89.4	89.5
3	LSPMSM WEG WQuattro	IE4	86.0	89.0	90.2
4	IM Siemens 1LE1004	IE4	88.3	89.6	89.5
5	IM WEG W22	IE4	88.5	89.5	89.5
6	IM Siemens 1LE1003	IE3	86.4	87.3	86.7
7	IM WEG W21	IE3	86.5	87.0	87.0
8	IM ABB M3BP	IE3	85.1	86.9	86.7

Assessment of energy consumption of the pumping unit. The operation of the pumping unit is considered in modes where the water flow rate during the cycle of the pumping unit varies, in accordance with the hydraulic load characteristic of HVAC applications. A typical pump operation cycle (Fig. 3), defined by EU regulation [25], is divided into 4 modes. A feature of the cycle is that most of the time the pump operates at a flow rate much less than the nominal. For example, with a flow rate of 25 % of the nominal, the pump operates during the relative time t_i/t_Σ = 44 %, where t_Σ is the total operating time, taken equal to 24 hours, t_i is the pump operation time in this mode. Here, the relative operating time in the nominal mode does not exceed 6 %. This load profile is typical for pumping systems with the need to vary the flow rate over a wide range (systems with variable flow rate) [6].

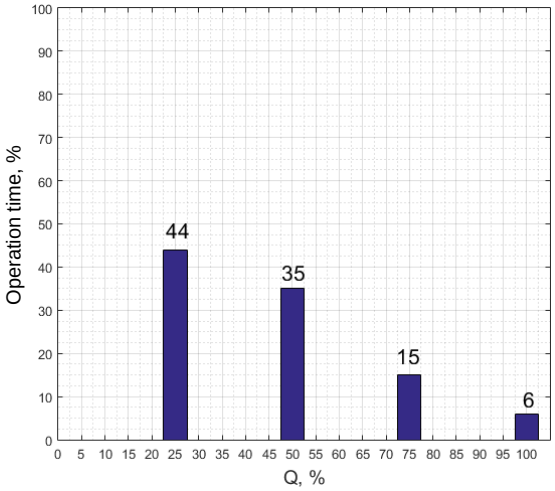

Fig. 3. Time dependence of water flow rate per cycle

The electric motor is directly connected to the network, that is, the motor speed is not controlled by the frequency converter during the cycle, and the pump flow rate Q is controlled by the valve. The water pressure in this case changes in accordance with the Q–H curve of the pump, and the operating point is the intersection point of the pump characteristic and the hydraulic system characteristic. Figure 4 shows the results of the Q–H characteristic interpolation for the selected pump and the starting points according to the manufacturer [17], as well as the pump power in the operating range of flow rates.

The pump power curve as a function of flow rate is given by the pump manufacturer (Fig. 4). According to this curve, the pump power was determined in 4 standard operating modes (25 %, 50 %, 75 %, 100 % of the flow rate). A flow rate corresponding to 100 % was determined from the pump efficiency curve [17] as corresponding to the maximum efficiency. Based on the known passport values of the efficiency of electric motors (Table 2), by means of polynomial interpolation of the loss curve $\Sigma P_{\text{loss.m}}$ of each electric motor, the efficiency values for four operating modes of the pumping unit were determined. As shown in [27], the dependence of the electric motor losses on the load is well described by a second-order polynomial, whose coefficients can be easily obtained from 3 points of the initial data on the efficiency of electric motors.

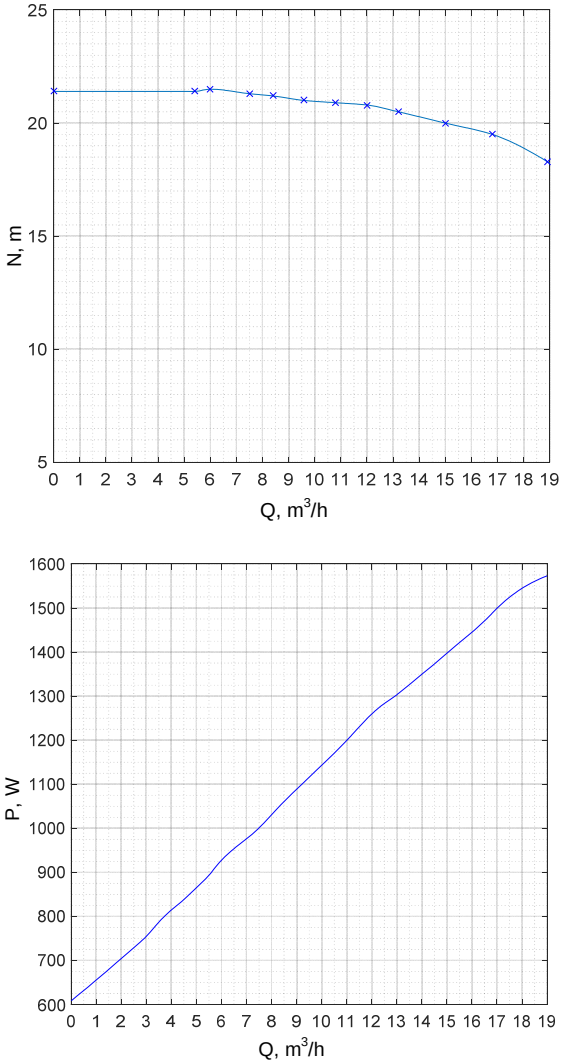

Fig. 4. Q-H – pump characteristic and power versus flow rate dependence

The obtained values of the efficiency for each electric motor $\eta_{\text{m}.i.m}$ are given in Table 3 which also indicates for each operating mode: flow rate, pump pressure, pump power, electric motor output power as a percentage of the nominal.

Active electric power consumed from the network in each mode was calculated according to expression (4)

$$P_{1.i.m} = P_{\text{mech}.i.m} / \eta_{\text{m}.i.m}, \quad (4)$$

где $\eta_{\text{m}.i.m}$ is the efficiency of the m-th electric motor in the i-th mode of operation.

The calculation results are given in Table 4.

The daily energy consumption of each electric motor (kW·h) for the full cycle of the pumping unit in accordance with the considered load profile is determined by the expression

$$E_{d.m} = \frac{t_\Sigma}{1000} \cdot \sum_{i=1}^{4} (P_{1.i.m} \cdot t_i / t_\Sigma). \quad (5)$$

At year-round operation of the pump unit, the annual energy consumption can be calculated as:

$$E_{\text{y.m}} = E_{\text{d.m}} \cdot 365. \quad (6)$$

Table 3

Interpolated motor efficiency values

i	1	2	3	4
Q_i, %	25	50	75	100
Q_i, m^3/h	4.75	9.50	14.25	19.00
$H_{\text{pump}.i}$, m	21.4	21.0	20.2	17.8
$P_{\text{mech}.i}$, W	851	1116	1361	1573
$P_{\text{mech}.i}$, %	38.7	50.7	61.9	71.5
Efficiency $\eta_{\text{m}.i.m}$, %				
i	1	2	3	4
LSPMSM SEW DRU J	85.5	88.1	89.5	90.3
LSPMSM SynchroVERT	87.7	88.6	89.1	89.3
LSPMSM WEG WQuattro	83.3	86.1	87.8	88.7
IM Siemens 1LE1004	86.7	88.4	89.2	89.5
IM WEG W22	85.8	88.2	89.3	89.7
IM Siemens 1LE1003	84.9	86.5	87.1	87.3
IM WEG W21	84.8	86.3	86.9	87.2
IM ABB M3BP	82.7	85.2	86.3	86.8

The cost of electricity consumed (Euro) taking into account the adopted average European electricity tariff GT = 0.1149 €/kW·h for non-household consumers in the second half of 2018 [28], is calculated as

$$C_{\text{y.m}} = E_{\text{y.m}} \cdot GT. \quad (7)$$

To compare the energy consumption and the cost of electricity consumed by pumping units with various electric motors, the expression (8) were used to calculate the differences in the cost of electricity relative to the pumping unit with the electric motor with the highest energy consumption at the considered load profile (motor No. 8 of IE3 class manufactured by ABB)

$$S_{\text{y.m}} = C_{\text{y.8}} - C_{\text{y}(1\ldots7)}, \quad (8)$$

The results of calculations by formulas (4)-(8) are summarized in Table 4, 5, and are also shown in Fig. 5, 6.

Table 4

Power consumption $P_{1.i,m}$, W

i	1	2	3	4
LSPMSM SEW DRU J	996.2	1266.1	1520.3	1742.3
LSPMSM Synchro-VERT	971.3	1258.6	1527.4	1760.8
LSPMSM WEG WQuattro	1022.6	1295.2	1550.9	1773.1
IM Siemens 1LE1004	982.2	1262	1526.3	1757.5
IM WEG W22	992.9	1264.8	1524.4	1753.8
IM Siemens 1LE1003	1003.1	1289.9	1562.5	1802.5
IM WEG W21	1004.4	1293.1	1566	1805
IM ABB M3BP	1029.4	1309.4	1576.4	1812.2

Table 5

Cost characteristics of power consumption

Type	$E_{\text{d.m}}$, kW·h	$E_{\text{y.m}}$, kW·h	$C_{\text{y.m}}$, €	$S_{\text{y.m}}$, €
LSPMSM SEW DRU J	29.1	10635	2113.1	73.8
LSPMSM SynchroVERT	28.9	10535	2093.3	93.6
LSPMSM WEG WQuattro	29.8	10882	2162.3	24.6
IM Siemens 1LE1004	29	10585	2103.1	83.8
IM WEG W22	29.1	10630	2112.1	74.8
IM Siemens 1LE1003	29.6	10822	2150.3	36.6
IM WEG W21	29.7	10843	2154.4	32.5
IM ABB M3BP	30.2	11006	2186.9	0

The graph in Fig. 5 shows that the electric motor No. 3 – LSPMSM of class IE4 in the cycle under consideration, which is typical for pumps with variable flow rate, consumes more electricity than IMs of class IE3 No. 6 and No. 7, but less than the class IE3 IM No. 8. So, according to Fig. 6, this IE4 class electric motor provides lower cost savings than IE3 class electric motors No. 6 and No. 7. LSPMSMs No. 1 and No. 2 have energy consumption indicators that approximately coincide with class IE4 IMs No. 4 and No. 5. The smallest energy consumption has electric motor No. 2 – LSPMSM SynchroVERT, and the largest – electric motor No. 8, the IM AB.

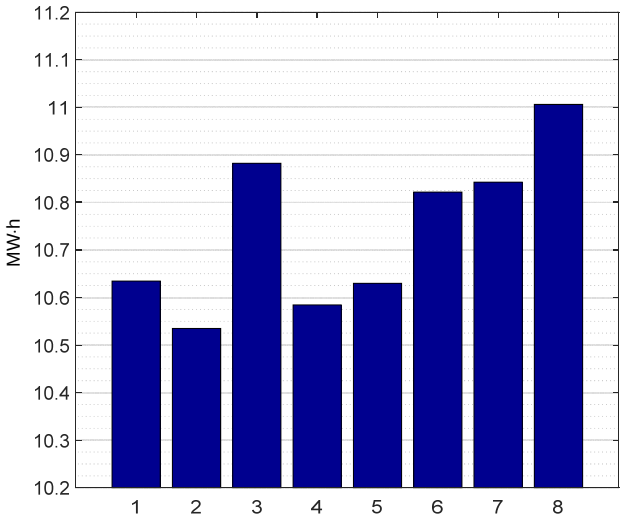

Fig. 5. Annual energy consumption:
1 – LSPMSM IE4 SEW DRU J; 2 – LSPMSM IE4 Synchrovert; 3 – LSPMSM IE4 Weg WQuattro; 4 – IM IE4 Siemens 1LE1004; 5 – IM IE4 Weg W22; 6 – IM IE3 Siemens 1LE1003; 7 – IM IE3 Weg W21; 8 – IM IE3 ABB M3BP

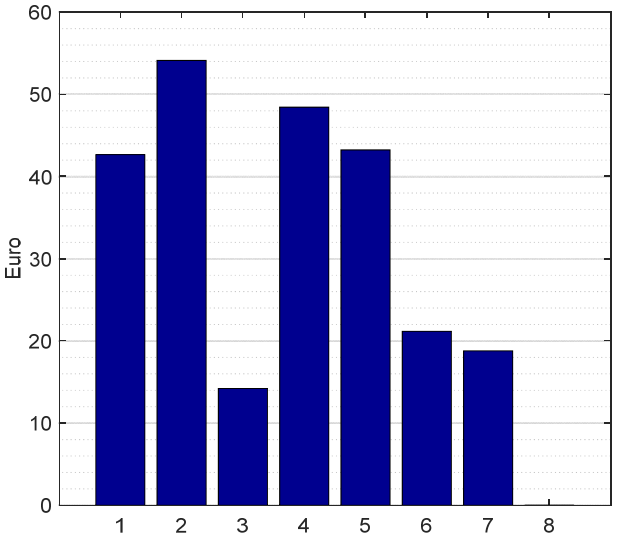

Fig. 6. Saving energy costs relative to electric motor No. 8: 1 – LSPMSM IE4 SEW DRU J; 2 – LSPMSM IE4 Synchrovert; 3 – LSPMSM IE4 Weg WQuattro; 4 – IM IE4 Siemens 1LE1004; 5 – IM IE4 Weg W22; 6 – IM IE3 Siemens 1LE1003; 7 – IM IE3 Weg W21; 8 – IM IE3 ABB M3BP

The results shown in Fig. 5, 6 are the consequence of the fact that according to the adopted standard [6], electric motors are classified according to energy consumption in accordance with the value of efficiency in the nominal mode of operation, at a load equal to 100 %. However, in pumping units, electric motors operate for a significant part of the time at a load 2...4 times less than the nominal and as a result have a reduced efficiency. Here, the existing standards do not establish the minimum values of the efficiency of electric motors powered directly from the network at loads below nominal.

Thus, the selection of an electric motor based on its energy efficiency class IE, in a number of applications, such as variable flow rate pumps, will not lead to minimum energy consumption. Note that for frequency-controlled electric motors, the IEC 60034-30-2 Standard [29] defines the efficiency values in seven load modes different from the nominal one. In the draft version of IEC 60034-30-2 [30], it was proposed for frequency-controlled electric motors of pumps and fans (drives with a quadratic dependence of the load on speed) to calculate the total efficiency as an average weighted average indicator of efficiency at reduced speeds and loads.

Therefore, when choosing an electric motor for a pumping unit operating with a variable flow rate, you can not be guided only by the energy efficiency class IE and the nominal value of the efficiency, but it is worthwhile to calculate the energy consumption depending on the operating modes or focus on the energy efficiency index of the pumping unit (see below).

It is worth noting that LSPMSMs have a higher cost than IMs (especially IE3 class), due to the presence of expensive rare-earth magnets in the design. Production of magnets from rare-earth metals is associated with significant environmental damage, for example in [31] it is indicated that the production of each ton of material for rare-earth magnets is associated with the generation of 1-1.4 tons of radioactive waste. Only a small part of these wastes contains rare-earth elements and is further processed to extract them [31]. There is also technological dependence on rare-earth suppliers from China, since more than 95 % of the global production of rare earth elements is controlled by China [32]. Due to the monopoly of China, the prices of rare-earth elements are unstable and can change several times over several years [33].

We also note the difficulties of starting LSPMSMs at significant moment of inertia of the load, which significantly limits their scope. A review of modern papers on LSPMSMs [34-37] shows that the maximum load inertia moment for such electric motors is relatively small and insufficient to start and reach rated speed, for example, for a turbo-mechanism with a steel impeller. These electric motors are not able to start with many typical mechanisms, such as: reciprocating compressors, screw compressors, plunger pumps, conveyors, escalators, etc. [34-37].

According to the results of comparing LSPMSMs and IMs classes IE3 and IE4, described in [38] LSPMSMs show a higher peak value of the starting current, which can cause the operation of typical circuit breakers. Inrush currents can cause unwanted switches off and can damage contactors, fuses and protective devices, such as circuit breakers or switchgears [38]. In this case, starting with star-delta switching or using electronic soft starters is not recommended or not possible for LSPMSMs [38]. Also, LSPMSMs are much more sensitive to voltage drop [38] and more sensitive to phase asymmetry [38].

Taking into account the above-mentioned drawbacks of LSPMSMs, it is more justified at the present time to use in applications with a variable load, which is very different from the nominal mode, of IMs class of IE4, and not LSPMSMs.

Calculation and assessment of the energy efficiency index of the pumping unit in accordance with existing standards. The energy efficiency of circulation pumps operating primarily with variable flow rate is evaluated in accordance with EU regulations [25]. In this document, the profile indicated in Fig. 3, according to which the above calculations were carried out is accepted as a typical pump load profile. According to [8], the energy efficiency index (*EEI*) is well established for evaluating the energy efficiency of circulation pumps and is now proposed for other pump applications.

That is, *EEI* is the most suitable indicator for assessing the energy efficiency of variable-flow pump systems for various purposes, in contrast to the minimum efficiency index (*MEI*), which is defined in [39] and is based on efficiency values in a relatively limited range of operating points (75...110 % flow rates) [8].

According to the approach of the Europump association [26, p. 12] and [40] *EEI* is defined by:

$$EEI = P_{1.avg} / P_{1.ref}, \quad (9)$$

where $P_{1.avg}$ is the weighted average value of the electric power consumed by the pump, which is determined by the following expression [25]:

$$P_{1.\text{avg}} = \sum_{i=1}^{4} \left[(t_i / t_\Sigma) \cdot P_{1.i} \right]. \quad (10)$$

The denominator in the expression (9) $P_{1.\text{ref}}$ is the electric power of the «reference» system, which according to [26, 40] is determined by the expression

$$P_{1.\text{ref}} = P_{\text{hydr.ref}} / (\eta_{\text{motor.ref}} \cdot \eta_{\text{pump.min.req}}). \quad (11)$$

In both expressions, $P_{\text{hydr.ref}}$ is the hydraulic power of the reference system, which is defined as the product of the flow rate Q_{BEP} (m³/s) and pressure H_{BEP} (Pa): in this case, $P_{\text{hydr.ref}} = 921.6$ W.

In expression (11) $\eta_{\text{motor.ref}}$ is the efficiency of the reference electric motor, which was taken equal to the efficiency of a 4-pole electric motor with power of 2.2 kW energy efficiency class IE3 according to [6] ($\eta_{\text{motor.ref}} = 86.7$ %); $\eta_{\text{pump.min.req}}$ is the minimum required efficiency of the reference pump at the best efficient point [39], depending on the tabular coefficient C, determined by the type of pump, the rated rotation speed of the pump n and its energy efficiency, flow rate Q_{BEP} and specific rotation speed n_s, in turn dependent on H_{BEP} and n. A detailed calculation of $\eta_{\text{pump.min.req}}$ is not given in this paper, the calculation result: $\eta_{\text{pump.min.req}} = 50.66$ %.

According to formula (11), the value of $P_{1.\text{ref}}$ = = 2098.23 W in this case.

The calculation results for expressions (9)-(11) are given in Table 6.

Table 6 shows that the *EEI* values for the pumping unit with various electric motors correspond to the patterns shown in Fig. 5, 6. Thus, *EEI* characterizes the energy consumption of the pumping unit more objectively than the energy efficiency class of the electric motor (IE), which depends only on the efficiency in the nominal mode.

Table 6

Energy efficiency index determination for pumping system

m	Type	$P_{1.\text{avg}}$, W	*EEI*
1	LSPMSM SEW DRU J	1214.0	0.5786
2	LSPMSM SynchroVERT	1202.6	0.5732
3	LSPMSM WEG WQuattro	1242.3	0.5921
4	IM Siemens 1LE1004	1208.3	0.5759
5	IM WEG W22	1213.4	0.5784
6	IM Siemens 1LE1003	1235.4	0.5888
7	IM WEG W21	1237.7	0.5899
8	IM ABB M3BP	1256.4	0.5988

Note that for circulation pumps, which are the subject of EU regulations [25], since 2005 there is a voluntary labeling of products by members of the Europump association using the letters *A*...*G* of the energy efficiency class. It seems relevant to introduce such labeling for industrial pumping units operating at variable flow rates.

Conclusions.

A comparative analysis of the energy consumption of electric motors of various types (LSPMSMs and IMs) and energy efficiency class (IE3 and IE4) as a part of a 2.2 kW variable-flow pumping unit with throttle regulation is carried out in the work. The approach used to compare the energy characteristics of electric motors is described, including the calculation of the energy consumption of the pumping unit in a typical operation cycle with various process loads. Electric power, energy consumption and cost savings for 8 electric motors have been calculated.

Using the results of the calculation according to the described method, based on the passport data of electric motors and pumps, it has been shown that the use of an electric motor with high efficiency at rated load (high energy efficiency class according to [6]) does not always provide the minimum power consumption in a variable speed pump unit's operation cycle.

It is noted in the paper that it is possible to select the best electric motor according to a technique based on the determination of the energy efficiency index *EEI* [26], since the mode of operation of the pumping unit is also taken into account in its calculation. However, the calculated value of *EEI* does not provide information on energy savings in physical and cost terms, in contrast to the approach described in the work.

It is also shown in the paper that the considered LSPMSMs of IE4 class do not have significant advantages over IMs of IE4 class, and sometimes also of IE3 class, if used in pumping units with variable flow rate.

Acknowledgment.

The results of the work have been obtained with the support of the Ministry of Education and Science of the Russian Federation, task No. 8.9549.2017/8.9.

REFERENCES

1. De Almeida A.T. et al. *EuP Lot 11 Motors, Final report to the European Commission*, 2008.

2. Phillips R., Tieben R. Improvement of Electric Motor Systems in Industry (IEMSI). *Proceedings of the 10th international conference on energy efficiency in motor driven systems (EEMODS' 2017)*, Rome, Italy, September 6-8, 2017. pp. 53-67. **doi: 10.2760/345473**.

3. *European Commission. Study on improving the energy efficiency of pumps*, 2001.

4. Arun Shankar V.K., Umashankar S., Paramasivam S., Hanigovszki N. A comprehensive review on energy efficiency enhancement initiatives in centrifugal pumping system. *Applied Energy*, 2016, vol. 181, pp. 495-513. **doi: 10.1016/j.apenergy.2016.08.070**.

5. *European Commission Regulation (EC) No. 640/2009 implementing Directive 2005/32/ EC of the European Parliament and of the Council with Regard to Ecodesign Requirements for Electric Motors*, (2009), amended by Commission Regulation (EU) No 4/2014 of January 6, 2014.

6. *Rotating electrical machines – Part 30-1: Efficiency classes of line operated AC motors (IE code)*. IEC 60034-30-1/ Ed. 1; IEC: 2014-03.

7. De Almeida A., Fong J., Falkner H. New European ecodesign regulation proposal for electric motors and drives. *Proceedings of the 9th International Conference on Energy Efficiency in Motor Driven Systems (EEMODS' 15)*, Helsinki, Finland, September 15-17, 2015. **doi: 10.2790/903731**.

8. Stoffel B. *Assessing the Energy Efficiency of Pumps and Pump Units. Background and Methodology*. Elsevier: Amsterdam, The Netherlands, 2015. **doi: 10.1016/B978-0-08-100597-2.00009-4**.
9. Gevorkov L. *Simulation and Experimental Study on Energy Management of Circulating Centrifugal Pumping Plants with Variable Speed Drives*. PhD Thesys, Tallinn University of Technology, 2017.
10. Shuvalova J. *Optimal Approximation of Input-Output Characteristics of Power Units and Plants*. PhD Thesys, Tallinn University of Technology, 2004.
11. Glover A., Lukaszczyk M. Oversizing pump motors – the problems. *World Pumps*, 2005, vol. 2005, no. 466, pp. 36-38. **doi: 10.1016/s0262-1762(05)70638-6**.
12. Safin N., Kazakbaev V., Prakht V., Dmitrievskii V. Calculation of the efficiency and power consumption of induction IE2 and synchronous reluctance IE5 electric drives in the pump application based on the passport specification according to the IEC 60034-30-2. *2018 25th International Workshop on Electric Drives: Optimization in Control of Electric Drives (IWED)*, Jan. 2018. **doi: 10.1109/IWED.2018.8321381**.
13. Kazakbaev V., Prakht V., Dmitrievskii V., Ibrahim M., Oshurbekov S., Sarapulov S. Efficiency Analysis of Low Electric Power Drives Employing Induction and Synchronous Reluctance Motors in Pump Applications. *Energies*, 2019, vol. 12, no. 6, p. 1144. **doi: 10.3390/en12061144**.
14. Mutize C., Wang R-J. Performance comparison of an induction machine and line-start PM motor for cooling fan applications». *Proceedings of SAUPEC*, 2013. **doi: 10.13140/RG.2.1.2542.1922.**
15. Jian Li, Jungtae Song, Yunhyun Cho. High Performance Line Start Permanent Magnet Synchronous Motor for Pumping System. *IEEE International Symposium on Industrial Electronics*, 2010. **doi: 10.1109/ISIE.2010.5637082**.
16. Kahrisangi M.G., Isfahani A.H., Vaez-Zadeh S., Sebdani M.R. Line-start permanent magnet synchronous motors versus induction motors: A comparative study. *Frontiers of Electrical and Electronic Engineering*, 2012, pp. 2095-2732. **doi: 10.1007/s11460-012-0217-8.**
17. *NM, NMS, Close Coupled Centrifugal Pumps with Flanged Connections; Catalogue*; Calpeda, 2018. Available at: https://www.calpeda.com/system/products/catalogue_50hzs/53/en/NM_NMS_EN2018.pdf?1549893188 (accessed 23 March 2019).
18. *Catalogue of super premium efficiency SynchroVERT LSPM motors*. Available at: https://www.bharatbijlee.com/media/14228/synchrovert_catalogue.pdf (accessed 15 May 2019).
19. Available at: https://www.weg.net/catalog/weg/RU/en/Electric-Motors/Special-Application-Motors/Permanent-Magnet-Motors/Line-Start-PM-Motors/Wquattro-2-2-kW-4P-100L-3Ph-230-400-V-50-Hz-IC411---TEFC---B3T/p/13009386 (accessed 28 August 2019).
20. *Addendum to the operating instructions: AC Motors DR.71.J-DR.100.J with LSPM technology, 21281793/EN, 09/2014, SEW Eurodrive*. Available at: https://download.sew-eurodrive.com/download/pdf/21343799.pdf (accessed 20 August 2019).
21. *Catalog Siemens D81.1 Simotics GP, SD, XP, DP low-voltage motors, 05/2018*. Available at: www.siemens.com/drives/catalogs (accessed 27 August 2019).
22. Available at: https://www.weg.net/catalog/weg/MV/en/Electric-Motors/Low-Voltage-NEMA-Motors/General-Purpose-ODP-TEFC/Cast-Iron-TEFC-General-Purpose/W22-Super-Premium-Efficiency/W22-Super-Premium-Efficiency-3-HP-4P-182-4T-3Ph-208-230-460-380-V-60-Hz-IC411---TEFC---Foot-mounted/p/12792146 (accessed 28 August 2019).
23. Available at: https://www.weg.net/catalog/weg/RU/en/Electric-Motors/Low-Voltage-IEC-Motors/General-Purpose-ODP-TEFC/Aluminum-TEFC-General-Purpose/Aluminium-TEFC-General-Purpose/Multimounting-IE3/Multimounting-IE3-2-2-kW-4P-100L-3Ph-220-240-380-415-460-V-50-Hz-IC411---TEFC---B3T/p/12397774 (accessed 24 August 2019).
24. *Catalog ABB - Low Voltage General Performance motors, June 2018*. Available at: https://library.e.abb.com/public/00389a1977844886b7e3e7560a6c22bf/9AKK105789%20EN%2006-2018%20General%20Perf.pdf (accessed 14 May 2019).
25. *Commission Regulation (EC) No 641/2009* of July 22, 2009 implementing Directive 2005/32/EC of the European Parliament and of the Council with regard to ecodesign requirements for glandless standalone circulators and glandless circulators integrated in products, amended by Commission Regulation (EU) No 622/2012 of July 11, 2012.
26. *Extended product approach for pumps*, Copyright © 2014 by Europump. Published by Europump.
27. Ferreira F.J.T.E., De Almeida A.T. Energy savings potential associated with stator winding connection mode change in induction motors. *2016 XXII International Conference on Electrical Machines (ICEM)*, pp. 2775-2783. **doi: 10.1109/ICELMACH.2016.7732915.**
28. *Eurostat Data for the Industrial Consumers in Germany*. Available at: http://ec.europa.eu/eurostat/statistics-explained/index.php/Electricity_price_statistics#Electricity_prices_for_industrial_consumers (accessed 10 September 2019).
29. *Rotating electrical machines – Part 30-2: Efficiency classes of variable speed AC motors* (IE-code) IEC 60034-30-2/ IEC: 2016-12.
30. *Rotating electrical machines – Part 30-2: Efficiency classes of variable speed AC motors* (IE-code) IEC 60034-30-2 (draft). Available at: https://www.iec.ch/dyn/www/f?p=103:52:0::::FSP_ORG_ID,FSP_DOC_ID,FSP_DOC_PIECE_ID:1221,151336,279593 (accessed on 17 September 2019).
31. W. Ismar Borges de Lima, editor. *Rare Earth Industry*. Elsevier, 2015. **doi: 10.1016/C2014-0-01863-1**.
32. Dent P.C. Rare earth elements and permanent magnets (invited). *Journal of Applied Physics*, 2012, vol. 111, no. 7, p. 07A721. **doi: 10.1063/1.3676616**.
33. Goss J., Popescu M., Staton D. A comparison of an interior permanent magnet and copper rotor induction motor in a hybrid electric vehicle application. *Proceedings of IEEE International Electric Machines & Drives Conference, EMDC 2013*, Chicago, IL, USA. **doi: 10.1109/IEMDC.2013.6556256**.
34. Ismagilov F.R., Vavilov V.E., Gusakov D.V. Line-Start Permanent Magnet Synchronous Motor for Aerospace Application. *2018 IEEE International Conference on Electrical Systems for Aircraft, Railway, Ship Propulsion and Road Vehicles & International Transportation Electrification Conference (ESARS-ITEC)*, Nov. 2018. **doi: 10.1109/ESARS-ITEC.2018.8607689**.
35. Sorgdrager A.J., Wang R.-J., Grobler A.J. Multiobjective Design of a Line-Start PM Motor Using the Taguchi Method. *IEEE Transactions on Industry Applications*, 2081, vol. 54, no. 5, pp. 4167-4176. **doi: 10.1109/TIA.2018.2834306**.

36. Kurihara K., Rahman M.A. High-Efficiency Line-Start Interior Permanent-Magnet Synchronous Motors. *IEEE Transactions on Industry Applications*, 2004, vol. 40, no. 3, pp. 789-796. **doi: 10.1109/TIA.2004.827476**.

37. Niaz Azari M., Mirsalim M. Line-start permanent-magnet motor synchronisation capability improvement using slotted solid rotor. *IET Electric Power Applications*, 2013, vol. 7, no. 6, pp. 462-469. **doi: 10.1049/iet-epa.2013.0042**.

38. Ferreira F.J.T.E., Leprettre B., de Almeida A.T. Comparison of protection requirements in IE2- IE3- and IE4-class motors. *IEEE Transactions on Industry Applications*, 2016, vol. 52, no. 4, pp. 3603-3610. **doi: 10.1109/TIA.2016.2545647**.

39. *Commission regulation (EU) No 547/2012* of June 25, 2012 implementing Directive 2009/125/EC of the European Parliament and of the Council with regard to ecodesign requirements for water pumps.

40. Lang S., Ludwig G., Pelz P.F., Stoffel B. *General methodologies of determining the Energy Efficiency Index of pump units in the frame of the Extended Product Approach*. Rio de Janeiro, EEMODS, 2013. **doi: 10.2790/28891**.

Received 29.10.2019

V.V. Goman[1], *Candidate of Technical Science,*
S.Kh. Oshurbekov[2],
V.M. Kazakbaev[2], *Candidate of Technical Science,*
V.A. Prakht[2], *Candidate of Technical Science,*
V.A. Dmitrievskii[2], *Candidate of Technical Science,*
[1] Nizhny Tagil Technological Institute (branch)
of Ural Federal University,
59, Krasnogvardeiskaia Str., Nizhny Tagil,
Sverdlovsk Region, 622013, Russia,
e-mail: v.v.goman@urfu.ru
[2] Ural Federal University,
19, Mira Str., Ekaterinburg, 620002, Russia,
e-mail: s.oshurbekov@mail.ru, vadim.kazakbaev@urfu.ru,
va.prakht@urfu.ru, vladimir.dmitrievsky@urfu.ru

How to cite this article:
Goman V.V., Oshurbekov S.Kh., Kazakbaev V.M., Prakht V.A., Dmitrievskii V.A. Comparison of energy consumption of various electrical motors operating in a pumping unit. *Electrical engineering & electromechanics*, 2020, no.1, pp. 16-24. **doi: 10.20998/2074-272X.2020.1.03.**

UDC 621.313 **doi: 10.20998/2074-272X.2020.1.04**

Yu.V. Shurub, Yu.L. Tsitsyurskiy

HARMONIC ANALYSIS OF THE COMBINED CIRCUIT OF SINGLE-PHASE SWITCHING OF INDUCTION ELECTRIC DRIVE WITH THYRISTOR CONTROL

Purpose. *The purpose of this article is to provide a comparative analysis of influence of the phase controlled single-phase induction electric drive coordinates harmonic components on the operational characteristics of the electric drive under different variants of the power part.* ***Methodology.*** *A mathematical model of the combined circuit of a single-phase induction motor with a variable structure of the power part and a constant capacitance of the phase-shifting capacitor is generalized for various variants of connection of the power part of the electric drive with thyristor control. The comparative harmonic analysis of currents and torques of the motor is carried out and the factors influencing the energy efficiency of the electric drive at different circuit of connection of the power part are determined.* ***Results.*** *The analysis of the obtained data shows that the series-parallel circuit has the best harmonic composition of the consumed current in practically the whole range of changes of load torque and speed. The main effect on the loss increase is due to the asymmetry of the currents in the series-parallel circuit and the higher harmonics in the Steinmetz circuit.* ***Originality.*** *For the analysis of the processes in these circuits, a generalized thyristor control single-phase electric drive mathematical model, in which the structure of differential equations remains unchanged regardless of the circuit of connections of the power part, is developed.* ***Practical value.*** *Using of the combined circuit of single-phase switching on of a three-phase induction motor allows to use a constant capacity in the range of slips from nominal to critical without exceeding the nominal losses.* References 4, tables 1, figures 5.

Key words: **induction motor, single-phase power, thyristor control, harmonics.**

Розроблено узагальнену для різних варіантів з`єднання силової частини електроприводу з тиристорним керуванням математичну модель комбінованої схеми однофазного включення асинхронного двигуна із змінною структурою силової частини та постійною ємністю фазозміщуючого конденсатора. Проведено порівняльний гармонійний аналіз струмів та моментів двигуна та визначено фактори, що впливають на енергоефективність електроприводу, при різних схемах включення силової частини. Бібл. 4, табл. 1, рис. 5.

Ключові слова: **асинхронний двигун, однофазне живлення, тиристорне керування, гармоніка.**

Разработана обобщенная для разных вариантов соединения силовой части электропривода с тиристорным управлением математическая модель комбинированной схемы однофазного включения асинхронного двигателя с переменной структурой силовой части и постоянной емкостью фазосмещающего конденсатора. Проведен сравнительный гармонический анализ токов и моментов двигателя и определены факторы, влияющие на энергоэффективность электропривода, при разных схемах включения силовой части. Библ. 4, табл. 1, рис. 5.

Ключевые слова: **асинхронный двигатель, однофазное питание, тиристорное управление, гармоника.**

Introduction. Circuits of single-phase switching of three-phase induction motors (IMs) with phase-shifting capacitor and permanent structure of the power section are widely used in unregulated electric drives due to the simplicity of design and sufficiently high energy characteristics [1-3]. In the case of a controlled electric drive (ED), the use of circuits with the connection of a phase-shifting capacitor with constant capacity can significantly impair the operational and energy characteristics of the electric drive in start-up and variable speed operation [2, 3]. The use of a capacitor with an adjustable capacity increases the overall dimensions of the ED. In [4], for the operation of controlled pumps at single-phase power, the use of a combined circuit controlled by a thyristor voltage converter (TVC) of the electric drive with variable structure of the power part, shown in Fig. 1 is proposed. The application of this circuit allows the use of a constant capacity in a wide range of speed regulation.

The goal of this work is a comparative analysis of the effect of the harmonic components of the coordinates of a single-phase electric drive arising from the phase control method on the operational characteristics of the electric drive in different variants of the power part connection.

Mathematical model. The circuit of combined connection (Fig. 1) has two variants of connection of a power part. The motor windings in the start mode and at low speed operation are switched on according to the series-parallel switching circuit (position 2 of contactor *K*), in the operating mode – according to the Steinmetz circuit (position 1 of contactor *K*). In order to analyze the processes in this circuit with thyristor control, a generalized mathematical model was developed in which the structure of the differential equations remains unchanged regardless of the circuit of the power unit connections.

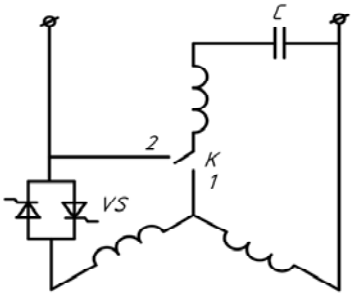

Fig. 1. Single-phase connection combined circuit of the induction electric drive

In the stator coordinate system α, β, 0, electromechanical processes in IM are described by the following system of equations in matrix form:

$$\begin{cases} \bar{u}_S = R_S \cdot \bar{i}_S + \sigma \cdot L_S \cdot p \cdot \bar{i}_S + \dfrac{L_m}{L_r} \cdot p \cdot \bar{\psi}_r; \\ 0 = -R_r \cdot \dfrac{L_m}{L_r} \cdot \bar{i}_S + \dfrac{R_r}{L_r} \cdot \bar{\psi}_r' + p \cdot \bar{\psi}_r' + \bar{\omega} \cdot \bar{\psi}_r'; \\ M = \dfrac{3}{2} \cdot \dfrac{L_m}{L_r} \cdot \left(\psi_\alpha^r \cdot i_\beta^s - \psi_\beta^r \cdot i_\alpha^s \right); \\ J \dfrac{d\omega}{dt} = M - M_c, \end{cases} \quad (1)$$

where $\bar{u}_S = \left| u_\alpha^s, u_\beta^s \right|^t$ is the vector of stator voltages; $\bar{i}_S = \left| i_\alpha^s, i_\beta^s \right|^t$ is the vector of stator currents; $\bar{\psi}_r' = \left| \psi_\alpha^r, \psi_\beta^r \right|^t$ is the vector of rotor flux linkages; $L_S = L_m + L_{\sigma S}$, L_r are the full inductances of stator and rotor; L_m is the inductance of the magnetizing circuit; $L_{\sigma S}$ is the rotor leakage inductance; R_s, R_r are the resistances of stator and rotor; $\sigma = 1 - \dfrac{L_m^2}{L_r \cdot L_S}$ is the leakage coefficient; J is the moment of inertia; $\bar{\omega} = \begin{vmatrix} 0 & \omega \\ -\omega & 0 \end{vmatrix}$ is the matrix that determines the EMF of rotation; p is the symbol of differentiation by time.

To solve the system (1), it is necessary to express the vector of stator voltages $\bar{u}_S = \left| u_\alpha^s, u_\beta^s \right|^t$ through the parameters of the outer circuit of the motor and the state variables for which the stator currents $\bar{i}_S = \left| i_\alpha^s, i_\beta^s \right|^t$ and rotor flux linkages $\bar{\psi}_r' = \left| \psi_\alpha^r, \psi_\beta^r \right|^t$ are taken. Based on the Kirchhoff equation and the known relationships between electromagnetic variables in the orthogonal coordinate system α, β, 0 and in the natural coordinate system A, B, C it is possible to determine that in the general case the stator voltage vector for the studied circuits (Steinmetz and series-parallel) is a function of the network voltage u, the stator current vector $\bar{i}_S$, the rotor flux linkage vector $\bar{\psi}_r$ and the voltage on the capacitor u_C which in turn can be determined by the components of the vector $\bar{i}_S$. Then the general expression for determining the vector of stator voltages will be:

$$\bar{u}_S = \bar{k}_1 \cdot u + \frac{1}{C_1} \cdot \bar{k}_2 \cdot \frac{1}{p} \cdot \bar{i}_S + \left(R_S \cdot \bar{k}_3 + \sigma \cdot L_S \cdot \bar{k}_3 \cdot p \right) \cdot \bar{i}_S + \\ + L_m \cdot \left(\frac{L_m}{L_r} - 1 \right) \cdot \bar{k}_4 \cdot p \cdot \bar{i}_S + \frac{L_m}{L_r} \cdot \bar{k}_5 \cdot p \cdot \bar{\psi}_r'. \quad (2)$$

In the right-hand side of expression (2), the first component is caused by the action of the network voltage, the second one by the voltage on the capacitor, the third one by the action of counter-EMF from zero sequence currents, and the fourth one by the counter-EMF of rotation.

The operation of the thyristor controller is described by a logical function

$$F = X_1 \cdot \Pi + Y_1 + X_2 \cdot \Pi + Y_2, \quad (3)$$

where the logic functions Y_1, Y_2 correspond to the non-zero value of currents through the thyristors, the logic functions X_1, X_2 to the reverse voltages on the thyristors, Π is the switching function corresponding to the control signal of the thyristors.

The switching function Π in phase control has the following form:

$$\Pi = 1 \text{ at } \alpha + \pi \cdot k < \omega_0 \cdot t < (\alpha + \theta) + \pi \cdot k; \\ \Pi = 0 \text{ at } 0 + \pi \cdot k < \omega_0 \cdot t < \alpha + \pi \cdot k \cup \\ \cup (\alpha + \theta) + \pi \cdot k < \omega_0 \cdot t < \pi + \pi \cdot k, \quad (4)$$

where α is the control angle of the thyristors (in electrical degrees); ω_0 is the frequency of supply voltage; θ is the duration of control pulses (in electrical degrees), selected from the conditions of reliable opening of the thyristors; k = 0, 1, 2, 3, ... To reliably open thyristors, the TVC control system must generate pulses of duration of at least 70 electrical degrees.

Thyristor controller's conductive state corresponds to F = 1, non-conductive one to F = 0.

The numerical values of the matrices of coefficients $\bar{k}_1 - \bar{k}_4$ that allow to associate the stator voltage vector of the two-phase IM model in the stator coordinates α, β, 0, with the parameters of the external motor circuit (network voltage, capacitor capacity) and the state variables are given in Table 1 depending on the position of switch K and the state (conductive or non-conductive) of the thyristor controller.

Thus, changing the structure of the power circuit does not require a change in the system of differential equations, and is accompanied only by a change in the coefficients $\bar{k}_1 - \bar{k}_4$ in equation (2), without violating the laws of continuity of motor flux linkages and capacitor charges.

Table 1

Matrices of coefficients of equation (1)

Circuit (position of the key K)	Thyristors state (values of F)	$\bar{k}_1$	$\bar{k}_2$	$\bar{k}_3$	$\bar{k}_4$
1	1	$2/3$ 0	$-1/6 \quad -1/2\sqrt{3}$ $-1/2\sqrt{3} \quad -1/2$	$0 \quad 0$ $0 \quad 0$	$0 \quad 0$ $0 \quad 0$
	0	0 0	$0 \quad 0$ $-1/2\sqrt{3} \quad -1/2$	$0 \quad 0$ $0 \quad 0$	$1 \quad 0$ $0 \quad 0$
2	1	$2/3$ $1/\sqrt{3}$	$-1 \quad 0$ $0 \quad 0$	$-1/3 \quad 0$ $0 \quad 0$	$1/3 \quad 0$ $0 \quad 0$
	0	$2/3$ 0	$-1 \quad 0$ $0 \quad 0$	$-1/3 \quad 0$ $0 \quad 0$	$1/3 \quad 0$ $0 \quad 0$

Results of investigations. Consider first the operation of the ED with a motor 4A71B2 of power of 1.1 kW when connected on the Steinmetz circuit. The curves of changes in time of linear current *i* and of the instantaneous electromagnetic torque *M* when connecting the motor windings according to the Steinmetz circuit are shown in Fig. 2.

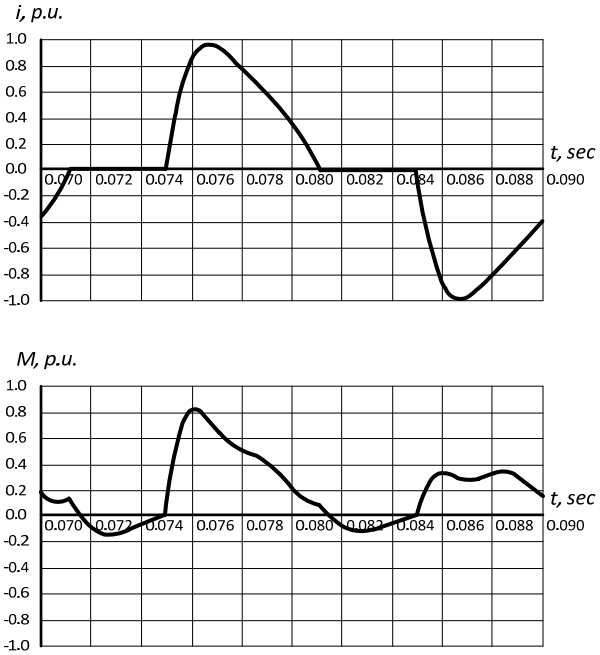

Fig. 2. Current and torque change curves when connected according to the Steinmetz circuit

During the non-conducting state of the thyristors, the phase A current is zero, and the capacitor is periodically discharged through phases B and C. The motor goes into braking at these intervals resulting in the maximum (in modulus) value of the oscillating torques ΔM much greater than the average torque M_{avg} ($\Delta M_{\max}=3...4\cdot M_{avg}$).

The harmonic analysis of the linear current of the motor showed that all odd harmonics are present in the current curve at phase control. The most significant higher harmonic in the curve of the linear current of the motor is the third one whose amplitude reaches at angles α greater than 90 electrical degrees, values of 50…60 % of the amplitude of the fundamental harmonic. The amplitudes of the fifth and seventh harmonics in this case are respectively 30...35 % and 15...20 %.

The dependences of the ratio of power consumed by the motor when powered from TVC with a given opening angle P_{1T} and when powered by sinusoidal voltage equal to the value of the first harmonic at thyristor control, $P_{1\sim}$ per units (p.u.) on the sliding (Fig. 3) show that at when powered from TVC the power consumption is higher than at sinusoidal power supply. The efficiency of the motor when powered from TVC is lower than when at sinusoidal power supply (Fig. 4) while reducing the efficiency is greater, the greater the opening angle of the thyristors, reaching at α = 90...110 electrical degrees 20 %.

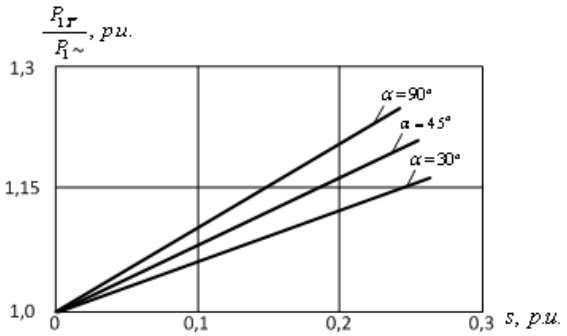

Fig. 3. Dependencies of the ratio of powers consumed by the motor

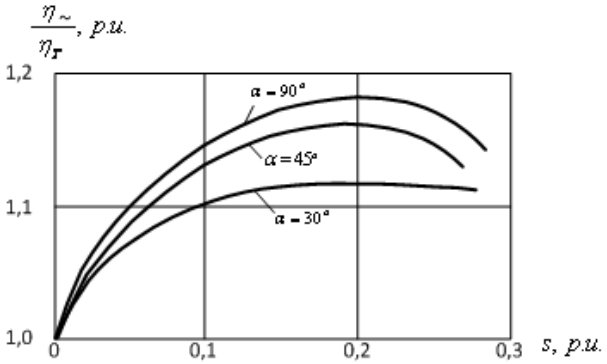

Fig. 4. Dependencies of the motor's efficiency ratio

In order to improve energy performance, it is necessary to use means of reducing the higher harmonic components of the motor current.

One possible way to improve the harmonic composition of the linear current of the motor at thyristor control is to connect the motor in a series-parallel circuit with voltage regulation of only one phase (position 2 of the contactor *K* in Fig. 5). In this case, the unregulated phase winding acts as a filter. The curves of changes in time of linear current *i* and the instantaneous electromagnetic torque *M* of the series-parallel circuit are presented in Fig. 5.

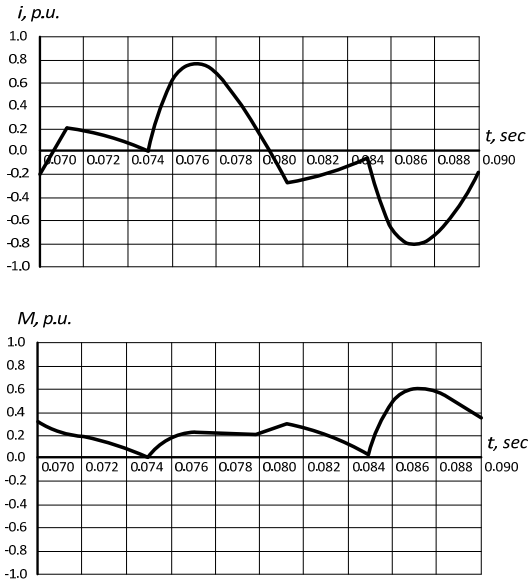

Fig. 5. Current and torque change curves when connected according to the series-parallel circuit

This circuit with the connection of TVC in series with the main phase is characterized by the best harmonic composition of the linear current (the amplitude of the third harmonic is 20-30 % of the amplitude of the first harmonic). The analysis of the simulation results of this circuit showed a significant decrease in the harmonic coefficient (at thyristor opening angles of 90…120 electrical degrees k_v does not exceed 40 %) and a decrease in the amplitude of the third harmonic of the linear current by 30…40 % in the whole range of change of torque and speed.

However, it should be noted that the improvement of the harmonic composition in this circuit is achieved by the price of increasing the asymmetry coefficient and, consequently, the loss from reverse sequence currents. Increasing the coefficient of asymmetry at the phase control of the capacitor IM according to the series-parallel scheme is caused by the delayed nature of the phase shift angle of the first harmonic of the main phase voltage relative to the supply voltage due to the use of thyristors with natural switching.

When comparing Fig. 2, 5 it can be seen that the series-parallel circuit has smaller amplitude of oscillatory torques. The maximum value (in modulus) of the oscillating torques ΔM does not exceed the values 1…1.5 of the average torque M_{avg}. This is due to the fact that in the intervals of the non-conducting state of the thyristors, the motor continues to operate in single-phase connection motor mode and does not go into braking mode, as in the Steinmetz circuit. Figure 5 shows that the non-sinusoidal oscillating component caused by the switching of the thyristors is weakly expressed in the instantaneous electromagnetic torque curve in a series-parallel circuit.

Conclusions.

The use of the combined circuit of single-phase connection on of a three-phase induction motor allows to use a constant capacity in the range of slips from nominal to critical without exceeding the nominal losses.

The analysis of the obtained data shows that the series-parallel circuit has a better harmonic composition of the current consumed and smaller amplitudes of the torque oscillations than the Steinmetz circuit, in practically the whole range of changes of the load torque and speed.

The main influence on the increase of losses in comparison with symmetric sinusoidal amplitude control is due to the asymmetry of the currents in the series-parallel circuit and the higher harmonics of the currents in the Steinmetz circuit.

REFERENCES

1. Popovych O.M., Bibik O.V. Search and evaluation of ways to increase the energy efficiency of a monoblock pump in the application of complex design. *Bulletin of NTU «KhPI». Series: «Electric machines and electromechanical energy conversion»,* 2018, no.5(1281), pp. 79-82. (Ukr).

2. Malyar V., Hamola O., Maday V. Calculation of capacitors for starting up a three-phase asynchronous motor fed by single-phase power supply. *17th International Conference Computational Problems of Electrical Engineering (CPEE)*, Sep. 2016. **doi: 10.1109/cpee.2016.7738735**.

3. Bespalov V.Ya., Moshchinskiy Yu.A., Petrov A.P. Dynamic parameters of three-phase asynchronous motor with single-phase power supply. *Russian Electrical Engineering*, 2000, no.1, pp. 13-19. (Rus).

4. Shurub Yu.V, Vasilenkov V.Ye., Tsitsyurskiy Yu.L. Investigation of properties of combined scheme of single-phase switching of induction electric drive of pumping plants. *Technical Electrodynamics*, 2018, no.6, pp. 50-53. (Ukr). **doi: 10.15407/techned2018.06.050.**

Received 23.10.2019

Yu.V. Shurub[1]*, Candidate of Technical Science,*
Yu.L. Tsitsyurskiy[2]*,*
[1] The Institute of Electrodynamics of the NAS of Ukraine,
56, prospekt Peremogy, Kiev, 03057, Ukraine,
e-mail: shurub@bigmir.net
[2] National University of Life and Environmental Sciences of Ukraine,
15, Heroiv Oborony Str., Kyiv, 03041, Ukraine.

How to cite this article:
Shurub Yu.V., Tsitsyurskiy Yu.L. Harmonic analysis of the combined circuit of single-phase switching of induction electric drive with thyristor control. *Electrical engineering & electromechanics,* 2020, no.1, pp. 25-28. **doi: 10.20998/2074-272X.2020.1.04.**

UDC 621.3.013.22:517.968 **doi: 10.20998/2074-272X.2020.1.05**

S.T. Tolmachev, S.L. Bondarevskyi, A.V. Il'chenko

MAGNETIC PROPERTIES OF MULTICOMPONENT HETEROGENEOUS MEDIA WITH A DOUBLY PERIODIC STRUCTURE

Heterogeneous media have a wide range of practical applications. Media with a doubly periodic structure (matrices of high-gradient magnetic separators, etc.) occupy an important place. Their study is usually based on experimental and approximate methods and is limited to simple two-phase systems. The development of universal and accurate methods of mathematical modelling of electrophysical processes in such environments is an urgent task. The aim of the paper is to develop a method for calculating local and effective parameters of a magnetostatic field with minimal restrictions on the number of phases, their geometry, concentration, and magnetic properties. Based on the theory of elliptic functions and secondary sources, an integral equation is formulated with respect to the magnetization vector of the elements of the main parallelogram of the periods. The calculated expressions for the complex potential, field strength, and components of the effective magnetic permeability tensor are obtained. The results of a series of computational experiments confirming the universality and effectiveness of the method are presented. As an example of a practical application, a detailed study of the field of the magnetic forces of the matrix is carried out: the lines of magnetic isodine and potential extraction areas for a complex version of the matrix are constructed. Within the framework of the developed method, the calculation of local and effective field characteristics is carried out by solving the field problem in the field of an arbitrary parallelogram of periods without specifying boundary conditions on its sides with a comprehensive consideration of significant interdependent factors. The practical value of the method is to create new opportunities for improving the technical characteristics of electrophysical devices for which the universality and accuracy of calculating local and effective field characteristics is decisive. An algorithm for optimizing the characteristics of the separator is proposed. References 16, figures 11.

Key words: **doubly periodic heterogeneous medium, integral equation, magnetization vector, strength field, homogenization problem, magnetic permeability tensor, polygradient separation, matrix, magnetic forces.**

Викладено метод розрахунку магнітостатичного поля в двоякоперіодичному гетерогенному середовищі. Сформульовано інтегральне рівняння відносно вектора намагніченості елементів середовища. Розрахунок характеристик поля виконується шляхом вирішення польової задачі в області основного паралелограма періодів без задання граничних умов на його сторонах. Отримано розрахункові вирази для напруженості поля і тензора магнітної проникності. Наведено результати обчислювальних експериментів, що підтверджують універсальність і ефективність методу. Проведено детальне дослідження поля магнітних сил матриці високоградієнтного магнітного сепаратора. Метод відкриває нові можливості підвищення технічних характеристик електрофізичних пристроїв, для яких універсальність і точність розрахунку локальних і ефективних характеристик поля є визначальною. Бібл. 16, рис. 11.

Ключові слова: **двоякоперіодичне гетерогенне середовище, інтегральне рівняння, вектор намагніченості, поле напруженості, тензор магнітної проникності, високоградієнтна сепарація, матриця, магнітні сили.**

Изложен метод расчета магнитостатического поля в двоякопериодической гетерогенной среде. Сформулировано интегральное уравнение относительно вектора намагниченности элементов среды. Расчет характеристик поля осуществляется путем решения полевой задачи в области основного параллелограмма периодов без задания граничных условий на его сторонах. Получены расчетные выражения для напряженности поля и тензора магнитной проницаемости. Приведены результаты вычислительных экспериментов, подтверждающих универсальность и эффективность метода. Проведено детальное исследование поля магнитных сил матрицы высокоградиентного магнитного сепаратора. Метод открывает новые возможности повышения технических характеристик электрофизических устройств, для которых универсальность и точность расчета локальных и эффективных характеристик поля является определяющей. Библ. 16, рис. 11.

Ключевые слова: **двоякопериодическая гетерогенная среда, интегральное уравнение, вектор намагниченности, поле напряженности, тензор магнитной проницаемости, высокоградиентная сепарация, матрица, магнитные силы.**

Introduction. Heterogeneous media (HM) are widely used due to a wide range of their practical application: magnetodielectrics, semiconductors, mixtures, solutions, composite and reinforced materials, electrostatic and magnetic filters, etc.

The theory of HM originates from the classical works by J. Maxwell and J. Rayleigh, which dealt with determining the effective parameters of the HM with canonical inclusions in the shape of cylinders and spheres (the problem of homogenization). Subsequently, these investigations were developed and summarized by many authors: K.M. Polivanov, V.M. Finkelberg, A.V. Netushil, B.M. Fradkin, V.I. Odelevsky, L.D. Stepin, B.Ya. Balagurov, Yu.P. Yemets, V. Buryachenko, M. Kharadly, W. Jackson, K.Z. Markov, S. Nemat-Nasser, M. Hori, W.T. Perrins, D.R. McKenzie, R.C. McFedran, P.D. Qyuivy, S. Torcuato and many others.

Various aspects of the theory and practice of HM were actively developed in Ukraine, in particular, by researchers of the Institute of Electrodynamics of the NAS of Ukraine. Particular attention was paid to the development of methods for analyzing electromagnetic fields in electrically conductive, dielectric, composite and heterogeneous systems at the Department of Electrophysics of Energy Conversion. Yu.P. Yemets developed analytical methods for analyzing electric fields using methods of integral equations and complex variables. 2D two-component systems with a regular distribution structure of inhomogeneities are considered.

The main effective parameters of two-component dielectric and conductive media with canonical inclusions are determined: conductance, magnetoresistance and Hall coefficient. Research results by Yu.P. Emets and his followers in this direction are presented in the monograph [1].

Based on the multipole expansion of high orders, the classical J. Maxwell and J. Rayleigh formulas on spherical and circular cylinders in a rectangular matrix in [2] are generalized and developed for the case of elliptic cylinders and spheroidal elements. There, for the first time, a fairly general field formulation was considered on the doubly periodic problem of magnetostatics for a nonlinear inhomogeneous anisotropic medium with periodic inclusions and with complex geometry of elements.

In recent years, the scope of HM has been steadily expanding: the study of nanocomposite materials [3], ferromagnetic perforated membranes (magnetic sieves) [6], and other devices for micromagnetic separation of ultrafine magnetic particles [5]. More actively in the study of the properties of the HM the capabilities of modern information technology are used.

Significant place in the theory and applications of HM occupy the tasks associated with the use of a magnetic field. In particular, one of such problems is the synthesis of filter matrices of high-gradient magnetic separators (HGMS) for maximum extraction of weakly magnetic minerals. The need for these devices arose in the middle of the last century due to the depletion of reserves of rich raw materials against the background of the rapidly developing technology of homeless metallurgy and the growth of requirements for the quality of steel [6, 7]. Various types of HGMS (Jones, Sala-Carousel, Boxmag Rapid, Krupp-Sol-24/14, 6-ERM-35/135, VGS-100/2, etc.) were created. The operation of these separators showed that at high weight and size parameters (for example, the Jones separator DR 335 with capacity of 180 t/h has a rotor diameter of 3.35 m and mass of 114 t) and specific power consumption they do not always provide the required technological parameters of enrichment. Therefore, the development of new HGMS designs continues, and the optimization of their technical parameters remains an urgent task.

A distinctive feature of the HGMS, which largely determines their effectiveness, is the use of magnetic filters of the matrix structure, the elements of which have complex geometry and high concentration to increase the magnetic field strength and its gradient. The study of various types of matrices is the subject of attention of many authors. A review of the current state of this issue with an extensive bibliography is given in [5]. The interest in this issue is explained by the fact that the matrix significantly affects productivity, separation efficiency, and operating cost. Ideally, it should, with high extraction efficiency, provide the maximum specific capture volume of the useful mineral with the minimum possible pulp resistance.

Optimization of matrix parameters is associated with a compromise between a large number of factors affecting its effectiveness. The magnetic force acting on a particle with volumetric magnetic susceptibility χ and volume V, $\boldsymbol{F}=\mu_0\chi V|\boldsymbol{H}|\text{grad}(|\boldsymbol{H}|)$. In this expression, the last two factors are related to the magnetic system of the separator and its matrix, and the rest are related to the extracted magnetic material. If justification of the holding force $|\boldsymbol{F}|_{\min}$ for specific parameters χ and V is the task of technologists, then ensuring the necessary value of the value of $\boldsymbol{F}^*=|\boldsymbol{H}|\text{grad}(|\boldsymbol{H}|)$, at which $|\boldsymbol{F}| \geq |\boldsymbol{F}|_{\min}$, is a rather complicated task requiring special research. Obviously, the $\boldsymbol{F}^*$ value is important for extraction, not the $|\boldsymbol{H}|$ and $\text{grad}(|\boldsymbol{H}|)$ values separately. Moreover, the «weight» of each of the factors is far from obvious. The increase in the field strength $\boldsymbol{H}$ is associated with an increase in the power and, ultimately, the mass and size parameters of the separator. Since here the magnetic field gradient does not change significantly, an increase in the magnetic field strength «blindly» does not necessarily lead to an improvement in the separation efficiency in practical use [7]. As for the field gradient, the possibility of increasing it is potentially much greater, since it substantially depends on the size of the matrix elements and their shape. But here, a compromise solution should be sought, since for selective separation it is necessary to coordinate the dimensions of the matrix element with the particle size distribution. In addition, the large heterogeneity of the matrix field and especially of its gradient greatly complicates the task of ensuring the maximum capture zone while eliminating the possible blocking of the matrix. This explains a large number of studies on precisely the geometric parameters of matrix elements. For example, in [8], the expected decrease in the magnetic force with an increase in the number of sides of regular polygons has been confirmed by calculation. The studies of many authors (see, for example, [7, 9, 10]) recommended the optimal parameters of triangular gear plates, although due to a more uniform force field, replacing triangular elements with elements with a lower surface steepness can increase the ability to collect small particles. On the contrary, the patent [11] proposed strengthening the forces for the extraction of a fine fraction by replacing rods of circular cross section with rods with a diamond-shaped cross section (with a reduction in the size of the capture zone). The publication [12] recommended as promising rod matrices with an elliptical cross section. A number of works (see, for example, [13]) discuss the feasibility of using a combination of rods with different diameters or different cross-sectional shapes, as well as changing the order of their grouping.

A feature of the listed works is their particular and sometimes contradictory nature, as well as the predominant orientation to simple forms of matrix elements. Unfortunately, they do not give an idea of the local distribution of the field of magnetic forces in the working space of the matrix formed by elements of complex geometry and arbitrary concentration, especially when there are difficulties with the formation of boundary conditions in order to localize the calculation domain.

The wide variety of matrix elements used (balls, corrugated plates, rods, nets, spirals, wire wool, etc.) significantly complicate the development of a universal mathematical model for calculating the force field of

HGMS matrices. At the same time, the most common type of rod matrices, which are characterized by periodicity along the plane coordinates, should be selected. As shown in [2, 14], to study such media, the natural mathematical apparatus is the theory of doubly periodic (elliptic) functions, the use of which allows one to efficiently solve doubly periodic problems for HM in a fairly general formulation.

The goal of the paper is the development of a universal method for calculating the magnetic and force fields of a heterogeneous medium with a doubly periodic structure without significant restrictions on the number of phases, their geometry, concentration, and magnetic properties.

Basic definitions and properties of doubly periodic systems. The first and indispensable condition for the investigation of multicomponent HM is the determination of the main periods ω_1 and ω_2, which are the constituents of the main parallelogram of the periods Ω (if it exists). The unequivocal answer to this question is not always obvious, since, as will be shown below, even the doubly periodicity of all phases of a multicomponent HM does not guarantee its doubly periodicity as a whole.

Consider a pair of complex numbers ω_1 and ω_2, with $\mathrm{Im}(\tau=\omega_2/\omega_1)>0$. Points u and v of the complex plane are called congruent if they are connected by the relation $u \equiv v \bmod(\omega_1, \omega_2)$ [15] or

$$u = v + m_1 \cdot \omega_1 + m_2 \cdot \omega_2, \text{ at } m_1, m_2 = 0, \pm 1, \pm 2, \ldots . \quad (1)$$

A parallelogram with vertices u_0, $u_0+\omega_1$, $u_0+\omega_2$, $u_0+\omega_1+\omega_2$ will be called a parallelogram of periods constructed on periods ω_1 and ω_2. Obviously, the set of congruent points corresponds to an infinite number of parallelograms of periods covering the entire complex plane without overlapping.

The concept of a doubly periodic (elliptic) function occupies an important place in the subsequent analysis. Denote $\boldsymbol{\omega}=m_1 \cdot \omega_1 + m_2 \cdot \omega_2$. The function $f(u)$ with periods $\boldsymbol{\omega}$ will be called doubly periodic, and ω_1 and ω_2 – its main periods.

From the theory of elliptic functions, it is known [13] that a pair of main periods (ω_1, ω_2) is not unique. If for arbitrary integers m_1, m_2 and m_1', m_2' the sets of points $\boldsymbol{\omega}=m_1 \cdot \omega_1 + m_2 \cdot \omega_2$ and $\boldsymbol{\omega}'=m_1' \cdot \omega_1' + m_2' \cdot \omega_2'$ coincide, then the pairs of periods $\boldsymbol{\omega}$ and $\boldsymbol{\omega}'$ are equivalent. Here, a pair of periods (ω_1, ω_2) is equivalent if and only if to a pair of periods (ω_1', ω_2'), when the relation $\omega_2' = \alpha \cdot \omega_2 + \beta \cdot \omega_1$, $\omega_1' = \gamma \cdot \omega_2 + \delta \cdot \omega_1$ is valid, where $\alpha, \beta, \gamma, \delta$ are the integers that satisfy the condition $\alpha \cdot \delta - \beta \cdot \gamma = 1$ at $\mathrm{Im}(\omega_2/\omega_1)>0$. Examples of equivalent periods for two sets of congruent points are shown in Fig. 1.

We note some more obvious statements. The areas of equivalent periods are the same, and the area of the main parallelogram Ω with periods (ω_1, ω_2) is minimal. We will also call two parallelograms with periods (ω_1, ω_2) and (ω_1', ω_2') similar if the directions of the periods ω_1 and ω_1', ω_2 and ω_2' and coincide.

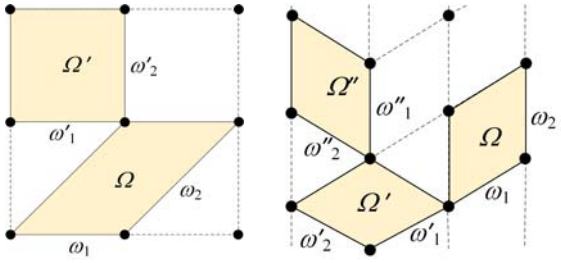

a *b*

Fig. 1. Sets of congruent points and their corresponding equivalent parallelograms of periods

The concept of a doubly periodic HM is more complicated than the concept of a doubly periodic lattice, since in addition to geometrical properties it is also necessary to take into account the physical and other properties of individual phases, their arrangement in the parallelogram of periods, etc. Moreover, the set of HM can correspond to the same period lattice. For example, we establish a correspondence between doubly periodic HM shown in Fig. 2 and lattices of periods of Fig. 1.

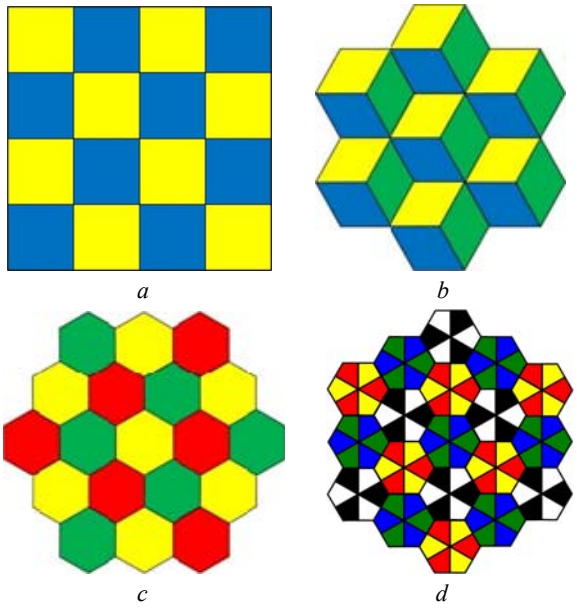

a *b* *c* *d*

Fig. 2. Examples of doubly periodic multicomponent HM corresponding to the lattices of Fig. 1: two-component – *a*; three-component – *b* and *c*; six-component – *d*

Note an important point on the example of Fig. 2,*a*. The main parallelogram for the set of congruent points is the small square. At the same time, it cannot be the main parallelogram of the HM, since, for example, the entire complex plane cannot be covered by the yellow phase. Therefore, for this HM, the main parallelograms of the periods correspond to Fig. 1,*a* (each of them includes two elements of the yellow and blue phases). HMs, shown in Fig. 2,*b*,*c*,*d* correspond to Fig. 1,*b*. Indeed, considering in Fig. 2,*b*,*c* the system of congruent points of the yellow phase (for example, the upper points of the elements) we see that they coincide with the period lattice of Fig. 1,*b*. The same can be said about other congruent points of the yellow and two other phases. More complicated HM of Fig 2,*d* also corresponds to Fig. 1,*b*. After turning Fig. 2,*d*

(or coordinate systems) at 30° it can be seen that topologically Fig. 2,*c*,*d* are the same. The only difference is that each element of the phases of Fig. 1,*c* corresponds to three elements of the two phases of Fig. 2,*d*. Here, as it is easy to see, the sets of the corresponding congruent points of all six phases coincide with the lattice of periods in Fig. 1,*b*.

Shown in Fig. 2 multicomponent HMs have obvious doubly periodicity with the same lattice parameters for the periods of each phase within the HM. As will be shown below, in this case, the main periods of the HM generally coincide with the corresponding periods of the phases.

A number of important conclusions can be drawn from the analysis performed. In particular, it is legitimate to introduce the concept of congruent areas, whose geometry is fully reproduced in each parallelogram of periods. Moreover, these areas can be multiply connected and multicomponent. This follows from the statement that each period parallelogram of system (1) owns only one point of this system [15]. Considering the set of arbitrary points ν with the sets of congruent points (1) generating them, we naturally come to the concept of congruent doubly periodic domains.

We will illustrate some additional features of a doubly periodic HM using the example of a complex HM shown in Fig. 3.

The discrete phase of this HM is represented by three fractions – red, blue and green. The main parallelograms of the periods of these fractions are highlighted in the corresponding colors. They are similar (i.e., the corresponding sides of the parallelograms are parallel), but have different basic periods and concentration of inclusions. For example, if for the green fraction introduce the designation $\Omega^1=(\omega_1, \omega_2)$, then for the red fraction $\Omega^2=(\omega_1, 2\cdot\omega_2)$, and for the blue one $\Omega^3=(3\cdot\omega_1, \omega_2)$. Note that each of the highlighted main parallelograms of periods Ω^i has a set of equivalent ones, however, for the HM under consideration, all of them are reduced to similar ones. This procedure is necessary to answer the important question: is this HM a doubly periodic, and if so, what are the main periods of this medium. This question was posed in [16]. therefore, we confine ourselves here to some refinements and additions.

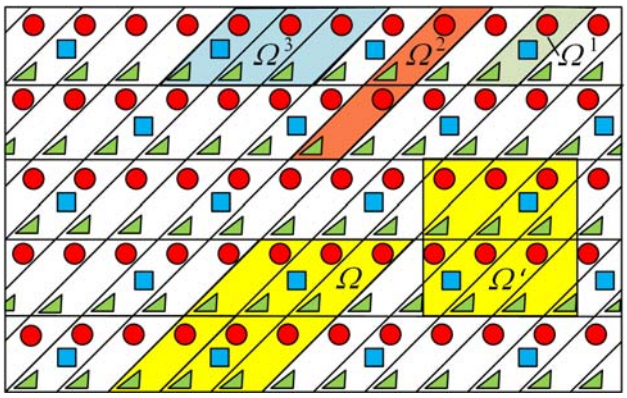

Fig. 3. Basic parallelograms of periods Ω^1, Ω^2, Ω^3 of separate phases and equivalent parallelograms of periods Ω and Ω' of a three-component HM

The condition of doubly periodicity of a multicomponent HM. Let some multicomponent HM is composed of a number of doubly periodic HMs of a lower level. Denote by $\{\Omega^i\}$ the set of primitive lattices $\boldsymbol{\omega}^i=(\omega_1^i, \omega_2^i)$, i=1, 2, 3, … P. In the simplest case, when $\omega_1^i = n^i\cdot\tilde{\omega}_1$, $\omega_2^i = m^i\cdot\tilde{\omega}_2$, where $\tilde{\omega}_1$ and $\tilde{\omega}_2$ are some complex numbers, $\mathrm{Im}(\tilde{\omega}_2/\tilde{\omega}_1)>0$, and n^i, m^i are the arbitrary natural numbers , the HM under consideration is doubly periodic and its main periods ω_1, ω_2 are defined as follows. Denote by N and M the least common multiples for the sets $\{n^i\}$, $\{m^i\}$: N = lcm(n^1, n^2, …, n^P), M = lcm(m^1, m^2, …, m^P). Then $\omega_1=N\cdot\tilde{\omega}_1$, $\omega_2=M\cdot\tilde{\omega}_2$. For example, for the HM considered in Fig. 3, N = lcm(1, 1, 3) = 3, M = lcm(1, 2, 1) = 2. Thus, $\omega_1=3\cdot\tilde{\omega}_1$, $\omega_2=2\cdot\tilde{\omega}_2$. In Fig. 3 two equivalent periods of HM Ω and Ω' are highlighted in yellow.

Note several important consequences of the analysis carried out.

1. A necessary condition for doubly periodicity of the HM is the existence in the set of main periods of the phases $\{\Omega^i\}$ of a subset of similar periods $\{\Omega'^i\}$.

2. The doubly periodicity and similarity of periods $\{\Omega'^i\}$ does not guarantee the doubly periodicity of the HM as a whole. For example, let $\omega_1^1 = a$, $\omega_1^2 = b$, $\omega_2^1 = \omega_2^2$, and $a \neq b$ are any irrational numbers, for example, $a = e$, $b = \pi$. Obviously, it is impossible to select integer multiplicities for the specified periods.

3. At a linear displacement of the main parallelogram of periods Ω or when moving to the equivalent parallelogram, all congruent components (or their parts), the concentration of individual phases and physical parameters that are doubly periodic, such as the magnetization vectors in the corresponding congruent points, are conserved. This is important in the practical solution of problems on the definition of local and effective parameters of HM.

It should be noted that the establishment of the fact that the HM is doubly periodic and the determination of its main periods significantly expand the possibilities of investigation the HM, since it provides the possibility of applying the theory of elliptic functions and limits the scope of analysis by the main parallelogram of periods.

Basic calculation relations. In the complex plane E, we consider a medium with a regular structure formed by a set of congruent groups of magnetics, each of which corresponds to a bounded (in the general case multiply connected) domain $D_{mn}\equiv\cup D_{mn}^j$ with a sufficiently smooth boundary $S_{mn}\equiv\cup S_{mn}^j$ (j = 1, 2, ... , k; m, n = 0, ±1, ±2, ...). For convenience, we denote the domain D_{00} corresponding to the main parallelogram Ω with periods ω_1 and ω_2, by D. Accordingly, $S_{00}\equiv S$ and $\bar{D}\equiv D\cup S$. The region external to the magnetics is denoted by $D_e\equiv E\backslash D_{mn}$.

Let $B^j=B^j(H, z)$ be a known function that, in the general case, defines the inhomogeneous, nonlinear and

anisotropic properties of the set of congruent elements $j, z \in D_{mn}$. If $z \in D_e$, then $B=\mu_0 H$.

Consider a system of dipoles with identical moments M located at the points $\xi \equiv \xi \bmod(\omega_1, \omega_2)$. Their complex potential and field strength [2]

$$W_M(z) = \frac{M}{2\pi} \cdot \zeta(z-\xi) + C(z-\xi), \tag{2}$$

$$H_M(z) = -\overline{W}'_M(z) = -\frac{\overline{M}}{2\pi} \cdot \overline{\zeta'(z-\xi)} - \overline{C} = \frac{\overline{M}}{2\pi} \cdot \overline{\wp(z-\xi)} - \overline{C}, \tag{3}$$

where $\zeta(z-\xi) = \zeta(u)$, $\wp(z-\xi) = \wp(u)$ are the Weierstrass functions, and a bar over a complex number means a conjugation operation.

Without loss of generality, we combine the period ω_1 with the x axis and take $\mathrm{Im}\,\omega_1=0$. Taking into account the Legendre relation [13]

$$\eta_1 \cdot \omega_2 - \eta_2 \cdot \omega_1 = 2\pi \mathrm{j},$$

for the constant C we obtain the expression [2]

$$C = -\frac{1}{2\pi} \cdot \left(M_1 \frac{\eta_1}{\omega_1} + M_2 \frac{\eta_2}{\omega_2} \right) = \frac{\mathrm{j} \cdot M_2}{\omega_1 \cdot \omega_2} - \frac{M}{2\pi} \cdot \frac{\eta_1}{\omega_1} = \frac{\mathrm{j} \cdot \mathrm{Im}\, M}{F_\Omega} - \frac{M}{2\pi} \cdot \frac{\eta_1}{\omega_1}, \tag{4}$$

where M_1, M_2 is the decomposition of the vector M in the directions of the periods ω_1 and ω_2, $F_\Omega = \omega_1 \cdot \mathrm{Im}\,\omega_2$ is the area of the main parallelogram of periods Ω.

Let $J(z)$, $z \in D$ be the distribution of magnetization arising under the action of the field of primary sources $H_0(z)$. A joint consideration in the domain D of the action of primary and secondary sources (the magnetization of all magnetics in E) leads to expressions for the complex potential and intensity [12]:

$$W(z) = W_0(z) + W_J(z) = W_0(z) + \frac{1}{2\pi} \cdot \int_\Omega J(\xi) \cdot [\zeta(z-\xi) - \frac{\eta_1}{\omega_1} \cdot (z-\xi)] \cdot \mathrm{d}\tau_\xi + \frac{\mathrm{j}}{F_\Omega} \cdot \int_\Omega \mathrm{Im}\, J(\xi) \cdot (z-\xi) \cdot \mathrm{d}\tau_\xi, \tag{5}$$

$$H(z) = H_0(z) + H_J(z) = H_0(z) + \frac{1}{2\pi} \times \int_\Omega \overline{J}(\xi) \cdot \left[\overline{\wp(z-\xi) + \frac{\eta_1}{\omega_1}} \right] \mathrm{d}\tau_\xi + \frac{\mathrm{j} \cdot \mathrm{Im}\, P}{F_\Omega}, \tag{6}$$

where P is the full dipole moment of the main parallelogram Ω. The integral in (6) is singular.

Let us consider in more detail the linear case: $B^j = \mu_a^j \cdot H = \mu_0\, \mu^j \cdot H$, $B_e = \mu_0 \cdot H$ for $z \in D$ and $z \in D_e$, respectively. In this case, outside the domain D $J(z)=0$ and the problem of calculation of the field characteristics at an arbitrary point of the HM is reduced to calculation of the distribution of the magnetization vector $J(z)$ in D.

Introduce the integral operator that is important for the analysis below [2]

$$\Pi_\omega J = -\frac{1}{\pi} \int_D J(\xi) \cdot \left[\wp(z-\xi) + \frac{\eta_1}{\omega_1} \right] \mathrm{d}\tau_\xi + \frac{2\mathrm{j} \cdot \mathrm{Im}\, P}{F_\Omega}. \tag{7}$$

Denote $\tilde{B} = \mu_0^{-1} B$ and consider a chain of equalities:

$$J = \tilde{B} - H = (\mu - 1) \cdot H; \tilde{B}_J + H_J = \overline{\Pi_\omega J}; \quad \tilde{B} + H = (\mu + 1) H = 2H_0 + \tilde{B}_J + H_J = 2H_0 - \overline{\Pi_\omega J}. \tag{8}$$

From (7), (8) it is easy to obtain an integral equation for the medium magnetization vector $J(z)$, $z \in D$:

$$J(z) = \lambda \cdot (2H_0(z) - \overline{\Pi_\omega J}) = \lambda \left\{ 2H_0(z) + \frac{1}{\pi} \int_D \overline{J(\xi)} \cdot \left[\overline{\wp(z-\xi) + \frac{\eta_1}{\omega_1}} \right] \mathrm{d}\tau_\xi + \frac{2\mathrm{j} \cdot \mathrm{Im}\, P}{F_\Omega} \right\}, \tag{9}$$

where $\lambda = (\mu - 1)/(\mu + 1)$.

We give one more expression for the singular operator $\Pi_\omega J$. Denoting by σ_ε a circle of small radius ε, and by $D_\varepsilon = D \setminus \sigma_\varepsilon$ a domain D with punctured point $z = \xi$, expression (7) is transformed to

$$\Pi_\omega J = -\frac{1}{\pi} \int_{D_\varepsilon} J(\xi) \cdot \partial_\xi \left[\zeta(z-\xi) - \frac{\eta_1}{\omega_1}(z-\xi) \right] \mathrm{d}\tau_\xi + \frac{2\mathrm{j} \cdot \mathrm{Im}\, P}{F_\Omega} = -\frac{1}{\pi} \int_{D_\varepsilon} \partial_\xi \left\{ J(\xi) \cdot \left[\zeta(z-\xi) - \frac{\eta_1}{\omega_1}(z-\xi) \right] \right\} \mathrm{d}\tau_\xi - \frac{1}{\pi} \cdot \int_{D_\varepsilon} \partial_\xi J \left[\zeta(z-\xi) - \frac{\eta_1}{\omega_1}(z-\xi) \right] \mathrm{d}\tau_\xi + \frac{2\mathrm{j} \cdot \mathrm{Im}\, P}{F_\Omega}. \tag{10}$$

It is easy to establish that

$$P = \int_D J(\xi) \cdot \mathrm{d}\tau_\xi = \int_D \{ \partial_\xi [\xi \cdot J(\xi)] - \xi \cdot \partial_\xi J \} \cdot \mathrm{d}\tau_\xi. \tag{11}$$

Applying the Green formula to (10), (11), assuming the differentiability of the function f

$$\int_{D_\varepsilon} \partial_\xi f \cdot \mathrm{d}\tau_\xi = -\frac{1}{2\mathrm{j}} \cdot \int_S f(\xi) \cdot d\overline{\xi} + \frac{1}{2\mathrm{j}} \cdot \int_{|z-\xi|=\varepsilon} f(\xi) \cdot \mathrm{d}\overline{\xi} \tag{12}$$

and taking into account that the integral (12) along a circle of a sufficiently small radius ε is zero, we find:

$$P = \int_D J(\xi) \cdot \mathrm{d}\tau_\xi = \int_D \{ \partial_\xi [\xi \cdot J(\xi)] - \xi \cdot \partial_\xi J \} \cdot \mathrm{d}\tau_\xi = -\frac{1}{2\mathrm{j}} \cdot \int_S \xi \cdot J(\xi) \cdot \mathrm{d}\overline{\xi} - \int_D \xi \cdot \partial_\xi J \cdot \mathrm{d}\tau_\xi.$$

Here S is the boundary of the domain D (in the general case, multiply connected). At $\lambda(z) = \mathrm{const}$ $\partial_\xi J = 0$, therefore, the singular operator $\Pi_\omega J$ is expressed through the surface (boundary) integral

$$\Pi_\omega J = \frac{1}{2\pi\mathrm{j}} \cdot \int_S J(\xi) \cdot \left[\zeta(z-\xi) - \frac{\eta_1}{\omega_1}(z-\xi) \right] \cdot \mathrm{d}\overline{\xi} - \frac{1}{F_\Omega} \cdot \mathrm{Re} \left[\int_S \xi \cdot J(\xi) \cdot \mathrm{d}\overline{\xi} \right]. \tag{13}$$

The practical implementation of the basic relations. Let us now consider some questions of the practical use of the expressions obtained. We represent the domain D as a set of triangular elements $D \equiv \cup D^k$ with a constant magnetization J^k corresponding to the center of gravity ξ^k of triangle D^k. In this case, the solution $J(z) \equiv \cup J^k(z)$ can be obtained by simple iteration method for the equation

$$J_i^m \equiv J_i(z^m) = 2\lambda \cdot H_0^m + \frac{\lambda}{\pi} \cdot \sum_k \int_{D^k} \overline{J_{i-1}(\xi^k)} \times \left[\overline{\wp(z^m - \xi) + \frac{\eta_1}{\omega_1}} \right] \cdot \mathrm{d}\tau_k + \frac{2\mathrm{j} \cdot \lambda}{F_\Omega} \cdot \mathrm{Im} \sum_k \int_{D^k} \overline{J_{i-1}(\xi^k)} \cdot \mathrm{d}\tau_k. \tag{14}$$

($m = 1, 2, 3, \ldots, M$; $i = 1, 2, 3, \ldots$).

If we consider the magnetized domains D^k as dipoles with magnetic moments $M^k = J^k \cdot \Delta\tau_k$, located at the points ξ^k, then (14) is greatly simplified:

$$J_i^m = 2\lambda \cdot H_0^m + \frac{\lambda}{\pi} \cdot \sum_k \int_{D^k} \overline{A_m^k \cdot J_{i-1}^k} \cdot \Delta\tau_k + \\ + \frac{2\mathrm{j} \cdot \lambda}{F_\Omega} \cdot \mathrm{Im} \sum_k \int_{D^k} \overline{J_{i-1}^k} \cdot \Delta\tau_k , \quad (15)$$

where $A_{mk} = \wp(z^m - \xi^k) + \eta_1/\omega_1$.

The calculation of A_{mk} values can be performed using the formulae [15]

$$\wp(u) + \frac{\eta_1}{\omega_1} = -\frac{4\pi^2}{\omega_1^2} \cdot \left\{ \frac{1}{(h - h^{-1})^2} + \sum_{r=1}^{\infty} \left[\frac{q^{2r} \cdot h^{-2}}{(1 - q^{2r} \cdot h^{-2})^2} + \right. \right. \\ \left. \left. + \frac{q^{2r} \cdot h^2}{(1 - q^{2r} \cdot h^2)^2} \right] \right\}, \quad (16)$$

or at $-\mathrm{Im}\,\tau < \mathrm{Im}\ \nu < \mathrm{Im}\,\tau$

$$\wp(u) + \frac{\eta_1}{\omega_1} = \frac{\pi^2}{\omega_1^2 \cdot \sin^2(\pi\nu)} - \frac{8\pi^2}{\omega_1^2} \cdot \sum_{n=1}^{\infty} \frac{n q^{2n}}{1 - q^{2n}} \cos(2\pi \cdot n\nu), \quad (17)$$

where $u \equiv u^{mk} = z^m - \xi^k$, $q = \exp(\mathrm{j}\pi\tau)$, $\nu = u/\omega_1$.

For uniformly magnetized triangles, the integrals in (14) can be calculated analytically. Applying (13) for the k-th triangle and taking into account that [15]

$$\zeta(u) - \frac{\eta_1}{\omega_1} u = \frac{d}{du} \ln \vartheta_1(\nu, \tau) = -\frac{d}{d\xi} \ln \vartheta_1(\nu, \tau), \quad (18)$$

we obtain

$$\Pi_\omega J = \sum_k \frac{J^k}{2\pi\mathrm{j}} \cdot \int_{S^k} \partial_\xi [\ln \vartheta_1(z^m - \xi)] \cdot \mathrm{d}\bar{\xi} - \\ - \frac{1}{F_\Omega} \sum_k \mathrm{Re} \left[J^k \cdot \int_{S^k} \xi \cdot \mathrm{d}\bar{\xi} \right] = \\ = \sum_k \frac{J^k}{2\pi\mathrm{j}} \left[\begin{array}{l} a_{ijk} \ln \vartheta_1(z^m - z^j) + a_{kij} \ln \vartheta_1(z^m - z^i) + \\ + a_{jki} \ln \vartheta_1(z^m - z^k) \end{array} \right] - \\ - \frac{1}{F_\Omega} \sum_k \mathrm{Re} \left[J^k \cdot \int_{S^k} \xi \cdot \mathrm{d}\bar{\xi} \right]. \quad (19)$$

In this expression S^k is the boundary of the k-th triangle, z^i, z^j, z^k are the complex coordinates of its vertices, $a_{kij} = a_{ki} - a_{ij}$, $a_{ijk} = a_{ij} - a_{jk}$, $a_{jki} = a_{jk} - a_{ki}$, $a_{mn} = (\overline{z^n - z^m})/(z^n - z^m)$, m, n = i, j k; ϑ_1 is the ϑ-function with high convergence rate:

$$\vartheta_1 = 2q^{1/4} \cdot \left[\sin(\pi\nu) - q^2 \sin(3 \cdot \pi\nu) + q^6 \sin(5 \cdot \pi\nu) - \ldots \right].$$

Let us consider in more detail the calculation of the complex potential (5) from the known distribution of the magnetization vector $J(z)$ in D. In the simplest case, the discrete analog of this equation, by analogy with (15), takes the form

$$W(z) = W_0(z) + \frac{1}{2\pi} \cdot \sum_k J^k \cdot [\zeta(z - \xi^k) - \\ - \frac{\eta_1}{\omega_1}(z - \xi^k)] \cdot \Delta\tau_k + \frac{\mathrm{j}}{F_\Omega} \sum_k \mathrm{Im}\, J^k \cdot (z \cdot \Delta\tau_k - g_k), \quad (20)$$

where for g_k using the Green formula we obtain

$$g_k = \int_{D^k} \xi \cdot \Delta\tau_k = \frac{1}{2} \int_{D^k} \partial_\xi(\xi^2) \cdot \Delta\tau_k = \frac{\mathrm{j}}{4} \int_{S^k} \xi^2 \cdot \mathrm{d}\bar{\xi} = \\ = \frac{\mathrm{j}}{12} (z_i^3 \cdot a_{kij} + z_j^3 \cdot a_{ijk} + z_k^3 \cdot a_{jki}),$$

and for $\zeta(u) - (\eta_1/\omega_1) \cdot u$ one can use absolutely and uniformly convergent series

$$\zeta(u) - \frac{\eta_1}{\omega_1} \cdot u = \frac{\pi\mathrm{j}}{\omega_1} \cdot \left(\frac{h + h^{-1}}{h - h^{-1}} + 2 \cdot \sum_{n=1}^{\infty} \left[\begin{array}{l} \dfrac{q^{2n} \cdot h^{-2}}{1 - q^{2n} \cdot h^{-2}} - \\ - \dfrac{q^{2n} \cdot h^2}{1 - q^{2n} \cdot h^2} \end{array} \right] \right), \quad (21)$$

or at $-\mathrm{Im}\,\tau < \mathrm{Im}\ \nu < \mathrm{Im}\,\tau$

$$\zeta(u) - \frac{\eta_1}{\omega_1} \cdot u = \frac{\pi}{\omega_1} \cdot \left(\mathrm{ctq}(\pi\nu) + 4 \cdot \sum_{n=1}^{\infty} \frac{q^{2n}}{1 - q^{2n}} \cdot \sin(2\pi n \cdot \nu) \right). \quad (22)$$

A more accurate expression for $W(z)$ can be obtained by passing in (5) to the integral over the boundary S^k. Using (18) and (20), we rewrite (5) as

$$W(z) = W_0(z) - \frac{1}{2\pi} \sum_k J^k \int_{D^k} \partial_\xi [\ln \vartheta_1(\nu, \tau)] \cdot \mathrm{d}\tau_\xi + \\ + \frac{\mathrm{j}}{F_\Omega} \sum_k \mathrm{Im}\, J^k (z\Delta\tau_k - g_k) = W_0(z) - \quad (23) \\ - \frac{\mathrm{j}}{4\pi} \sum_k J^k \int_{S^k} \ln \vartheta_1(\nu, \tau) d\bar{\xi} + \frac{\mathrm{j}}{F_\Omega} \sum_k \mathrm{Im}\, J^k (z\Delta\tau_k - g_k).$$

To calculate the integrals in (23), we use the well-known expansion for the ϑ-function

$$\ln \left(\pi \cdot \frac{\vartheta_1(\nu, \tau)}{\vartheta_1'(0, \tau)} \right) = \ln \sin(\pi\nu) + \\ + 2 \sum_{n=1}^{\infty} \frac{q^{2 \cdot n}}{n \cdot (1 - q^{2 \cdot n})} [1 - \cos(2\pi n \cdot \nu)]. \quad (24)$$

Taking into account that in accordance with (12) $\int_\Gamma d\bar{\xi} \equiv 0$,

$$\int_S \ln \vartheta_1(\nu, \tau) \cdot \mathrm{d}\bar{\xi} = \int_S \ln \sin(\pi\nu) \cdot \mathrm{d}\bar{\xi} - \\ - 2 \sum_{n=1}^{\infty} \int_S a_n \cdot \cos(2\pi n \cdot \nu) \cdot \mathrm{d}\bar{\xi}, \quad (25)$$

where $a_n = q^{2n}/[n \cdot (1 - q^{2n})]$.

Calculation of the first integral in (25) leads to the expression

$$I_1 = \int_{S^k} \ln \sin(\pi\nu) \cdot d\bar{\xi} = \int_{S^k} \ln \left[\pi\nu \cdot \prod_{n=1}^{\infty} (1 - \frac{\nu^2}{n^2}) \right] \cdot \mathrm{d}\bar{\xi} = \\ = \int_{S^k} \ln(z - \xi) \cdot \mathrm{d}\bar{\xi} + \sum_{n=1}^{\infty} \int_{S^k} \ln \left[(z - \xi)^2 - (n \cdot \omega_1)^2 \right] \cdot \mathrm{d}\bar{\xi} = \\ = -a_{kij} \cdot \sum_{n=0}^{\infty} b_n \cdot [u_{1i} \cdot (\ln u_{1i} - 1) + u_{2i} \cdot (\ln u_{2i} - 1)] - \quad (26) \\ - a_{ijk} \cdot \sum_{n=0}^{\infty} b_n \cdot [u_{1j} \cdot (\ln u_{1j} - 1) + u_{2j} \cdot (\ln u_{2j} - 1)] - \\ - a_{jki} \cdot \sum_{n=0}^{\infty} b_n \cdot [u_{1k} \cdot (\ln u_{1k} - 1) + u_{2k} \cdot (\ln u_{2k} - 1)],$$

where $u_{1p} = z - n \cdot \omega_1 - z_p$, $u_{2p} = z + n \cdot \omega_1 - z_p$, p = i, j, k; b_n=0,5 at $n = 0$ and $b_n = 1$ at $n \neq 0$.

Calculation of the second integral in (25) gives:

$$I_2 = -2 \int_{S^k} a_n \cdot \cos(2\pi \cdot n\nu) \cdot \mathrm{d}\bar{\xi} = \sum_{n=1}^{\infty} \frac{a_n \cdot \omega_1}{\pi n} \times \\ \times \left[a_{ijk} \sin(2\pi n\nu^j) + a_{kij} \sin(2\pi n\nu^i) + a_{jki} \sin(2\pi n\nu^k) \right], \quad (27)$$

where

$\nu^j = (z - z^j)/\omega_1, \nu^i = (z - z^i)/\omega_1, \nu^k = (z - z^k)/\omega_1.$

It should be borne in mind that the logarithm is a multivalued function, therefore, when integrating along the boundary S^k, it is necessary to choose its continuous branches.

Examples of numerical implementation. Below are examples of numerical simulations illustrating the capabilities of the method described. Figures 4-8 show field patterns (field lines in blue, equipotentials in red) for a three-component HM with basic periods ω_1=8, ω_2=6j. The external field H_0 is uniform and directed at different angles about the horizontal axis.

In Fig. 5 with the same parameters as in Fig. 4, the field is calculated in the equivalent parallelogram of periods Ω' with $\omega_1' = 8$, $\omega_2' = -8 + 6\mathrm{j}$. Comparison of the field distribution in Fig. 4 and Fig. 5 confirms the conclusion about the conservation of field characteristics at congruent points of equivalent periods. The freedom to choose from equivalent periods of more convenient for calculating and visualizing the results in this case clearly speaks in favor of Fig. 4.

The choice of indicated in Fig. 6 angle 9.2535° is due to the direction of the external field H_0 in the direction of the main axis of anisotropy of the homogenized HM (calculation – see below).

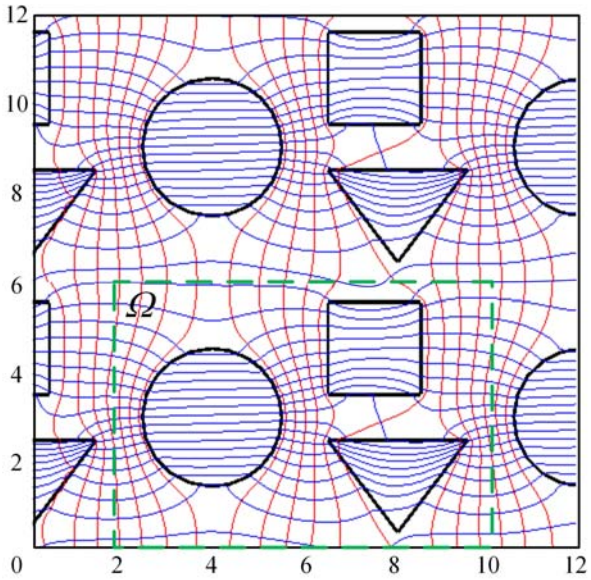

Fig. 4. The field pattern in the three-component HM at relative magnetic permeabilities of discrete elements μ=1000 and the external medium μ_e=1. Green dotted line illustrates the main parallelogram of the periods. External field H_0=1

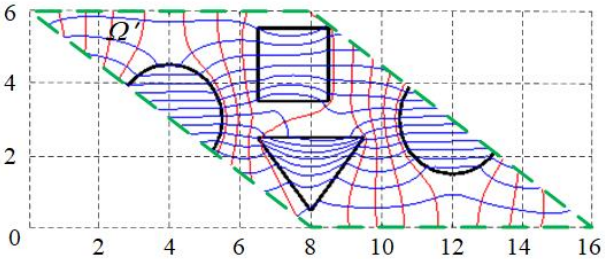

Fig. 5. The field pattern in the equivalent basic period (highlighted in green dotted line) with the HM parameters of Fig. 4

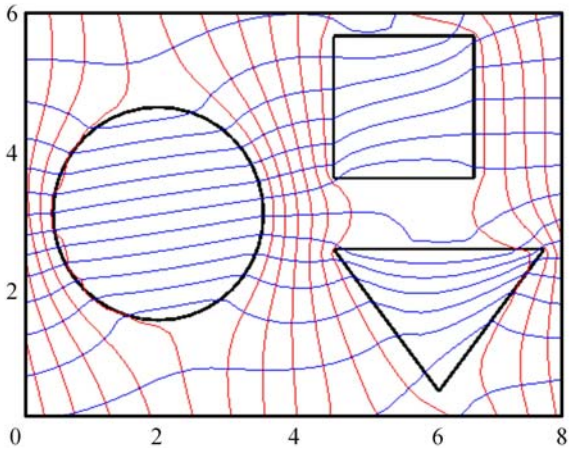

Fig. 6. The same as in Fig. 4, but the external field H_0 is directed at an angle of 9.2535° to *x*-axis

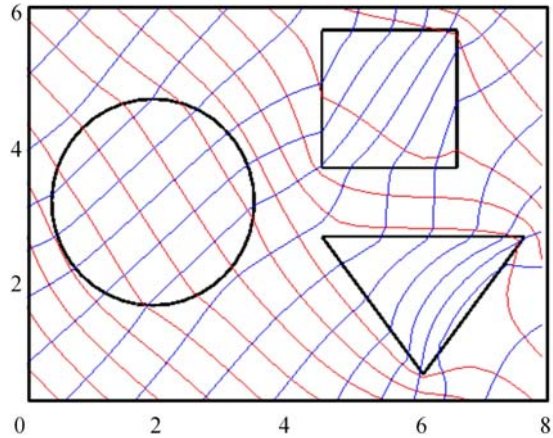

Fig. 7. Relative magnetic permeabilities of triangular, square and round rods, respectively, equal to 1000, 10 and 2, μ_e=1. The external field H_0 is directed at an angle of 45° to *x*-axis

Figures 8, 9 show the results of solution of the flow problem: Fig. 8 shows the flow lines, and Fig. 9 presents the distribution of the magnetization vector in a magnetic sheet with discrete air voids (see Fig. 8). In this case, instead of (9) the following equation is used:

$$J(z) = 2H_0 \cdot \frac{\mu_i(\mu_e - 1)}{\mu_i + \mu_e} - \lambda \cdot \overline{\Pi_\omega J},\ \lambda = \frac{\mu_i - \mu_e}{\mu_i + \mu_e}.$$

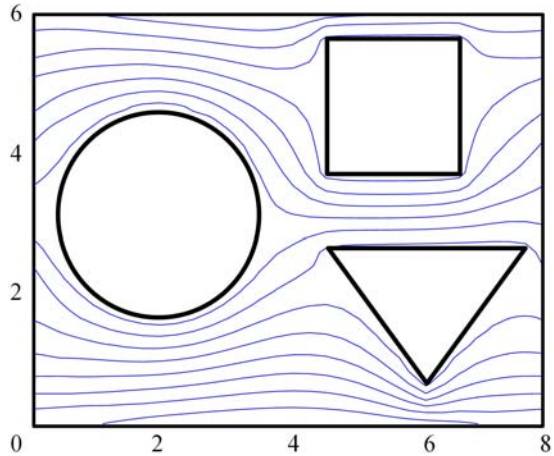

Fig. 8. The flow problem. The relative magnetic permeabilities of discrete elements μ=1, of the external medium μ_e=1000

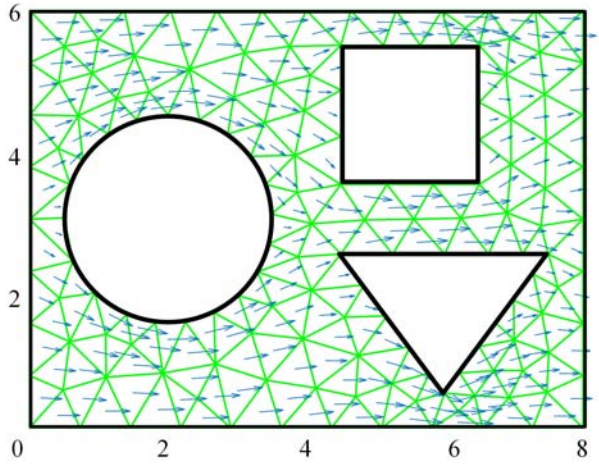

Fig. 9. Discretization of the computational domain and distribution of the magnetization vector in the flow problem (see Fig. 8)

Attention should be paid to an important detail: despite the simple shape of the main parallelogram of periods, the boundary conditions on its sides are not known a priori and cannot be reduced to the conditions commonly used in FEM.

Calculation of effective parameters of a multicomponent HM. Since the above method is based on the determination of the magnetization vector J in the main parallelogram of the periods, solution of the homogenization problem poses no significant difficulties. To do this, it is necessary to calculate $J(z)$, $z\in\Omega$ for two mutually perpendicular external fields H_0, for example, for $H_0 = 1$ and $H_0 = j$. Let us denote the total magnetization of all elements in Ω by $\wp_x=\wp_{xx}+\mathrm{j}\,\wp_{xy}$ and $\wp_y=\wp_{yx}+\mathrm{j}\,\wp_{yy}$, respectively. Then the relative magnetic permittivity tensor $\boldsymbol{\kappa}$ is easily determined through the effective magnetization of the medium: in vector notation $\boldsymbol{J}=\boldsymbol{\wp}/F_\Omega=\boldsymbol{\kappa}\cdot\boldsymbol{H}_0$. Obviously, $\kappa_{xx}=\wp_{xx}/F_\Omega$, $\kappa_{xy}=\wp_{xy}/F_\Omega$, $\kappa_{yx}=\wp_{yx}/F_\Omega$, $\kappa_{yy}=\wp_{yy}/F_\Omega$.

In the general case, for the chosen coordinate system, the tensor $\boldsymbol{\kappa}$ should be symmetric, but not necessarily diagonal. To bring it to a diagonal tensor $\tilde{\boldsymbol{\kappa}}$ with principal $\tilde{\kappa}_{xx},\tilde{\kappa}_{yy}$ $(\tilde{\kappa}_{xy}=\tilde{\kappa}_{yx}=0)$ values, we introduce a new coordinate system (x', y') by rotating the old one by the angle α. This angle can be determined from the expression

$$\alpha=\frac{1}{2}\operatorname{arctg}\left(\frac{2\kappa_{xy}}{\kappa_{xx}-\kappa_{yy}}\right), \tag{28}$$

and the principal values of the tensor $\tilde{\boldsymbol{\kappa}}$ can be determined from the relations

$$\tilde{\kappa}_{xx}=\frac{(\kappa_{xx}+\kappa_{yy})+\sqrt{(\kappa_{xx}-\kappa_{yy})^2+4\kappa_{xy}{}^2}}{2},$$
$$\tilde{\kappa}_{yy}=\frac{(\kappa_{xx}+\kappa_{yy})-\sqrt{(\kappa_{xx}-\kappa_{yy})^2+4\kappa_{xy}{}^2}}{2}. \tag{29}$$

In accordance with the above, for a medium with parameters corresponding to Fig. 4, the following results are obtained:

$$\boldsymbol{\kappa}=\begin{vmatrix}1,0054 & 0,0210\\ 0,0211 & 0,8801\end{vmatrix},\ \tilde{\boldsymbol{\kappa}}=\begin{vmatrix}1,0088 & 0\\ 0 & 0,8766\end{vmatrix},\ \alpha=9,2535°.$$

For the components of the effective relative magnetic permeability tensor, we obtain the obvious values: $\tilde{\mu}_{xx}$ =2,0088, $\tilde{\mu}_{yy}=1,8801$.

To confirm the correctness of the calculations, Fig. 6 shows a picture of the field obtained with an external field strength H_0=1, directed at an angle α = 9.2535° to the x-axis (i.e. along the main axis of anisotropy). For effective magnetization of the medium, a sufficiently accurate result is obtained: $\wp$=1.0089·exp(j·9.2561·π/180).

For the parameters of the HM corresponding to Fig. 7, the corresponding results are equal to:

$$\boldsymbol{\kappa}=\begin{vmatrix}0,4462 & -0,0029\\ -0,0025 & 0,5571\end{vmatrix},\ \tilde{\boldsymbol{\kappa}}=\begin{vmatrix}0,4461 & 0\\ 0 & 0,5572\end{vmatrix},\ \alpha=1,4169°.$$

The components of the tensor of effective relative magnetic permeability: $\tilde{\mu}_{xx}$ =1.4461, $\tilde{\mu}_{yy}=1.5572$. Their decrease in comparison with the above values is explained by a decrease in the effective magnetization of the HM due to smaller values of the magnetic permeabilities of the discrete phases. The insignificant asymmetry of the tensor $\boldsymbol{\kappa}$ is explained by its almost zero non-diagonal components.

Calculation of the field of magnetic forces. To further illustrate the capabilities of the developed method, we present the results of calculating the distribution of the force field $|\boldsymbol{H}|\mathrm{grad}|\boldsymbol{H}|$ = 0,5 grad($|\boldsymbol{H}|^2$). As can be seen from the last expression, the force field of the HGMS matrix is completely determined by the distribution of the modulus of the magnetic field vector $\boldsymbol{H}$ in the working space of the matrix. Within the framework of the developed method, this distribution is easily obtained on the basis of expression (6) using its discrete analogue or the relation $\boldsymbol{H}=-\mathrm{grad}(\mathrm{Re}W(z))$.

To determine the force field $\boldsymbol{F}^*$, it is necessary to specify the vector of the external (background) field strength $\boldsymbol{H_0}$ and the dimensions of the matrix elements. For example, for the HM corresponding to Fig. 4, with the value of the main period ω_1=8 mm (the dimensions of the matrix elements are determined by proportional conversion and are visible from Fig. 4-9) and the external field H_0 =5 kA/m direction along this period, in Fig. 10 lines $|\boldsymbol{H}|^2$=const and the magnetic force vectors $\boldsymbol{F}^*$ perpendicular to them are shown. Since the force field of the matrix is highly heterogeneous, Fig. 10 shows a fragment of the domain with the most intense force field. The areas of magnetic particle capture zones are determined by the known value of the minimum extraction force $\left|\boldsymbol{F}^*\right|_{\min}$, the determination of which is beyond the scope of this paper. As noted above, this force depends on the magnetic susceptibility of the initial product, the size of the extracted fraction, and other technological parameters. For example, at $\left|\boldsymbol{F}^*\right|_{\min}=\left|\boldsymbol{F}\right|_{\min}/(\mu_0\chi V)=5.5\cdot10^9$ A^2/m^3, which roughly corresponds to the real values, the isodines $\left|\boldsymbol{F}^*\right|$ = const and the particle extraction zones are shown in Fig. 11.

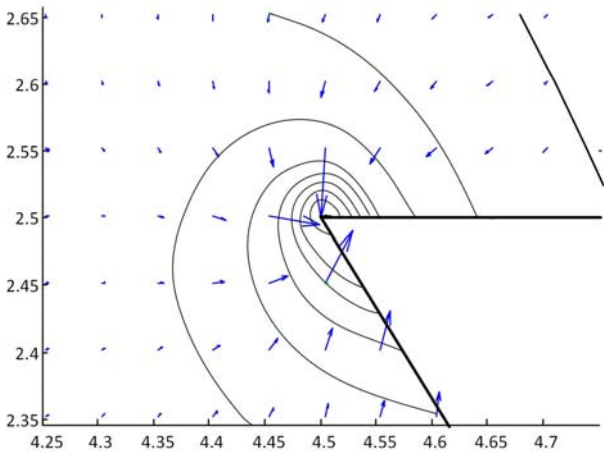

Fig. 10. Characteristics of the force field of the matrix of Fig. 4 in the corner zone of a triangular element

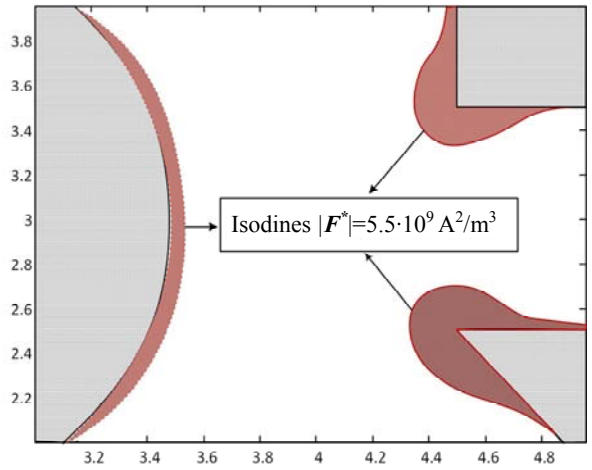

Fig. 11. Isodines $\boldsymbol{F}^*$| = const and their corresponding extraction domains of the force field at $|\boldsymbol{F}^*|_{min}$= 5.5·10^9 A^2/m^3 for a fragment of the matrix working space

The above analysis shows that the high heterogeneity of the force field (even in the extraction zone, the forces can differ by 2-3 orders of magnitude) is a negative factor. It is more preferable to have a field sufficient for extraction with a minimum spread of magnetic forces (ideally, isodynamic). We also note the high sensitivity of the force field to the strength value H_0 and the size of the filter elements. This casts doubt on the universality of the recommendations for determining the optimal geometric shapes of matrix elements without reference to the magnetic system of a particular HGMS and its comprehensive study.

Field analysis of the force field in the matrix can be continued in the following direction. Obviously, the formed extraction zones reduce the area and geometry of the pulp free flow area. The hydraulic permeability of the matrix can be investigated by solving the flow problem (see Fig. 8) with the geometry of liquid-impermeable regions modified due to particle sticking.

Thus, the information obtained on the basis of the developed method can be used in the development of new and modernization of existing HGMS in the following directions:

- calculation of the magnetic permeability tensor values (homogenization problem) makes it possible to quite accurately determine the magnetic resistance of the matrix as the main element of the magnetic system of the separator, and as a result of calculating the distribution of the magnetic flux in it, to determine the average magnetic flux density in the matrix and the calculated value of the field strength H_0. For the considered example, $\tilde{\mu}_{xx} \approx 2$ and H_0=5 kA/m, the average magnetic flux density is B = 0.126 T;
- for the selected geometrical and magnetic parameters of the matrix elements with a known value of strength $\boldsymbol{H}_0$, it is necessary to calculate the field of magnetic forces $|\boldsymbol{F}^*| \geq |\boldsymbol{F}^*|_{min}$ (according to the example of Fig. 10), and for a given value of the minimum holding force $|\boldsymbol{F}^*|_{min}$ – the areas of potential extraction zones and the fill factor of the working space (Fig. 10). It should be borne in mind that the specific magnetic resistance of the matrix does not depend on the absolute dimensions of its elements and the strength of the external field. At the same time, the magnetic forces $|\boldsymbol{F}^*|$ are proportional to $|\boldsymbol{H}_0|^2$ and inversely proportional to the absolute sizes of the elements. From this it follows that the recalculation of the force field in these cases should not be done, since the picture of isodines $|\boldsymbol{F}^*|$ = const remains unchanged, only the values of their values change;
- calculated configuration of liquid-tight areas makes it possible to evaluate the hydraulic permeability of the pulp and decide on a change in the force field $\boldsymbol{F}^*$ in one direction or another;
- varying the geometric sizes and shapes of the matrix elements and conducting a series of corresponding computational experiments, it is possible to optimize the HGMS magnetic system as a whole with given technological limitations.

Thus, the use of the proposed method will create additional opportunities for improving the technical characteristics of electrophysical devices with HM elements, for example, high-gradient magnetic separators, electrostatic filters, and other structures for which the universality and accuracy of calculating effective and especially local field characteristics are decisive.

Conclusions.

1. A universal method has been developed for calculating the local and effective characteristics of the magnetic field of a multicomponent heterogeneous medium with a doubly periodic structure which is based on solving the integral equation with respect to the magnetization vector of the elements of the main parallelogram of the periods.

2. The performed computational experiments confirm the high efficiency and accuracy of the proposed method. Its main advantages are the compactness of the computational domain, the absence of the need to specify unknown boundary conditions on the sides of the parallelogram of the periods and severe restrictions on the geometry and number of components of a heterogeneous medium.

3. One of the effective areas of application of the developed method is the analysis of the force fields of matrices of high-gradient magnetic separators. The ability to comprehensively take into account the factors

determining the effective and local field characteristics opens up additional possibilities for optimizing the matrix parameters and improving the overall dimensions and technological characteristics of the separator as a whole.

4. Without significant changes, the method can be used in the analysis of other potential fields in doubly periodic systems (design of electrostatic filters, problems of flowing around gratings of a complex profile, etc.).

REFERENCES

1. Yemets Y.P. *Elekricheskie harakteristiki kompozicionnih materialov s reguliarnoi ctrukturoi* [Electrical characteristics of regular structure composites]. Kyiv, Naukova Dumka Publ., 1986. 191 p. (Rus).

2. Tolmachev S.T. *Specialnie metody resheniia zadach magnitostatiky* [Special methods for solving magnetostatic problems]. Kyiv, Vyshcha shkola Publ., 1983. 166 p. (Rus).

3. Kowalczyk P., Bielski W., Idzik A. Effective conductivity in two-dimensional two-component structures: macroscopic isotropy. *Photonics Applications in Astronomy, Communications, Industry, and High-Energy Physics Experiments*, 2014, T. 9290, P. 92901A. **doi: 10.1117/12.2075144.**

4. Earhart C.M., Nguyen E.M., Wilson R.J., Wang Y.A., Wang S.X. Designs for a microfabricated magnetic sifter. *IEEE Transactions on Magnetics*, 2009, vol. 45, no. 10, pp. 4884-4887. **doi: 10.1109/tmag.2009.2026486.**

5. Ge W., Encinas A., Araujo E., Song S. Magnetic matrices used in high gradient magnetic separation (HGMS): A review. *Results in Physics*, 2017, vol. 7, pp. 4278-4286. **doi: 10.1016/j.rinp.2017.10.055.**

6. Oder R. High gradient magnetic separation theory and applications. *IEEE Transactions on Magnetics*, 1976, vol. 12, iss. 5, pp. 428-435. **doi: 10.1109/TMAG.1976.1059076.**

7. Svoboda J. *Magnetic Techniques for the Treatment of Materials.* Kluwer Academic Publ., 2004. 642 p. **doi: 10.1007/1-4020-2107-0.**

8. Ren L., Zeng S., Zhang Y. Magnetic field characteristics analysis of a single assembled magnetic medium using ANSYS software. *International Journal of Mining Science and Technology*, 2015, vol. 25, no. 3, pp. 479-487. **doi: 10.1016/j.ijmst.2015.03.024.**

9. Song C.C., Ning G.H., Yuan Z.Y., Jing L.X., Hui C.C., Yao M.S. Investigation of the influence of different matrix rotation angles on the surrounding magnetic field in a uniform magnetic field. *Ming Metall Eng*, 2014, no. 34, pp. 290-294.

10. Gerlici J., Shvedchykova I.O., Romanchenko J.A., Nikitchenko I.V. Determination of the rational geometrical parameters of plate type elements of magnetic matrix of the polygradient separator. *Electrical engineering & electromechanics*, 2018, no.4, pp. 58-62. **doi: 10.20998/2074-272X.2018.4.10.**

11. Hou L.S., Geng L. *A kind of high gradient magnetic matrix for high-intensity magnetic separator*, CN. Patent, 2012.

12. Zheng X., Wang Y., Lu D., Li X. Study on the application of elliptic cross-section matrices for axial high gradient magnetic separation: key considerations for optimization. *Physicochemical Problems of Mineral Processing*, 2019, vol. 55(3), pp. 655-666. **doi: 10.5277/ppmp18178**.

13. Ding L., Chen L.Z., Zeng J.W. Investigation of combination of variable diameter rod elements in rod matrix on high gradient magnetic separation performance. *Advanced Materials Research*, 2014, vol. 1030-1032, pp. 1193-1196. **doi: 10.4028/www.scientific.net/amr.1030-1032.1193.**

14. Tolmachev S.T., Rozhnenko Z.G. Complex solve of a magnetostatic problem in systems with ordered heterogeneous medium. *Bulletin of NTU «KhPI»*, 2008, no. 40, pp. 139-145. (Rus).

15. Hurwitz A., Courant R. *Vorlesungen über allgemeine Funktionentheorie und elliptische Funktionen*. J. Springer, 1922. 399 p. (Ger).

16. Tolmachev S.T., Bondarevskyi S.L. Classification of heterogeneous structures and conditions of their doubly periodicity. *Eastern-European journal of enterprise technologies*, 2013, vol. 5, no. 5(65), pp. 24-29. (Rus).

Received 20.08.2019

S.T. Tolmachev[1]*, Doctor of Technical Science, Professor,*
S.L. Bondarevskyi[1]*, Candidate of Technical Science, Associate Professor,*
A.V. Il'chenko[1]*, Candidate of Technical Science, Associate Professor,*
[1] Kryvyi Rih National University,
11, Vitaly Matusevich Str., Kryvyi Rih, Dnipropetrovsk Region, 50027, Ukraine,
e-mail: kafem.knu@gmail.com

How to cite this article:
Tolmachev S.T., Bondarevskyi S.L., Il'chenko A.V. Magnetic properties of multicomponent heterogeneous media with a doubly periodic structure. *Electrical engineering & electromechanics*, 2020, no.1, pp. 29-38. **doi: 10.20998/2074-272X.2020.1.05.**

UDC 621.3.022: 621.315.3: 629.7 **doi: 10.20998/2074-272X.2020.1.06**

M.I. Baranov

A CHOICE OF ACCEPTABLE SECTIONS OF ELECTRIC WIRES AND CABLES IN ON-BOARD CIRCUITS OF AIRCRAFT ELECTRICAL EQUIPMENT

Purpose. *Implementation of choice of maximum permissible sections S_{il} of the uninsulated wires and insulated wires (cables) with copper (aluminum) cores (shells) in the on-board power circuits of electrical equipment of different aircrafts with AC current of frequency f>50 Hz.* ***Methodology.*** *Theoretical bases of the electrical engineering, electrophysics bases of technique of high voltage and high pulsed currents, applied thermal physics.* ***Results.*** *The engineering approach is developed for a calculation choice on the condition of thermal resistibility of aircraft cable-conductor products (CCP) of maximum permissible sections S_{il} of the uninsulated wires, insulated wires and cables with copper (aluminum) cores (shells), polyvinyl chloride (PVC), rubber (R) and polyethylene (PET) insulation, on which in malfunction of operation of on-board aircraft network with AC frequency of f>50 Hz flows of $i_k(t)$ current at single phase short circuit (SC) with given amplitude-temporal parameters. It is determined that in the on-board power circuits of electrical equipment of aircrafts (f=400 Hz; for permanent time of slump of T_a=3 ms of aperiodic constituent of current of SC) maximum permissible amplitudes of current density of $\delta_{ilm} \approx I_{mk}/S_{il}$ of single phase SC at time of its disconnecting t_{kC}=5 ms in the on-board network of aircraft without dependence on the numerical value of amplitude I_{mk} of the given current of SC for the uninsulated wires with copper (aluminum) cores is accordingly about 2.48 (1.40) kA/mm^2, for wires (cables) with copper (aluminum) cores (shells) and PVC (R) with insulation – 1.85 (1.18) kA/mm^2, and for wires (cables) with copper (aluminum) cores (shells) and PET insulation – 1.53 (0.99) kA/mm^2. The influence on a choice in the on-board network of aircrafts of maximum permissible sections S_{il} of its CCP and accordingly maximum permissible amplitudes of current density δ_{ilm} of current copper (aluminum) parts of its wires and cables of frequency f of AC in the on-board network of aircraft is determined, but duration of flow t_{kC} (time of disconnecting) renders in the on-board network of aircrafts of emergency current of SC $i_k(t$. For diminishing in the on-board power circuits of electrical equipment of aircrafts of maximum permissible sections S_{il} of the electric wires (cables) applied in them and accordingly providing of decline for different aircrafts of mass and overall indicators of their on-board CCP is needed in the on-boar networks of aircrafts along with the use of enhance frequency of f=400 Hz of AC to apply the fast-acting devices of their protecting from SC in course of time wearing-outs of t_a<<100 ms. It isshown that application of enhance frequency of f=400 Hz of AC in the on-board networks of aircrafts as compared to its frequency of f=50 Hz results in the considerable increase (in four times) of fast-acting of devices of their protection from SC, operation of which is based on the air electric explosion of metallic wire.* ***Originality.*** *First for the on-board network of aircrafts with AC of frequency of f=400 Hz the maximum permissible sections S_{il} and amplitudes of current density δ_{ilm} of SC are determined for the uninsulated wires and insulated wires (cables) with copper (aluminum) cores (shells), PVC, R and PET insulation.* ***Practical value.*** *Theobtained results will be used in the increase of thermal resistibility of CCP with copper (aluminum) cores (shells), PVC, R and PET insulation applied in the on-board electric networks of different aircrafts.* References 18, tables 5.

Key words: **aircraft, on-board power circuits of electrical equipment, electric wires and cables, frequency of alternating current, selection of maximum permissible cross-sections of cable products.**

Надані результати *запропоноаного інженерного електротехнічного підходу до розрахункового вибору гранично допустимих поперечних перерізів S_{il} електричних неізольованих дротів, ізольованих дротів і кабелів з полівінілхлоридною (ПВХ), гумовою (Г) і поліетиленовою (ПЕТ) ізоляцією і мідними (алюмінієвими) жилами (оболонками) по умові їх термічної стійкості, по яких у бортових силових колах електрообладнання літальних апаратів (ЛА) в аварійному режимі протікає струм $i_k(t)$ однофазного короткого замикання (КЗ) із заданими амплітудно-часовими параметрами. На підставі цього підходу здійснений вибір гранично допустимих поперечних перерізів S_{il} для вказаних дротів (кабелів) бортових силових кіл електрообладнання ЛА з частотою змінного струму f=400 Гц. Виконана розрахункова оцінка гранично допустимих амплітуд щільності δ_{ilm} струму $i_k(t)$ вказаного КЗ в даних дротах і кабелях бортових силових кіл ЛА.* Бібл. 18, табл. 5.

Ключові слова: **літальний апарат, бортові силові кола електрообладнання, електричні дроти і кабелі, частота змінного струму, вибір гранично допустимих перерізів кабельно-провідниковій продукції.**

Приведены результаты *предложенного инженерного электротехнического подхода к расчетному выбору предельно допустимых поперечных сечений S_{il} электрических неизолированных проводов, изолированных проводов и кабелей с поливинилхлоридной (ПВХ), резиновой (Р) и полиэтиленовой (ПЭТ) изоляцией и медными (алюминиевыми) жилами (оболочками) по условию их термической стойкости, по которым в бортовых силовых цепях электрооборудования летательных аппаратов (ЛА) в аварийном режиме протекает ток $i_k(t)$ однофазного короткого замыкания (КЗ) с заданными амплитудно-временными параметрами. На основании этого подхода осуществлен выбор предельно допустимых поперечных сечений S_{il} для указанных проводов (кабелей) бортовых силовых цепей электрооборудования ЛА с частотой переменного тока f=400 Гц. Выполнена расчетная оценка предельно допустимых амплитуд плотности δ_{ilm} тока $i_k(t)$ указанного КЗ в рассматриваемых проводах и кабелях бортовых силовых цепей ЛА.* Библ. 18, табл. 5.

Ключевые слова: **летательный аппарат, бортовые силовые цепи электрооборудования, электрические провода и кабели, частота переменного тока, выбор предельно допустимых сечений кабельно-проводниковой продукции.**

Introduction. In [1, 2], as applied to the tasks of industrial electric power industry, the issues of a refined choice of the maximum allowable S_{il} and critical S_{iC} cross-sections of uninsulated electric wires, as well as insulated wires and cables with polyvinyl chloride (PVC), rubber (R) and polyethylene (PET) insulation and copper (aluminum) cores (sheaths) according to conditions of

their, respectively, thermal stability and electric explosion (EE) are considered. As is known, the calculation modes for choosing the maximum allowable cross-sections S_{il} of cable-conductor products (CCP) used in power circuits of electrical equipment with alternating current of frequency f=50 Hz are the modes of single or three-phase short circuit (SC) [3, 4]. The technical data given in [1-4] for the selection of CCP relate to power circuits of electrical equipment used in land-based stationary objects during their industrial power supply with AC with frequency of f=50 Hz. And what about the choice of the maximum allowable cross-sections S_{il} of CCP for objects of aviation and rocket and space technology, in the on-board electrical networks of which it is possible to use alternating current with frequency f, significantly different from the traditional power frequency of 50 Hz? It is no secret that the overall dimensions and mass indicators of the on-board CCP, and hence the cross-sectional values S_{il} of its metal conductors (shell-screens), for such objects «go» to the forefront of the developers of this high technology. In this part, it should be noted that, for example, on the modern Airbus 380 airliner, the length of CCP of its on-board network is more than 530 km [5]. Here, the total power of electric power sources on board of military and civil aircrafts can range from 20 kW for light aircrafts to 600 kW and more for heavy aircrafts [6]. In this regard, the tasks related to the study of the peculiarities of application of AC with frequency f>50 Hz in the on-board power circuits of aircraft electrical equipment and the choice of maximum permissible cross-sections S_{il} of electrical wires and cables containing internal copper (aluminum) cores (i=1) and external reverse (protective) shells (i=2), as well as PVC, R and PET belt insulation for such frequencies become relevant in the field of applied electrical engineering in relation to modern aircraft.

The goal of the paper is the choice of the maximum permissible cross-sections S_{il} of bare wires and insulated wires (cables) with copper (aluminum) cores (shells) in the on-board power circuits of electrical equipment of various aircrafts with alternating current with frequency f>50 Hz.

1. Problem definition. Let us consider uninsulated copper and aluminum wires widely used in on-board power circuits of aircraft electrical equipment, as well as insulated wires and cables with copper (aluminum) inner cores and outer shell-shields, having PVC, R and PET belt (protective) insulation [7]. We assume that in round solid (split) copper (aluminum) cores (shells) of the indicated wires (cables) of the power circuits of the aircraft electrical equipment located in the air at temperature of θ_0=20 °C in the normal mode of their operation under the rated current load, in the longitudinal direction alternating current flows with frequency f>50 Hz, and the maximum long-term permissible temperature θ_{ll} of the Joule heating for non- and insulated wires (cables) with PVC, R and PET insulation does not numerically exceed those regulated by the applicable for electric power devices of levels of 70 °C and 65 °C, respectively [8]. Suppose that, for the generality of the electrical engineering problem to be solved, in the power circuits of aircrafts with CCP, their operation modes are possible when some sections of their wires (cables) can be completely de-energized. We believe that the thermal stability of the electrical wires and cables of the aircraft on-board circuits under consideration, as well as for stationary ground electric equipment with a two-wire power supply network, is limited by the maximum permissible short-term heating temperature θ_{lS} of the current-carrying parts of wires (cables) at the single-phase type of SC in the aircraft on-board network under study. In the first approximation of the solution of the formulated problem, we assume that the values of θ_{lS} correspond to the known maximum permissible short-term heating temperatures of the CCP with alternating SC current of power frequency f=50 Hz [8]. In this regard, the numerical values of the temperature θ_{lS} for uninsulated copper wires with strains less than 20 N/mm^2 will be 250 °C, and for uninsulated aluminum wires with strains less than 10 N/mm^2 – 200 °C [8]. For insulated wires and cables with copper and aluminum cores, PVC and R insulation, the numerical values of the temperature θ_{lS} then turn out to be 150 °C, and for the considered CCP with PET insulation – 120 °C [8]. We assume that when choosing the cross-sections S_{il}, the electric current $i_k(t)$ of the single-phase SC in the on-board network of the aircrafts, made according to a single or two-wire circuit, is almost uniformly distributed over the cross-section of the core and the screen-shell of the studied wire (cable).

The justification for this assumption is that the minimum penetration depth Δ_i of the magnetic field (skin layer thickness) from the current $i_k(t)$ of a single-phase SC in the on-board network of the aircraft in a quasi-stationary approximation to the conductive non-ferromagnetic materials of the core (screen-shell) under consideration, determined from the calculation relation $\Delta_i \approx [1/(\pi f \mu_0 \gamma_{0i})]^{1/2}$ [9], where γ_{0i} is the specific conductivity of the core (shell) of the core (shell) of CCP at θ_0=20 °C, and $\mu_0=4\pi\cdot10^{-7}$ H/m is the magnetic constant, for example, for emergency current frequencies f=50 Hz and f=400 Hz is numerically for copper ($\gamma_{0i}=5.81\cdot10^7$ (Ω·m)$^{-1}$) respectively about 9.3 mm and 3.3 mm, and for aluminum ($\gamma_{0i}=3.61\cdot10^7\cdot$(Ω·m)$^{-1}$) about 11.8 mm and 4.2 mm. It can be seen that the indicated values of the skin layer thickness Δ_i turn out to be comparable with the radii (thicknesses) of the current-carrying cores (shells) of wires and cables, usually used in electrical circuits of the aircrafts under consideration (in particular, in aircraft networks [7]). As in [1, 2], we use the condition of the adiabatic nature of the action of the current $i_k(t)$ of a single-phase SC in the on-board network of the aircraft, no more than $t_{kC}=40f^{-1}$=100 ms in the conductive materials of the cores (shells) of the thermal process in CCP under consideration, in which the influence of heat transfer from the surfaces of their current-carrying parts having current temperature $\theta_{iS} \geq \theta_0$, and the thermal conductivity of the layers of their electrically conductive materials and insulation on the Joule heating of the current-carrying parts of the cores (shells) of the studied wires (cables) can be neglected. It is required by

calculation in an approximate form, taking into account the nonlinear nature of the change, due to the Joule heating of the investigated CCP of the specific conductivity γ_i of the material of its cores (shells) and the conditions of the thermal resistibility of the CCP to the action of the current $i_k(t)$ of a single-phase SC in the on-board network of the aircraft to determine in the range of change of AC frequency f = (50-400) Hz in the power circuits of its electrical equipment the maximum permissible cross-sections S_{il} of current-carrying parts for uninsulated copper (aluminum) wires, as well as for insulated wires and cables with copper (aluminum) cores (shells), PVC, R and PET insulation, through which in emergency operation mode of the aircraft single-wire on-board network (with a common «minus» on its massive metal casing, which serves as a reverse current lead [10]) or two-wire on-board aircraft network [11] current of a single-phase SC $i_k(t)$ flows with known duration t_{kC} and with specified amplitude-temporal parameters (ATPs). In addition, taking into account the obtaining of cross-sections S_{il}, it is necessary for the investigated CCP in the aircraft to determine also the maximum permissible density amplitudes δ_{ilm} of the current $i_k(t)$ of a single-phase SC in the on-board network of the aircraft.

2. An engineering approach to the selection of the maximum allowable cross-sections S_{il} of wires and cables in aircraft electrical equipment circuits. From the heat balance equation for the current-carrying parts of the CCP of the aircraft electrical equipment circuits in the adiabatic mode and the conditions of their thermal resistibility to the current $i_k(t)$ of the indicated SC, the analytical expression for the calculation of the maximum permissible cross-sections S_{il} of the considered electric wires and cables takes the following form [1]:

$$S_{il} = \left[J_{ak}/(J_{ilS} - J_{ill})\right]^{1/2} = J_{ak}^{1/2}/C_{ik}, \qquad (1)$$

where $J_{ak} = \int_0^{t_{kC}} i_k^2(t)dt$ is the Joule (action) integral of current $i_k(t)$ of a single-phase SC, $A^2 \cdot s$; J_{ilS}, J_{ill} are the current integrals for current-carrying parts of wires (cables), the maximum permissible short-term temperature and long-term permissible material heating temperature are θ_{lS} and θ_{ll}, respectively, $A^2 \cdot s \cdot m^{-4}$; $C_{ik}=(J_{ilS}-J_{ill})^{1/2}$ is the calculation coefficient, $A \cdot s^{1/2} \cdot m^{-2}$.

It clearly follows from (1) that for the calculation determination of the values of the cross-sections S_{il}, it is necessary to know the values of the Joule integral J_{ak} and the coefficient C_{ik}.

2.1. Determination of current integrals J_{ilS}, J_{ill} and coefficient C_{ik} for CCP of on-board aircraft network. To calculate with engineering accuracy the values of the current integrals J_{ilS} and J_{ill} included in (1), used, in particular, in [9] in the form of current or inertia integrals (see formula 4.56), whose integrand, unlike the classical Joule integral, does not contain the square of the emergency current $i_k(t)$, but the square of the density of this current $\delta_{ik}(t)$ in the electrically conductive materials of the CCP of the aircraft on-board network, we use the following approximate analytical expressions [1, 12]:

$$J_{ilS} = \gamma_{0i}\beta_{0i}^{-1}\ln\left[c_{0i}\beta_{0i}(\theta_{lS} - \theta_0) + 1\right]; \qquad (2)$$

$$J_{ill} = \gamma_{0i}\beta_{0i}^{-1}\ln\left[c_{0i}\beta_{0i}(\theta_{ll} - \theta_0) + 1\right], \qquad (3)$$

where c_{0i}, β_{0i} are, respectively, quantifiable at θ_0=20 °C the specific volumetric heat capacity (J/(m^3·°C)) and the thermal coefficient of the electrical conductivity (m^3/J) of the conductive material of the core (shell) of the wire (cable) of on-board power circuit of the aircraft electrical equipment with current frequency f>50 Hz before exposure to the CCP of the emergency current $i_k(t)$ of a single-phase SC in the on-board network of the aircraft with specified ATPs.

Table 1 shows the numerical values of the used in (2), (3) electrophysical parameters γ_{0i}, c_{0i} and β_{0i} for the main conductive materials used in the current-carrying parts of the CCP of the aircraft on-board network at temperature equal to θ_0=20 °C [9, 12].

Table 1

Numerical values of the characteristics of the basic materials of current-carrying cores (shells) of non- and insulated wires (cables) of power circuits of electrical equipment of the aircraft on-board network at θ_0=20 °C [9, 12]

Core (shell) material of wire (cable)	Numerical value of the characteristic		
	γ_{0i}, $10^7 \cdot (\Omega \cdot m)^{-1}$	c_{0i}, $10^6 \cdot J/(m^3 \cdot °C)$	β_{0i}, $10^{-9} \cdot m^3/J$
Copper	5.81	3.92	1.31
Aluminum	3.61	2.70	2.14

Using the values of the indicated characteristics γ_{0i}, c_{0i} and β_{0i} (see Table 1), for given values of the normalized temperatures θ_0, θ_{lS} and θ_{ll}, using (2), (3), numerical values of the desired current integrals J_{ilS}, J_{ill}, and coefficient C_{ik} used in (1) for a wide range of CCP used in on-board power circuits of electrical equipment of various aircrafts can be found. Table 2 shows the numerical values of the calculated coefficient C_{ik} for the main versions of the CCP, which is widely used in the on-board power circuits of electrical equipment of various aircrafts.

Table 2

The numerical values of the coefficient C_{ik} for non- and insulated wires (cables) with copper (aluminum) cores (shells) used in on-board power circuits of aircraft electrical equipment [1]

Type of insulation in the wire (cable) of the aircraft electrical equipment circuit	Core (shell) material of wire (cable)	Numerical value of C_{ik}, 10^8 A·s$^{1/2}$/m^2	
		$J_{ill} \neq 0$	$J_{ill}=0$
Without insulation	Copper	1.56	1.86
	Aluminum	0.88	1.09
PVC, R	Copper	1.16	1.51
	Aluminum	0.74	0.97
PET	Copper	0.96	1.36
	Aluminum	0.62	0.88

In Table 2, the case when $J_{ill} \neq 0$ corresponds to the rated current load of the CCP in the on-board power circuits of the aircraft electrical equipment under study (the temperature of their current-carrying parts is θ_{ll}), and the case when $J_{ill}=0$ corresponds to the de-energized state of the CCP in the aircraft (temperature of their current-carrying parts before flowing through them of the current $i_k(t)$ of a single-phase SC in the on-board network of the

aircraft corresponds to the temperature of the surrounding CCP the air environment, which we adopted equal to θ_0=20 °C). Next, we focus on finding the Joule integral J_{ak}, which is the main parameter for the calculation determination of the desired cross-section S_{il} by (1).

2.2. Determination of the integral of action J_{ak} of emergency current during SC in the on-board network of an aircraft. To do it, we first write down the analytical relation describing the variation in time t of current $i_k(t)$ of a single-phase SC in the on-board power circuits of electrical equipment used in various aircraft and launch vehicles and fed from an on-board AC source with frequency of f>50 Hz. According to [1, 4], the ATPs of this current $i_k(t)$ of SC in the on-board network of an aircraft containing active and reactive resistances obey the following time dependence:

$$i_k(t) = I_{mk}[\exp(-t/T_a) - \cos(2\pi ft)], \quad (4)$$

where I_{mk} is the amplitude of the steady current $i_k(t)$ of SC in the power circuit of the electrical equipment of the aircraft, A; T_a is the decay time constant of the aperiodic component of the emergency current $i_k(t)$ of SC in the on-board circuit of the aircraft, s.

From (4) at f=400 Hz and t=1.25 ms, which corresponds to the largest amplitude of the shock current $i_k(t)$ of a single-phase SC in the on-board network of the aircraft, an analytical expression for the calculated shock coefficient k_S, which is typical for the considered on-board power supply system of the aircraft in emergency mode follows:

$$k_S = \left[1 + \exp(-0{,}00125/T_a)\right]. \quad (5)$$

At T_a=3 ms, according to (5), the value of the shock coefficient k_S turns out to be numerically equal to 1.66. Therefore, at an operating voltage of alternating current with frequency f=400 Hz in the on-board network of an aircraft produced, for example, by an on-board converter of the ПОС-1000 type and equal to 115 V [6], in the single-phase SC mode the amplitude of the shutdown current is in accordance with the data [13-15] can reach a level of (2-25) kA.

Then, taking into account (1) and (4), the expression for the desired integral of action J_{ak} of the current $i_k(t)$ of the SC in the on-board circuit of the aircraft electrical equipment in the accepted approximation takes on the following analytical form [1]:

$$\begin{aligned} J_{ak} = I_{mk}^2 \{ & 0{,}5t_{kC} + 0{,}25(\pi f)^{-1}\sin(2\pi f t_{kC}) \times \\ & \times \cos(2\pi f t_{kC}) - 2T_a^2(1 + 4\pi^2 f^2 T_a^2)^{-1}\left[e^{-t_{kC}/T_a} \times \right. \\ & \left. \times [2\pi f \sin(2\pi f t_{kC}) - T_a^{-1}\cos(2\pi f t_{kC}) + T_a^{-1}]\right] + \\ & + 0{,}5T_a(1 - e^{-2t_{kC}/T_a})\}. \end{aligned} \quad (6)$$

From (6) it follows that the values of the action integral J_{ak} of the SC current $i_k(t)$ in the aircraft on-board power supply system are directly proportional to the square of the amplitude I_{mk} of the steady-state SC current and duration t_{kC} (switching off time equal to the operation time t_a of the on-board protection devices [13, 14]) against the course of the SC under consideration. It can be seen that the larger the numerical values of I_{mk} and t_{kC}, the greater will be the numerical values of the desired value of the integral J_{ak}. Table 3 at T_a=3 ms (f=400 Hz) for four fixed numerical values of the amplitude I_{mk} of the steady-state SC current (3, 5, 10, and 30 kA) and two possible numerical values of the duration t_{kC} of a single-phase SC in the on-board network of the aircraft (5 ms and 100 ms) according to [13, 14] shows the numerical values of the action integral J_{ak} of the current $i_k(t)$ of the indicated SC calculated according to (6).

Table 3

Numerical values of the action integral J_{ak} for the SC current $i_k(t)$ according to (4), flowing in the on-board power circuits of the aircraft electrical equipment (f = 400 Hz; T_a = 3 ms)

Numerical value of the amplitude I_{mk} of the steady-state current $i_k(t)$ of a single-phase SC in the on-board power circuit of the aircraft electrical equipment, kA	Value of the action integral J_{ak} for the Sc current $i_k(t)$ by (4), $A^2 \cdot s$	
	t_{kC}=5 ms	t_{kC}=100 ms
3	$3.55 \cdot 10^4$	$4.63 \cdot 10^5$
5	$9.86 \cdot 10^4$	$12.86 \cdot 10^5$
10	$39.46 \cdot 10^4$	$51.44 \cdot 10^5$
30	$35.51 \cdot 10^5$	$46.30 \cdot 10^6$

Determining by (6) the values of the action integral J_{ak} of the SC current $i_k(t)$ (see Table 3) and knowing the numerical values of the coefficient C_{ik} (see Table 2), on the basis of (1) numerical values of the maximum permissible cross-sections S_{il} of current-carrying parts of the CCP under consideration in the on-board power circuits of the aircraft electrical equipment can be found. Using the assumptions made, for given amplitudes I_{mk} from a relationship of the form $\delta_{ilm} \approx I_{mk}/S_{il}$, the maximum permissible current density amplitudes δ_{ilm} in the materials of the cores (shells) of the CCP under study of the aircraft on-board network for emergency SC conditions can be quantified.

2.3. The results of the selection of the maximum allowable cross-sections S_{il} and current densities δ_{ilm} in the wires and cables of the on-board network of the aircraft. Table 4 shows the results of the calculation according to (1), taking into account the data summarized in Table 2, 3, of maximum permissible cross-sections S_{il} of current-carrying copper (aluminum) parts of the CCP of on-board power circuits of the aircraft electrical equipment at =400 Hz, $J_{ill} \neq 0$, t_{kC}=5 ms and amplitude I_{mk} of a single-phase SC current $i_k(t)$ in the onboard network of the aircraft (launch vehicle), which varies discretely in the range (3-30) kA.

Table 4

Values of the maximum allowable cross-sections S_{il} for wires (cables) with copper (aluminum) cores (shells) in the on-board power circuits of the aircraft electrical equipment with current amplitude I_{mk} of single-phase SC current $i_k(t)$ from 3 to 30 kA (f=400 Hz; $J_{ill} \neq 0$; t_{kC}=5 ms; T_a=3 ms)

Type of insulation in the wire (cable) of the aircraft electrical equipment circuit	Core (shell) material of wire (cable)	Cross-section value S_{il}, mm^2			
		Amplitude I_{mk} of the steady-state SC current, kA			
		3	5	10	30
Without insulation	Copper	1.21	2.01	4.03	12.08
	Aluminum	2.14	3.57	7.14	21.41
PVC, R	Copper	1.62	2.71	5.41	16.24
	Aluminum	2.55	4.24	8.49	25.46
PET	Copper	1.96	3.27	6.54	19.63
	Aluminum	3.04	5.06	10.13	30.39

It should be pointed out that the questions of choosing the maximum permissible cross-sections S_{il} of cores (shells-shields) of the studied CCP for the case when f=50 Hz (J_{ill}≠0; t_{kC}=(100-160) ms; I_{mk}=(30-100) kA; T_a=20 ms) were considered in detail by the author in [1]. Comparing the data for S_{il} from the above Table 4 and from Table 5 in [1], we can conclude that the transition in the on-board network of an aircraft to AC frequency of f=400 Hz (eight times the frequency f=50 Hz used in power circuits of ground-based power facilities) allows for the use in the on-board network of the aircraft of high-speed protection devices against SC (for example, type A3-250 for currents with amplitude of up to 6 kA) [13, 14] and, accordingly, a sharp decrease at f=400 Hz in time t_{kC} of the action of the current $i_k(t)$ of a single-phase SC in the on-board network of an aircraft (from 100 ms to 5 ms) significantly reduce the numerical values of the maximum allowable cross-sections S_{il} of its copper (aluminum) wires and cables (for emergency operation at I_{mk}=30 kA about 3.9 times). This can lead to a similar decrease (3.9 times) in the overall dimensions and mass indicators of the indicated CCP installed on board of the aircraft. Of course, in spite of the indicated advantages of using in aircraft on-board networks of AC frequency f=400 Hz and fast-acting circuit breakers protecting against SC (for example, for A3-250 circuit breakers t_a=5 ms), this is not so easily to transfer available in aviation and space techniques and circuit-technical solutions in part of thermal protection against SC of relatively low-power low-voltage aircraft on-board networks (f=400 Hz) to ground powerful high-voltage electric networks of industrial power supply (f=50 Hz).

From the data of Table 4 it follows that the maximum permissible amplitude of the density $\delta_{ilm}\approx I_{mk}/S_{il}$ of the current $i_k(t)$ of a single-phase SC at the time of its flow (shutdown) t_{kC}=5 ms in the on-board power circuits of the aircraft electrical equipment (f=400 Hz; T_a=3 ms) for uninsulated wires with copper and aluminum cores are approximately 2.48 kA/mm^2 and 1.40 kA/mm^2, respectively, for cables with copper (aluminum) cores (shells), PVC and R insulation – 1.85 (1.18) kA/mm^2, and for cables with copper (aluminum) cores (shells) and PET insulation – 1.53 (0.99) kA/mm^2. Here, the indicated numerical values of the maximum permissible amplitudes of the SC current density δ_{ilm} in the considered conductive materials of the current-carrying parts of the wires (cables) of the aircraft on-board network do not depend on the amplitude level I_{mk} of the steady-state emergency current with frequency of f=400 Hz in them.

The above numerical data for δ_{ilm} in the CCP of the on-board aircraft network (f=400 Hz) compared with similar numerical values from [1] of the maximum permissible current density amplitudes δ_{ilm} of the current $i_k(t)$ of SC characteristic for this case (J_{ill}≠0; t_{kC}=100 ms; I_{mk}=30 kA; T_a=20 ms) and the considered CCP of power circuits of electrical equipment of general industrial use (f=50 Hz), turn out to be approximately 3.9 times larger. To assess the effect of the duration t_{kC} of SC in the on-board power circuit of an aircraft on the choice of values of the maximum allowable cross-sections S_{il} of the studied wires and cables, Table 5 shows the data corresponding to the case t_{kC}=100 ms.

Table 5

Values of the maximum allowable cross-sections S_{il} for wires (cables) with copper (aluminum) cores (shells) in the on-board power circuits of the aircraft electrical equipment with current amplitude I_{mk} of single-phase SC current $i_k(t)$ from 3 to 30 kA (f=400 Hz; J_{ill}≠0; t_{kC}=100 ms; T_a=3 ms)

Type of insulation in the wire (cable) of the aircraft electrical equipment circuit	Core (shell) material of wire (cable)	Cross-section value S_{il}, mm^2			
		Amplitude I_{mk} of the steady-state SC current, kA			
		3	5	10	30
Without insulation	Copper	4.36	7.27	14.54	43.62
	Aluminum	7.73	12.89	25.77	77.32
PVC, R	Copper	5.86	9.78	19.55	58.66
	Aluminum	9.19	15.32	30.65	91.95
PET	Copper	7.09	11.81	23.62	70.88
	Aluminum	10.97	18.29	36.58	109.75

Note that the quantitative results for the sections S_{il} of the current-carrying parts of the CCP of the aircraft on-board network (f=400 Hz) presented in Table 5 were obtained according to (1), taking into account the data in Table 2, 3 for the mode when the equality T_a=3 ms is fulfilled in the on-board electrical circuits of an aircraft with active-inductive load, and АЗД3-200 circuit breakers (t_a=100 ms) are used as on-board protection devices on an aircraft against SC [13, 14]. From the data of Table 5, it follows that at t_{kC}=100 ms, regardless of the numerical value of the current amplitude I_{mk}, the maximum permissible density amplitudes $\delta_{ilm}\approx I_{mk}/S_{il}$ of the emergency current $i_k(t)$ at the SC for bare wires with copper and aluminum cores in the on-board electrical circuits of the aircraft electrical equipment (T_a=3 ms) are about 0.69 kA/ mm^2 and 0.39 kA/mm^2, respectively, for cables with copper (aluminum) cores (shells), PVC and R insulation – 0.51 (0.33) kA/mm^2, and for cables with copper (aluminum) cores (shells) and PET insulation – 0.42 (0.27) kA/mm^2. The results obtained for both S_{il} and δ_{ilm} (f=400 Hz; t_{kC}=100 ms) from the corresponding quantitative data for S_{il} and δ_{ilm} (f=50 Hz; t_{kC}=100 ms) from [1] differ (due to different values of parameter T_a, which in the first case was numerically 3 ms, and in the second case – 20 ms) by almost no more than 8%. Hence, it can be concluded that the choice in the on-board aircraft network of the maximum permissible cross-sections S_{il} of its CCP and, accordingly, the maximum permissible amplitudes of the current density δ_{ilm} in the current-carrying copper (aluminum) parts of its wires and cables is determined not by the frequency f of alternating current in the aircraft on-board network, but duration t_{kC} of emergency SC current $i_k(t)$ in the considered electric network emergency current.

Considering the above, in order to reduce the maximum allowable cross-sections S_{il} of the electrical wires (cables) used in the aircraft electrical equipment on-board electrical circuits and, accordingly, to ensure a decrease for aircrafts in the weight and size characteristics of their on-board CCP, it is necessary in the aircraft on-board networks along with the use of increased frequency of alternating current (for example, f=400 Hz) to use high-speed short-circuit protection devices having operation times t_a<<100 ms.

2.4. Calculation estimation of thermal resistibility of wires and cables in the on-board network of aircrafts. The proposed approach to the calculation of the maximum permissible cross-sections S_{il} of the wires (cables) in the on-board power circuits of the aircraft electrical equipment (f=400 Hz) allows the calculation of their thermal stability to be carried out. Here, as in [1, 8], it is proposed to determine the thermal resistibility of the investigated CCP in the aircraft on-board network by the following thermophysical condition:

$$\theta_{iS} \le \theta_{lS}, \quad (7)$$

where θ_{iS}, θ_{lS} are, respectively, the current (final) and maximum permissible short-term heating temperatures of the current-carrying parts of the electrical wires and cables in the aircraft on-board circuits.

To find in (7) the values of the current or final heating temperature θ_{iS} of the material of the current-carrying parts of the CCP, determined by the Joule heat on the action of the SC current $i_k(t)$, we initially use the well-known nonlinear dependence of the specific conductivity γ_i of the core (shell) material of the wire and cable on the value of the temperature θ_{iS} [1, 9]:

$$\gamma_i = \gamma_{0i}\left[1 + c_{0i}\beta_{0i}(\theta_{iS} - \theta_0)\right]^{-1}. \quad (8)$$

It is important to note that relation (8) in the temperature range from 20 °C to the melting temperature of the core (shell) materials of the CCP, according to experimental data from [9], approximates the temperature dependence of γ_i for copper and aluminum with an error of no more than 5%. Note that in (8), the quantity γ_{0i} is understood as the specific electrical conductivity γ_i of the conductive material of the current-carrying parts of the CCP at temperature θ_0=20 °C. Then, taking into account (8), the solution of the first-order inhomogeneous differential equation for the final temperature θ_{iS} of the Joule heating by current $i_k(t)$ of the single-phase SC of the material of the core (shell) of the CCP in the on-board power circuit of the aircraft electrical equipment under the initial condition of the form $[\theta_{iS}|_{(t=0)} - \theta_{0i}]$=0 can be written in the following approximate analytical form [1, 12]:

$$\theta_{iS} = \theta_{0i} + (c_{0i}\beta_{0i})^{-1}[\exp(J_{ak}\gamma_{0i}^{-1}\beta_{0i}/S_{il}^2) - 1], \quad (9)$$

where θ_{0i} is the initial temperature of the material of the current-carrying parts of the CCP, which, depending on the operating mode of the on-board electrical circuits of the electrical equipment, is θ_{ll} (J_{ill}≠0) or θ_0=20 °C (J_{ill}=0).

It can be seen from (9) that, under the assumptions made, the known numerical values of the thermophysical characteristics γ_{0i}, c_{0i} and β_{0i} for the conductive materials under consideration of the current-carrying parts of the CCP in the aircraft on-board network (see the data in Table 1), as well as for found by (1), (6) the numerical values of the maximum permissible cross-sections S_{il} of copper (aluminum) cores (shells) of wires (cables) and the action integral J_{ak} of the current $i_k(t)$ of a single-phase SC, the determination of the desired value of the final temperature θ_{iS} and its comparison by condition (7) with the known [8] permissible short-term temperature θ_{lS} does not cause any electrical engineering trouble.

As an example of the calculation estimation according to condition (7) of the thermal resistibility of the CCP of the aircraft on-board network (f=400 Hz; J_{ill}≠0; θ_{0i}=θ_{ll}=65 °C), we consider the case when for its aviation shielded wire of the БПВЛЭ brand with PVC insulation and the split copper core [7, 15] in the emergency mode of a single-phase SC, the following initial data are satisfied: I_{mk}=5 kA; t_{kC}=5 ms; T_a=3 ms. According to Table 4, for the indicated initial parameters, the maximum permissible cross-section S_{il} of the wire considered is numerically approximately 2.71 mm^2. In this case, the value of the action integral J_{ak} of the current $i_k(t)$ of a single-phase SC in the on-board network of an aircraft according to (6) will be numerically about $9.86\cdot10^4$ A^2·s (see Table 3). Then, according to (9), taking into account the data in Table 1, the final temperature θ_{iS} of the Joule heating by an emergency current $i_k(t)$ of the SC of the form (4) of the copper wire under consideration installed in the on-board network of the aircraft will be numerically equal to about 133.8 °C. It is seen that the calculated value of the final temperature θ_{iS}=133.8 °C is less than the maximum permissible short-term heating temperature θ_{lS} of the БПВЛЭ grade aviation copper wire with PVC insulation of 150 °C [8] checked for thermal resistibility. Therefore, we can conclude that condition (7) for this calculation case as applied to the on-board aircraft network is fulfilled.

In this regard, it can be said that the calculated assessment of the thermal resistibility of the БПВЛЭ brand aircraft wire with copper core and PVC insulation of the power circuits of the aircraft electrical equipment with alternating current frequency of f=400 Hz indicates the operability of the proposed electrical engineering approach to the calculation choice of permissible cross-sections S_{il} of current-carrying parts of the CCP used in on-board networks of various aircraft.

3. The influence of the frequency of the alternating current in the on-board network of the aircraft on the operation time of its protection device against short-circuit. We consider this question that has been little studied today in the field of applied electrical engineering by the example of the possible use of a short-circuit protection device (fuse) in the on-board network of an aircraft using not a metal flat plate that does not melt due to Joule heating by SC current (as in a conventional electric fuse [11, 16]), but an electrically exploding metal round wire [9, 12]. It is known that the operation time t_a of conventional fuses (for example, one of the world's best Ultra Quick series for current amplitudes of power frequency f=50 Hz up to 1.4 kA [17]) is at least 10 ms. It is possible to reduce these values of the operation time t_a of the protection device to units of milliseconds or fractions of a unit of a millisecond due to the use of high-speed fuses (HSFs) in the aircraft on-board network using the phenomenon of EE of the metal wire under the influence of emergency SC current of frequency f=400 Hz with amplitude I_{mk} of unity (tens) kiloamperes [9, 18].

We use the well-known analytical relationship that determines the time of the EE t_e in atmospheric air (operation time t_a of the HSF) of a round metal wire with cross-section S_i when emergency current $i_k(t)$ of SC flows through it in the on-board network of the aircraft [18]:

$$t_e = 1{,}333\cdot\left[J_c S_i^2/(2\pi^2 f^2 k_s^2 I_{mk}^2)\right]^{1/3}, \quad (10)$$

where J_c is the critical value of the current integral for a conductive material of an electrically exploding metal wire (for copper – J_c=1.95·10^{17} A^2·s·m^{-4} [9]; for aluminum – J_c=1.09·10^{17} A^2·s·m^{-4} [9]).

From (10) at f=400 Hz, k_S=1.66 (T_a=3 ms) and I_{mk}=30 kA for a round copper wire (J_c=1.95·10^{17} A^2·s·m^{-4}) with radius r_i=1 mm (S_i=3.141 mm^2) the value of the operation time t_a of the HSF under consideration (the time of the air EE t_e this wire) from exposure to it (this type of fuse) of AC SC current $i_k(t)$ in the on-board network of the aircraft is approximately 0.84 ms. As you can see, the EE of the indicated wire, which forms the basis of the HSF under consideration, occurs at the front of the first half-wave of the emergency current $i_k(t)$ (the maximum of this half-wave at f=400 Hz corresponds to the time t_m=1.25 ms), which occurs during a single-phase SC in the studied on-board network of the aircraft. We note that for I_{mk}=20 kA with the previous initial data indicated above, the operation time t_a of the HSF (the time of the EE t_e of the assumed round copper wire with cross-section S_i=3.141 mm^2) is equal to about 1.09 ms. From (10) it follows that the time of EE t_e of the metal wire in the on-board network of an aircraft with AC of frequency f is inversely proportional to the value of $(f)^{2/3}$. The higher the frequency f of the alternating current in the on-board network of the aircraft, the shorter the operation time t_a of the indicated HSF will be. The transition in the on-board network of an aircraft from frequency f=50 Hz of alternating current to its frequency f=400 Hz leads to a decrease in the operation time t_a of the HSF using the EE of a metal wire by four times.

Considering the revealed feature of the influence of the frequency f on the operation time t_a of the HSF under consideration, the use of increased alternating current frequency (for example, f=400 Hz) in the aircraft on-board network from the standpoint of the possibility of increasing the speed of its short-circuit protection device, the operation of which is based on the phenomenon of the EE of a metal wire is a technically justifiable offer.

Conclusions.

1. The proposed electrical engineering approach allows, under the condition of thermal resistibility of the CCP of the on-board power circuits of aircraft electrical equipment with alternating current of increased frequency f=400 Hz, to carry out the calculation choice of the maximum permissible cross-sections S_{il} of uninsulated wires, insulated wires and cables with copper (aluminum) cores (shells) with PVC, R and PET insulation, the current-carrying parts of which in the emergency mode of their operation can be affected by the current $i_k(t)$ of a single-phase short circuit in the on-board network of the aircraft with predicted and confirmed by many years of experience in operating various aircrafts amplitude-temporal parameters.

2. It is found that in the on-board power circuits of the aircraft electrical equipment (f=400 Hz; T_a=3 ms), the maximum permissible density amplitudes $\delta_{ilm}\approx I_{mk}/S_{il}$ of the current $i_k(t)$ of a single-phase short-circuit with its switch-off time t_{kC}=5 ms in the on-board electrical network of the aircraft regardless of the numerical value of the amplitude I_{mk} of the steady-state short-circuit current for uninsulated wires with copper (aluminum) cores, respectively, are about 2.48 (1.40) kA/mm^2, for wires and cables with copper (aluminum) cores (shells) and PVC (R) insulation – 1.85 (1.18) kA/mm^2, and for wires and cables with copper (aluminum) cores (shells) and PET insulation – 1.53 (0.99) kA/mm^2. With an increase in the on-board electrical network of the aircraft of the switch-off time t_{kC} of the current $i_k(t)$ of a single-phase short circuit in the indicated power circuits of the aircraft (T_a=3 ms), the maximum permissible density amplitudes δ_{ilm} of the emergency short circuit current also decrease and at t_{kC}=100 ms for uninsulated wires with copper (aluminum) cores are respectively approximately 0.69 (0.39) kA/mm^2, for wires and cables with copper (aluminum) cores (shells) and PVC (R) insulation – 0.51 (0.33) kA/mm^2, and for wires and cables with copper (aluminum) cores (shells) and PET insulation – 0.42 (0.27) kA/mm^2.

3. The decisive influence on the choice in the aircraft on-board network of the maximum permissible cross-sections S_{il} of its CCP and, accordingly, the maximum allowable current density amplitudes δ_{ilm} in the current-carrying copper (aluminum) parts of its wires and cables is exerted not by the frequency f of alternating current in the aircraft on-board network, but by the duration t_{kC} of the flowing (switch-off time) in the on-board electrical network of emergency short circuit current $i_k(t)$.

4. To reduce in the on-board power circuits of the aircraft electrical equipment the maximum allowable cross-sections S_{il} of used in them non- and insulated electric wires (cables) and, accordingly, to ensure the reduction in mass and size indicators of their on-board CCP for various aircraft, it is necessary along with the use of increased frequency f=400 Hz of alternating current to use high-speed short-circuit protection devices (circuit breakers) with their operation time t_a<<100 ms.

5. It is shown that the use of increased frequency f=400 Hz of alternating current in the on-board networks of aircrafts as compared with its frequency f=50 Hz leads to a significant increase (four times) in the speed of devices (fuses) for their protection against short-circuit, the operation of which is based on air EE of a round metal (in particular, copper) wire.

REFERENCES

1. Baranov M.I. Refined selection of allowable cross-sections of electrical conductors and cables in the power circuits of industrial electrical equipment taking into account emergency operating modes. *Electrical engineering & electromechanics*, 2019, no. 3, pp. 37-43. **doi: 10.20998/2074-272X.2019.3.06.**

2. Baranov M.I. A choice of critical sections of electric wires and cables in power circuits of electrical equipment of power industry. *Electrical engineering & electromechanics*, 2019, no. 5, pp. 35-39. **doi: 10.20998/2074-272X.2019.5.06**.

3. Barybin Yu.G. *Spravochnik po proektirovaniyu elekricheskih setey i oborudovanija* [Handbook per planning electrical circuit and equipment]. Moscow, Energoatomizdat Publ., 1991. 464 p. (Rus).

4. Knyazevskyi B.A., Lipkin B.Yu. *Elekrosnabzhenie promyschlennyh predpriyatij* [Electric supply industrial organization]. Moscow, High school Publ., 1972. 432 p. (Rus).

5. Available at: https://docplayer.ru/27377176-Lekciya-2-1-razdel-2-bortovaya-elektricheskaya-set-vozdushnogo-sudna-tema-2-1-elektricheskaya-provodka.html (accessed 23 May 2019). (Rus).

6. Available at: https://ru.wikipedia.org/wiki/Бортовая_система_электроснабжения_летательных_аппаратов (accessed 11 May 2019). (Rus).
7. Belorussov N.I., Saakjan A.E., Jakovleva A.I. *Elektricheskie kabeli, provoda i shnury. Spravochnik* [Electrical cables, wires and cords. Directory]. Moscow, Energoatomizdat Publ., 1988. 536 p. (Rus).
8. Orlov I.N. *Elektrotehnicheskij spravochnik. Proizvodstvo i raspredelenie elektricheskoj energii. Tom 3, Kn. 1* [Electrical engineering handbook. Production and distribution of electric energy. Vol. 3, Book 1. Ed. I.N. Orlov]. Moscow, Energoatomizdat Publ., 1988. 880 p. (Rus).
9. Knopfel' G. *Sverkhsil'nye impul'snye magnitnye polia* [Ultra strong pulsed magnetic fields]. Moscow, Mir Publ., 1972. 391 p. (Rus).
10. Baranov M.I. An anthology of the distinguished achievements in science and technique. Part 48: Aircraft designer Andrey Tupolev and his accomplishments in airplane design. *Electrical engineering & electromechanics*, 2019, no.2, pp. 3-8. **doi: 10.20998/2074-272X.2019.2.01.**
11. Khalyutin S.P. *Sistemy elektrosnabzheniya letatel'nyh apparatov* [Systems of electric supply of aircrafts]. Moscow, AFEA to the name of N.E. Zhukovskogo Publ., 2010. 428 p. (Rus).
12. Baranov M.I. *Izbrannye voprosy elektrofiziki. Monografiya v 3kh tomakh. Tom 3: Teorija i praktika elektrofizicheskih zadach* [Selected topics of Electrophysics. Monograph in 3 Vols. Vol. 3. Theory and practice of electrophysics tasks]. Kharkiv, Tochka Publ., 2014. 400 p. (Rus).
13. *Otraslevoy standart OST 1 00195-76. Apparaty zashchity bortovyh elektricheskih setey samoletov i vertoletov. Metodika vybora i proverki pravil'nosti ustanovki v sistemah elektrosnabzheniya* [Industry standard OST 1 00195-76. Vehicles of protection of side electric networks of airplanes and helicopters. Is there a method of choice and verification of rightness of setting in the systems of electric supply]. Moscow, National Standard of the USSR Publ., 1976. 167 p. (Rus).
14. Available at: https://files.stroyinf.ru/Index2/1/4293834/4293834330.htm (accessed 10 June 2019). (Rus).
15. Vlasov G.D. *Proektirovanie sistem elektrosnabzheniya letatel'nyh apparatov* [Planning of the systems of electric supply of aircrafts]. Moscow, Engineer Publ., 1967. 415 p. (Rus).
16. Available at: https://en.wikipedia.org/wiki/Fuse_(electrical) (accessed 10 June 2019).
17. Available at: https://www.compel.ru/lib/na/2014/3/2-klassika-navsegda-sovremennyie-plavkie-predohraniteli-i-derzhateli-razediniteli (accessed 20 July 2019). (Rus).
18. Baranov M.I., Lysenko V.O. The main characteristics of an electric explosion of a metallic conductor at high impulse currents. *Electricity*, 2013, no.4, pp.24-30. (Rus).

Received 29.05.2019

M.I. Baranov, *Doctor of Technical Science, Professor,*
Scientific-&-Research Planning-&-Design Institute «Molniya»,
National Technical University «Kharkiv Polytechnic Institute»,
47, Shevchenko Str., Kharkiv, 61013, Ukraine,
phone +380 57 7076841,
e-mail: baranovmi@kpi.kharkov.ua

How to cite this article:
Baranov M.I. A choice of acceptable sections of electric wires and cables in on-board circuits of aircraft electrical equipment. *Electrical engineering & electromechanics*, 2020, no.1, pp. 39-46. **doi: 10.20998/2074-272X.2020.1.06.**

UDC 621.319 **doi: 10.20998/2074-272X.2020.1.07**

G.V. Bezprozvannych, I.A. Kostiukov

ERROR OF CONTROL OF ELECTRICAL INSULATION STRUCTURES BY DIELECTRIC ABSORPTION PARAMETERS ACCORDING TO THE CONCEPT OF UNCERTAINTY OF MEASUREMENTS

Introduction. Measurements on alternating current of dielectric absorption parameters – capacitance and dielectric loss tangent tgδ allow us to evaluate the quality of insulation of cables, electrical machines, transformers, etc., both at the technological stage of manufacture and in operation. An increase in the reliability of the measurement result of the parameters is provided by a decrease in the measurement error due to the improvement of measuring instruments and measurement methods and an increase in the number of measurements Purpose. The estimation of the error of control of electrical insulation structures by dielectric absorption parameters in accordance with the concept of measurement uncertainty. Methodology. The error of measurements of the capacitance and the tangent of the dielectric loss angle is estimated using the example of a twisted unshielded pair of category 5e. A statistical analysis of the results of multiple measurements of the capacitance and the tangent of the dielectric loss angle of an unshielded cable is carried out. The linear regression equations for the measured values of the dielectric absorption parameters of the number of measurements are obtained. Practical value. Ensuring unity in the methods for estimating the error of measurement results, both when using the traditional concept of «measurement result error» and when introducing the concept of «measurement result uncertainty» into practice, it will allow to unambiguously interpret and correctly compare the results of measurements of the capacitance and tangent of the dielectric loss angle of electrical insulation structures. References 16, figures 3.

Key words: **dielectric absorption parameters, capacitance, dielectric loss tangent, multiple measurements, measurement error, standard uncertainty, expanded uncertainty, twisted pair, digital immittance meter.**

Представлено методологію оцінки похибки вимірювань параметрів діелектричної абсорбції електроізоляційних конструкцій в рамках концепції невизначеності вимірювань. Наведено статистичний аналіз результатів багаторазових вимірювань ємності і тангенса кута діелектричних втрат скручений пари неекранованого кабелю категорії 5е. Отримано рівняння лінійної регресії для виміряних значень параметрів діелектричної абсорбції від числа вимірів. Виконано оцінювання похибки вимірювань ємності і тангенса кута діелектричних втрат неекранованого кабелю. Бібл. 16, рис. 3.

Ключові слова: **параметри діелектричної абсорбції, ємність, тангенс кута діелектричних втрат, багаторазові вимірювання, похибка вимірювань, похибка вимірювань, стандартна невизначеність, розширена невизначеність, скручена пара, цифровий вимірювач імітансу.**

Представлена методология оценки погрешности измерений параметров диэлектрической абсорбции электроизоляционных конструкций в рамках концепции неопределенности измерений. Приведен статистический анализ результатов многократных измерений емкости и тангенса угла диэлектрических потерь витой пары неэкранированного кабеля категории 5е. Получены уравнения линейной регрессии для измеренных значений параметров диэлектрической абсорбции от числа измерений. Выполнено оценивание погрешности измерений емкости и тангенса угла диэлектрических потерь неэкранированного кабеля. Библ. 16, рис. 3.

Ключевые слова: **параметры диэлектрической абсорбции, емкость, тангенс угла диэлектрических потерь, многократные измерения, погрешность измерений, погрешность измерений, стандартная неопределенность, расширенная неопределенность, витая пара, цифровой измеритель иммитанса.**

Introduction. Measurements on alternating current of dielectric absorption parameters – the capacitance C and dielectric loss tangent $tg\delta$ allow us to evaluate the quality of insulation of cables, electrical machines, transformers, etc., both at the technological stage of manufacture and in operation [1-4].

When presenting the results of measuring the dielectric absorption parameters, a certain quantitative characteristic of the quality of the obtained measurement result should be presented for the possibility of: assessing its reliability; comparisons with the values specified in the technical documentation, standards; comparisons with results obtained by other authors.

The increase in the reliability of the measurement result of the parameters is provided by reduction of error of measurements due to the improvement of measuring instruments and measurement methods and by increasing the number of measurements themselves [5-9].

Problem definition. When conducting multiple measurements, the procedure for estimating measurement errors is defined in [10-12]. Processing the observation results includes the following procedures:

1. Exclusion of known systematic errors from the observation results.
2. Calculation of the arithmetic mean value of the observation results, taken as the measurement result.
3. Calculation of the standard deviation of the observation result.
4. Identification and exclusion of results containing misses.
5. Calculation of the standard deviation of the measurement results.
6. Testing the hypothesis that the measurement results belong to the normal distribution law (for the number of measurements $n<10$, the hypothesis is not tested).

7. Calculation of the random component of the error of the measurement result, taking into account the Student coefficient, depending on the accepted confidence probability P and the number of observation results (P = 0.95 at technical measurements).

8. Calculation of the non-excluded systematic error of the measurement result (the limits of the allowed basic and additional errors of measuring instruments, as well as methodological errors and errors caused by other sources) [10-12].

By its definition, the error of the measurement result represents the deviation of the measurement result from the *true* (*actual*) value of the measured quantity, which is unknown in practice when measuring [10-12].

The concept of measurement uncertainty does not use the concepts of the true and actual values of the measured quantity. The result is considered reality, since the value of the true measurement is unknown [11-13].

The concept of uncertainty is the only internationally recognized measure of error assessment. Measurement uncertainty is considered as incomplete knowledge of the value of the measured quantity. To quantify this incompleteness, a probability distribution of the possible values of the measured quantity is introduced. The parameter of this distribution, called uncertainty, quantitatively characterizes the error of the measurement result [13].

Uncertainty can be expressed as standard deviation (standard uncertainty) or interval (extended uncertainty) and calculated by method A (based on a number of experimental data) or by method B (based on additional information) [13].

Uncertainty is a quantitative measure of how reliable an assessment of the measured quantity is the result obtained. Uncertainty does not mean doubt about the result, but, on the contrary, uncertainty implies an increase in the degree of reliability of the result.

Assessment of the measurement result and its uncertainty is carried out in the following sequence: drawing up the measurement equation; assessment of input quantities and their standard deviations (uncertainties); assessment of the measured (output) value and its uncertainty; budgeting for uncertainty; assessment of the extended uncertainty of the measurement result; representation of the measurement result [13].

Extended uncertainty is interpreted as an interval containing a given fraction of the distribution of values that could reasonably be attributed to the measured quantity. Extended uncertainty in the concept of uncertainty does not play the role that is assigned in the concept of error. It is believed that the main result of the assessment is the total uncertainty u_C, and the expanded uncertainty differs from it by a constant coefficient, which is necessary in a number of special cases to show the reliability of the estimate. This coefficient can take values from 2 to 3 with a confidence level from 0.95 to 0.99.

The goal of the paper is to evaluate the error of the control of electrical insulating structures according to the dielectric absorption parameters in accordance with the concept of measurement uncertainty.

Methodology for assessing the error of measuring capacitance and dielectric loss tangent. Inspections of electrical insulation structures in stationary laboratory conditions allow repeated observation of the measured dielectric absorption parameters. The results of repeated measurements of parameters even in stationary conditions differ from one another because the effect of many random interferences.

The standard ways to reduce the influence of random interferences is to calculate the average value and variance s of the measured parameters [7-8, 14].

The main difference in the concepts (of uncertainty and of error) is in what value the variance (standard deviation) is attributed: to the actual value of the measured quantity or to the measurement result.

The initial data for estimating the standard measurement uncertainty are the results of multiple measurements (N) of the capacitance C_i and the dielectric loss tangent $\mathrm{tg}\delta_i$. Based on the results obtained, arithmetic means $\overline{C_i}$, $\overline{\mathrm{tg}\delta_i}$ are calculated which are an estimate of the capacitance and the dielectric loss tangent.

Here, for the electric capacitance, the average value

$$\bar{C}_i = \frac{1}{N}\sum_{i=1}^{N} C_i \,. \qquad (1)$$

The standard uncertainty associated with the estimate of $\overline{C}$ is the experimental standard deviation of the mean value and is equal to the positive square root of the experimental variance of the mean value.

Standard uncertainty of measurement $u(C_i)$ according to method A

$$u(C_i) = u_A(C_i) = \sqrt{\frac{1}{N(N-1)}\sum_{i=1}^{N}\left(C_i - \overline{C_i}\right)^2} \qquad (2)$$

for the measurement result of $C_i = \overline{C_i}$ calculated as the arithmetic mean.

In calculating the standard uncertainty in accordance with (2), N independent random values of the form C_i and one value $\overline{C_i}$ depending on them are used. Therefore, the number of degrees of freedom associated with (1) is $k = N - 1$.

The sum of the squares in (2) refers to one degree of freedom, therefore, in the denominator of (2) there is the number $N - 1$.

With an increase in the number of measurements, the arithmetic mean $\overline{C_i}$ tends to the true value of $\overline{C_i}$, provided that all systematic errors are eliminated. In this case, the difference between the error and ($C_i - \overline{C_i}$) will tend to zero. Then the mathematical patterns of behavior of the aggregates of error and $u(C_i)$ will be similar.

When calculating the average, a series of random values of the capacitance C_i (the tangent of the dielectric loss angle) are summed up as the results of individual observations. Each of the results C_i can be represented as the sum of the mathematical expectation $\overline{C}$ and the random additive error e distributed according to the normal law with zero mathematical expectation [14]

$$C_i = \overline{C} + e \,. \qquad (3)$$

When summing N random values of the form (3), the mathematical expectation of the term $\overline{C}$ increases by

N times, and of the random one (e) only by a factor of $\sqrt{N}$. In other words, $\overline{C}$ amplifies, and random e decreases. As a result, the average is less prone to fluctuations than the result of a single observation of C_i. The variance of the mean $s_{\overline{C}}^2$ is N times smaller than the variance of a single observation s^2 [6, 14]

$$s_{\overline{C}}^2 = \frac{s^2}{N}. \quad (4)$$

The accumulation of the results of N measurements and the calculation of the average lead to a decrease in the width of the confidence interval by almost a factor of $\sqrt{N}$

$$\widetilde{C} - t(k,p)\frac{s}{\sqrt{N}} \le \overline{C} \le \widetilde{C} + t(k,p)\frac{s}{\sqrt{N}}, \quad (5)$$

where $t(k, p)$ is the Student criterion selected with a confidence probability of P (usually P = 0.95) for the number of degrees of freedom k.

For example, at N = 100, the width of the uncertainty interval decreases by 10 times. When using, for example, a digital immitance meter E7-14, an additional significant figure appears, indicating a decrease in the error of the measurement result [5].

Statistical analysis of the results of multiple measurements of dielectric absorption parameters. Testing the methodology for assessing the error of measuring the capacitance and the tangent of the dielectric loss angle in the concept of the uncertainty of measurements of electrical insulating structures is performed using an example of twisted unshielded pair of category 5e [15, 16]. The cable length is 100 m. The capacitance and the dielectric loss tangent are measured at frequency of 120 Hz for 1 hour using a RLC E7-22 digital immittance meter under constant ambient air conditions under laboratory conditions. In real time, with a resolution of 1 s, the results of measurements using the standard RS-232 electrical interface are recorded in computer memory using software. The error of the meter is 0.7 %.

Figure 1 shows a 3D diagram of the temporal series of the electric capacitance and the dielectric loss tangent of a twisted unshielded pair of category.

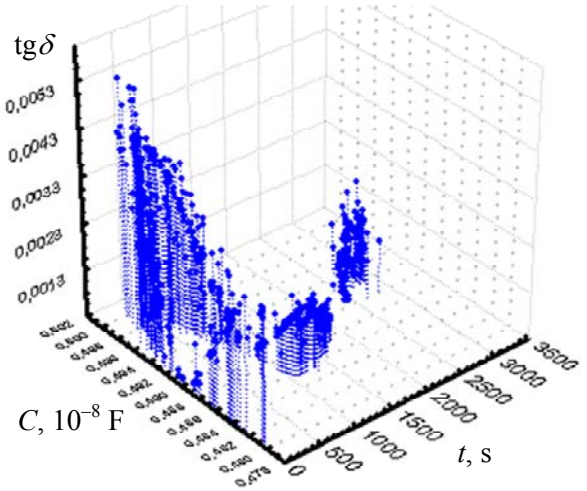

Fig. 1. Temporal series of dielectric absorption parameters of the twisted unshielded pair

The dynamics of the time variation of the capacitance (Fig. 2,*a*) and the dielectric loss tangent (Fig. 2,*b*) are almost identical. But the difference in time dependences and the wider spread of tgδ values are due to the physical nature of the dielectric loss tangent. This parameter reflects not only polarization losses, but also electrical conductivity loses. The straight line in the Figures shows the regression line of the parameter values depending on the number of measurements N. The linear regression equations for the measured values of the dielectric absorption parameters on the number of measurements N have the form

$$C = (0{,}4923 - 9{,}5794 \cdot 10^{-7} N) \cdot 10^{-8}, F \quad (6)$$

$$\mathrm{tg}\delta = 0{,}0027 - 8{,}5081 \cdot 10^{-7} N. \quad (7)$$

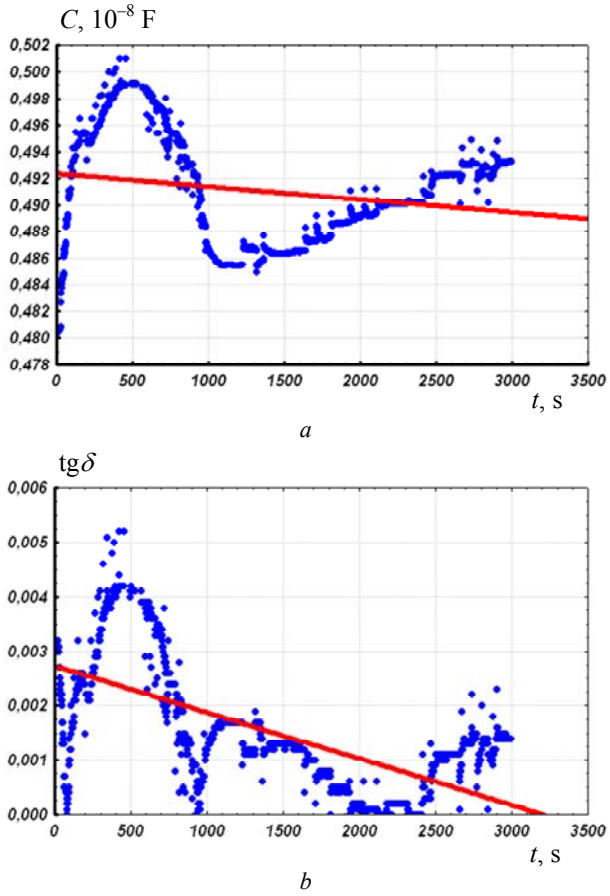

Fig. 2. Results of multiple measurements with a resolution of 1 s of the electrical capacitance and the tangent of the dielectric loss angle of a twisted pair

The average value of the capacitance is $0.4909 \cdot 10^{-8}$ F; the standard deviation is $0.00406 \cdot 10^{-8}$ F; the maximum value is $0.501 \cdot 10^{-8}$ F; the minimum value is $0.4803 \cdot 10^{-8}$ F (Fig. 3,*a*). The average value of the dielectric loss tangent is 0.001433; the standard deviation is 0.001128; the maximum value is 0.052; the minimum value is 0, which may be due to insufficient sensitivity of the digital meter (Fig. 3,*b*).

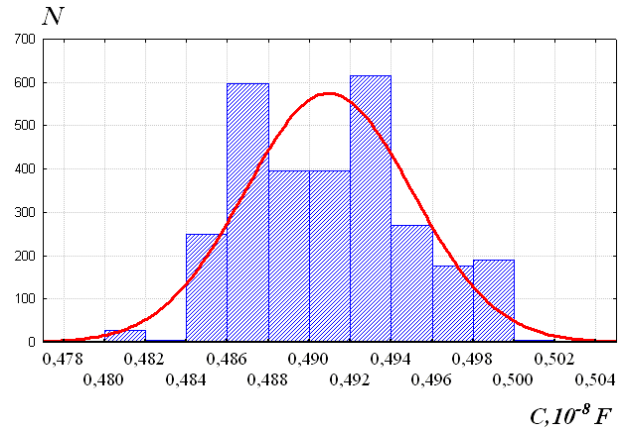

a

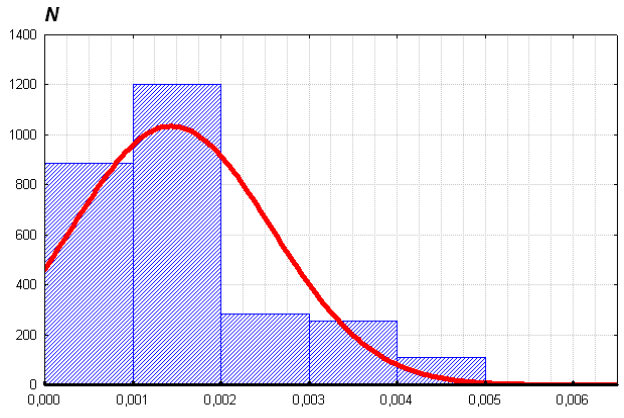

b

Fig. 3. Histogram of the observation results under the assumption of a normal distribution law of the measured dielectric absorption parameters

Assessment of error of measurements of capacitance and dielectric loss tangent. The calculated standard measurement uncertainty of type A, due to random sources of uncertainty having random nature, in accordance with (2) is $u(C_i) = 7.5007 \cdot 10^{-13}$ F or 0.00153 % for the capacitance; $u(\text{tg}\delta_i) = 2.0771 \cdot 10^{-5}$ or 1.45 % for the dielectric loss tangent.

The standard measurement uncertainty of type B for systematic uncertainty sources, i.e. the instrument error is $1.9827 \cdot 10^{-11}$ F or 0.4 % for the capacitance and $5.7983 \cdot 10^{-6}$ or 0.4 % for the dielectric loss tangent, respectively.

The total standard uncertainty: $1.9841 \cdot 10^{-11}$ F or 0.4 % for the capacitance and $2.1565 \cdot 10^{-11}$ or 1.5 % for the dielectric loss tangent, respectively.

The expanded uncertainty of the measurement results with a digital immitance meter E7-22 is for a capacity 0.8 %; for the dielectric loss tangent 3 %, respectively, for the confidence probability (probability of coverage) $P = 0.95$ and the coverage coefficient $k = 2$.

Conclusions.

A methodology for assessing the error of measurements of dielectric absorption parameters of electrical insulation structures within the framework of the concept of measurement uncertainty is presented.

Testing the methodology for assessing the error of control of electrical insulating structures in terms of the capacitance and the dielectric loss tangent in the concept of measurement uncertainty is carried out on the example of a twisted unshielded pair of category 5e.

A statistical analysis of the results of multiple measurements of the capacitance and the tangent of the dielectric loss angle of an unshielded cable is carried out. The linear regression equations for the measured values of the dielectric absorption parameters on the number of measurements are obtained.

The error of measuring the capacitance and the tangent of the dielectric loss angle of an unshielded cable has been evaluated. The standard measurement uncertainty of type A is 0.00153 % for the capacitance and 1.45 % for the dielectric loss tangent. The expanded uncertainty of the measurement results with an E7-22 digital immitance meter for the confidence probability (probability of coverage) $P = 0.95$ and the coverage coefficient $k = 2$ is 0.8 % and 3 % for the capacitance and the dielectric loss tangent, respectively.

Ensuring unity in the methods for assessing the error of measurement results, both when using the traditional concept of «*measurement result error*» and when introducing the concept of «*measurement result uncertainty*» into practice, will allow to unambiguously interpret and correctly compare the results of measurements of the capacitance and the tangent of the dielectric loss angle of electrical insulation structures.

REFERENCES

1. Liu T., Fothergill J., Dodd S., Nilsson U. Dielectric spectroscopy measurements on very low loss cross-linked polyethylene power cables. *Journal of Physics: Conference Series*, 2009, vol.183, p. 012002. **doi: 10.1088/1742-6596/183/1/012002.**

2. Setayeshmehr A., Fofana I., Eichler C., Akbari A., Borsi H., Gockenbach E. Dielectric spectroscopic measurements on transformer oil-paper insulation under controlled laboratory conditions. *IEEE Transactions on Dielectrics and Electrical Insulation*, 2008, vol.15, no.4, pp. 1100-1111. **doi: 10.1109/tdei.2008.4591233.**

3. Gavrilă Doina Elena. Dielectric Spectroscopy, a Modern Method for Microstructural Characterization of Materials. *Journal of Materials Science and Engineering A*, 2014, no.1, pp. 18-26. **doi: 10.17265/2161-6213/2014.01.003.**

4. Bezprozvannych G.V., Roginskiy A.V. Dielectric spectroscopy of casing thermosetting composite electrical insulation system of induction traction electric machines. *Electrical engineering & electromechanics*, 2018, no.1, pp. 17-20. **doi: 10.20998/2074-272X.2018.1.02.**

5. Bezprozvannych G.V., Naboka B.G. Influence of parasitic capacitance on the results of measurements of parameters of multicore cables in assessing their technical condition. *Electricity*, 2011, no.5, pp. 27-36. (Rus).

6. Bezprozvannych G.V., Boyko A.M. Electrostatic processes in power cables. *Electrical engineering & electromechanics*, 2013, no.4, pp. 27-31. (Ukr).

7. Hart H. *Vvedenie v izmeritel'nuiu tekhniku* [Introduction to Measurement Technology]. Moscow, Mir Publ., 1999. 391 p. (Rus).

8. Markov N.S. *Osnovy teorii obrabotki rezul'tatov izmerenii* [Fundamentals of the theory of processing measurement results]. Moscow, Standards Publishing House, 1991. 176 p. (Rus).

9. *DSTU 4743: 2007. Provody samoutrymni izolovani ta zakhyshcheni dlia povitrianykh linii elektroperedavannia. Zahalni tekhnichni umovy* [State Standard of Ukraine DSTU

4743: 2007. Wires self-supporting insulated and protected for overhead transmission lines. General specifications]. Kyiv, 2007. 26 p. (Ukr).
10. *DSTU ISO 10012:2005 Systemy keruvannia vymiriuvanniam. Vymohy do protsesiv vymiriuvannia ta vymiriuvalnoho obladnannia* [State Standard of Ukraine DSTU ISO 10012. Measurement management systems requirements for measurement processes and measuring equipment]. (Ukr).
11. Mironov E.G., Firsanov V.A. Errors and measurement uncertainties. *Instrumentation Practice*, 2004, no.2, pp. 79-84. (Rus).
12. Kuznetsov V.P. Error of Measurement and Uncertainty: A Comparison. *Measurement Techniques*, 2003, vol.46, iss.8, pp. 751-760. **doi: 10.1023/a:1026157229045**.
13. *JCGM 100:2008. Evaluation of measurement data. Guide to the expression of uncertainty in measurement*. Available at: http://www.bipm.org/ utils/common/documents/jcgm (accessed 17 June 2018).
14. Goltsman F.M. *Fizicheskii eksperiment i statisticheskie vyvody* [Physical experiment and statistical conclusions]. Leningrad, Leningrad University Publ., 1982. 192 p. (Rus).
15. Boyko A.N. Drift in time capacity and dielectric loss tangent of unshielded and shielded network cables. *Bulletin of NTU «KhPI»*, 2013, no.42, pp. 65-68. (Rus).
16. Bezprozvannych G.V., Boyko A.M. Experimental determination of triboelectric potential in unshielded and shielded network cables. *Electrical engineering & electromechanics*, 2012, no.3, pp. 56-60 (Ukr).

Received 12.11.2019

G.V. Bezprozvannych[1]*, Doctor of Technical Science, Professor,*
I.A. Kostiukov[1]*, Candidate of Technical Science,*
[1] National Technical University «Kharkiv Polytechnic Institute»,
2, Kyrpychova Str., Kharkiv, 61002, Ukraine,
phone +380 57 7076010,
e-mail: bezprozvannych@kpi.kharkov.ua,
iakostiukow@gmail.com

How to cite this article:
Bezprozvannych G.V., Kostiukov I.A. Error of control of electrical insulation structures by dielectric absorption parameters according to the concept of uncertainty of measurements. *Electrical engineering & electromechanics*, 2020, no.1, pp. 47-51. **doi: 10.20998/2074-272X.2020.1.07.**

UDC 621.316.99 **doi: 10.20998/2074-272X.2020.1.08**

D.G. Koliushko, S.S. Rudenko, L.V. Asmolova, T.I. Tkachova

DETERMINATION OF THE SOIL SOUNDING DEPTH FOR THE EARTHING RESISTANCE CALCULATION OF SUBSTATIONS 35 KV

Purpose. ***Determination of the minimum required sounding depth for calculation of the earthing resistance for substations with a voltage class of 35 kV.*** ***Methodology.*** ***For each ratio of electrical resistivity values of soil layers, earthing resistance was calculated with changing of the layers separation depth from 0.4 m to h_{max}, where h_{max} is the layers separation depth in a two-layer soil at which the earthing resistance value becomes the same as in a uniform soil.*** ***Results.*** ***In the experiments carried out, a family of curves was obtained that describes the effect of separation depth of soil layers for various combinations of soil electrical resistivities and geometric dimensions of the earthing arrangement. The accumulated statistical data for substations with a voltage class of 35 kV made it possible to determine the required sounding depth depending on the maximum size of the earthing arrangement and the probability of the relative resistivity falling into the corresponding range of values. An algorithm is proposed for determining the required investigation depth by Wenner method as part of the electromagnetic diagnostics of the earthing arrangement of existing substations with a voltage class of 35 kV.*** ***Originality.*** ***For the first time, a probabilistic relationship was established between the ratio of the electrical resistivity of soil layers, the size of the earthing arrangement, and the necessary depth investigation of the geological medium. As a result it has been proven that there are substations for which the required sounding depth does not exceed the maximum size of the earthing arrangement.*** ***Practical value.*** ***The use of the algorithm developed in this work allows increasing the accuracy of the earthing resistance calculation of electrical installations with voltages above 1 kV operating in a network with isolated neutral.*** References 9, figures 4.

Key words: **earthing arrangement, earthing resistance, the soil sounding, Wenner installation, electromagnetic diagnostics.**

Метою роботи є підвищення точності визначення опору заземлювального пристрою електроустановок напругою понад 1 кВ, що працюють в мережі з ізольованою нейтраллю. Для цього було проаналізовано величину необхідної глибини зондування ґрунту у процесі виконання електромагнітної діагностики стану заземлювального пристрою. Були проведені чисельні експерименти, які полягали у розрахунку електричних параметрів заземлювача, виконаного у вигляді прямокутника розмірами a × b з діагоналлю D і розташованого на глибині 0,3 м у двошаровому ґрунті. Було розглянуто різні варіанти співвідношення питомих електричних опорів ґрунту та розмірів заземлювального пристрою. Врахування статистичного розподілу вказаних параметрів для понад 500 підстанцій України класом напруги 35 кВ дозволило встановити двофакторну ймовірнісну залежність мінімально необхідної глибини зондування ґрунту установкою Веннера. Бібл. 9, рис. 4.

Ключові слова: **заземлювальний пристрій, опір заземлювального пристрою, зондування ґрунту, установка Веннера електромагнітна діагностика.**

Целью работы является повышение точности определения сопротивления заземляющего устройства электроустановок напряжением выше 1 кВ, работающих в сети с изолированной нейтралью. Для этого была проанализирована величина необходимой глубины зондирования грунта в процессе выполнения электромагнитной диагностики состояния заземляющего устройства. Были проведены расчетные эксперименты, которые заключались в нахождении электрических параметров заземления, выполненного в виде прямоугольника размерами a × b с диагональю D и расположенного на глубине 0,3 м в двухслойном грунте. При этом были рассмотрены различные варианты соотношения удельных электрических сопротивлений грунта и размеров заземляющего устройства. Учет статистического распределения указанных параметров для более 500 подстанций Украины классом напряжения 35 кВ, позволил установить двухфакторную вероятностную зависимость минимально необходимой глубины зондирования грунта установкой Веннера. Библ. 9, рис. 4.

Ключевые слова: **заземляющее устройство, сопротивление заземляющего устройства, зондирование грунта, установка Веннера, электромагнитная диагностика.**

Problem definition. To ensure reliable and safe operation of energy objects in the case of a short circuit [1] or direct lightning strike [2], an earthing arrangement made in accordance with regulatory requirements is used. For electrical installations exceeding 1 kV operating in a network with isolated neutral (substations of 35 kV voltage class and below), the only electrical parameter that allows to estimate the condition of the earthing arrangement (EA) is its resistance (R_{EA}) [1]. According to [3], the value of the R_{EA} should be periodically monitored and determined at least every 12 years. The measurement of the resistance of the EA, as a rule, is performed by the method of ammeter-voltmeter using a single-beam or two-beam circuit. Here, it is necessary to install measuring electrodes in the zone of zero potential, the distance to which, as a rule, several times exceeds the largest size of the EA [4].

For 35 kV substations, which are located in dense urban or industrial development with a branched communication system, this is practically impossible. Therefore, the only way to determine the resistance of the EA of such energy objects is to calculate it using special software systems. Therefore, improving the accuracy of R_{EA} calculation is an urgent task in terms of electrical safety and reliability of electrical installations exceeding 1 kV with isolated neutral.

Initial data for the calculation of the resistance of the EA are a real diagram of design with indication of the depth of arrangement of the elements of the EA, the cross-section of earthers and electrophysical characteristics (EPC) of the soil (number of soil layers, their specific electrical resistance (SER) and thickness) [5].

Constructive execution of the EA of objects, which are in operation for a long time, is determined by the induction method when conducting the electromagnetic diagnostics of the state of the EA [4], the cross-section of the earthers is measured at a selective opening of the soil, and EPC of the soil according to the results of vertical electrical sounding (VES) near the substation. The soil EPC ratio (SER of the first layer ρ_1 and of the second layer ρ_1, as well as the thickness of the first layer h_1) and the geometric dimensions of the EA actually determine the required sounding depth and the technical parameters of the device for conducting the VES [6]. The authors from 1999 to 2019 conducted electromagnetic diagnostics of the state of over 500 substations of a 35 kV class voltage, which are located in all regions of Ukraine, so the accumulated statistics allow us to determine the characteristic sizes of substations' EAs and the limits of soil EPC values.

As the literature analysis in [7] shows, there is no clear relationship between the size of the EA and the required depth of sounding. Depth of sounding (H_{VES}) has been determined by Kostruba S.I. as early as 1983, as the dependence of the distance between the current electrodes from the square root of the EA area, only for the Burgsdorf installation, however, there is no similar or any other dependence was given for other VES installations (in particular, for the most common Venner installation) [6].

In [6, 8, 9] some data from the study of the required depth of sounding, obtained in the study of the dependence of the resistance of the EA on its area are given. From the analysis of the mentioned works, the following conclusion is reached: if the value of SER decreases with increasing depth, then it is necessary to determine the soil structure to a depth of at least $1.5\cdot\sqrt{S}$, and with increasing – several (3–5) $\sqrt{S}$. Thus, there is no clear dependence of the required sounding depth on the size of the EA and the soil EPC in the works on the VES for the purpose of designing or diagnostics of EA.

The goal of the work is the determination of the minimum required depth of sounding soil for the calculation of the resistance of the substations' EAs with a voltage class of 35 kV.

Research materials. The EA size, as indicated above, determines the required sounding depth H_{VES} when conducting the diagnostics of the EA condition, so it is suggested to find it in the form of the product of the largest geometric size of the EA (diagonal) D and the sounding coefficient K_{VES}:

$$H_{VES} = K_{VES}D. \quad (1)$$

Thus, the problem is actually reduced to determining the K_{VES} coefficient, which depends on the corresponding diagonal size of the EA and the soil EPC.

To solve this problem it is necessary to analyze the influence of each of the factors within their values. To determine the effect of the size of the EA, we use the results obtained during the diagnostics of the state of the substations' EAs of the voltage class 35 kV, represented as the probability density of the maximum size D [5].

From the analysis of Fig. 1 it follows that the value of the largest diagonal lies in the range from 10 m to 300 m, taking into account the substations at which the study was not conducted.

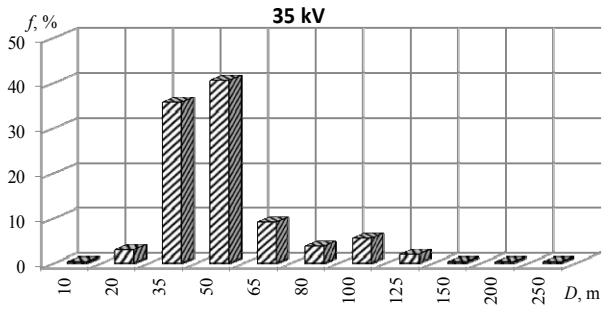

Fig. 1. Probability density of the size D of the EA

Different soil SER ratios ρ_2/ρ_1 were also systematized: Fig. 2 shows the probability density of the relative SER value ρ^* which was determined by the results of the VES in the framework of electromagnetic diagnostics of the EA of the studied substations in all regions of Ukraine.

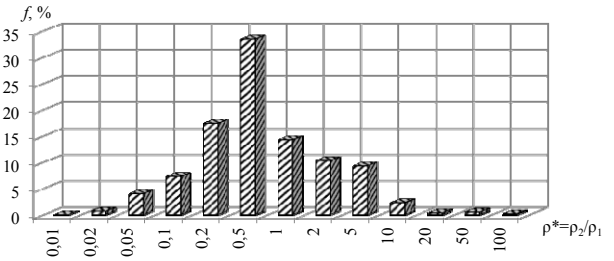

Fig.2. Probability density of the relative SER

According to the results obtained, it is advisable to consider ρ^* in the range [0.05; 10] which allows to cover 99 % of Ukraine's soils in the locations of existing substations.

Numerical experiments were carried out to determine H_{VES} which consisted of calculating the resistivity of the EA (R_{EA}), made in the shape of a square $a \times a$ of diagonal D and located at a depth of 0.3 m in two-layer soil. There are no internal cells in the EA as their effect on R_{EA} is insignificant and does not exceed 10 % [6]. The required sounding depth was determined by the relative resistance of the EA based on the study of the effect on its of the depth of layer separation h. For each ρ^*, the value of R_{EA} was calculated when the h/D ratio varied from 0.4 m to h_{max}, where h_{max} is the depth of layer separation in a two-layer soil, at which the resistance of the EA becomes equal to the resistance of the EA in a homogeneous soil ($R_{EA} = R_{EAUNI}$). In this case, the value of ρ_1 varied for the variation ρ^*, and the base ρ_2 was 1000 Ω·m which allows to cover all the ratios ρ_2/ρ_1 [5].

In the course of the experiments, a family of curves was obtained describing the effect of h for different combinations of soil EPC and the geometric parameters of the EA $R^*_{EA} = f(h / D)$, where $R^*_{EA} = R_{EA} / R_{EAUNI}$. The results of calculations for the EA, which is made in the shape of a square with side a = [10; 40; 100; 200] m and diagonal D = [14; 56.6; 141; 282] m respectively, are shown in the graphs of Fig. 3.

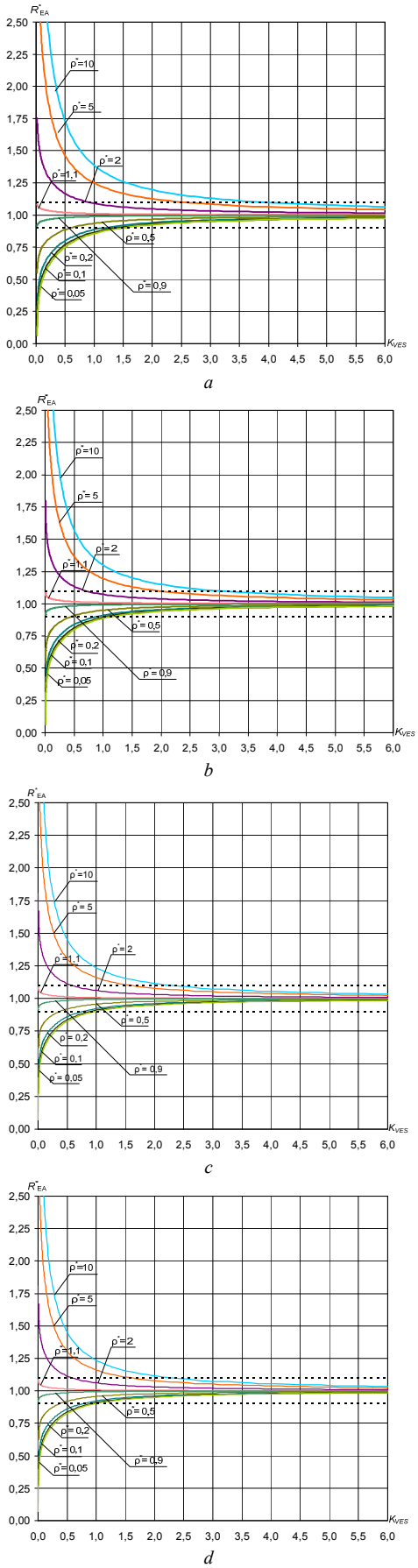

Fig. 3. Dependencies of the relative resistance on the coefficient of the depth of sounding:
a – a = 10 m, D = 14 m; *b* – a = 40 m, D = 56.6 m;
c – a = 100 m, D = 141 m; *d* – a = 200 m, D = 282 m

The graphs indicate the 10 % deviation by the dotted line. As it can be seen, for the EA with a diagonal of 14 m to calculate with an error of not more than 10 % it is necessary to sound the soil to a depth of not less than 4 D, and for the EA with a diagonal of 56 m – 3 D. Considering the individual ranges of values of ρ^*, we can state that at placement of ρ^* in the range [0.05; 2] (corresponding to 95 % of the substations studied in Ukraine) sounding depth is 1.5·D for 14 m and 1.0·D for 56 m. That is, for example, reducing the probability of ρ^* falling into the p_{EA} range from 0.99 to 0.95, it is possible to significantly reduce (by three times) the calculated value of the required sounding depth for the same substation (D = 56 m) from $H_{VES} = 3D$ to $H_{VES} = D$. This significantly reduces the labor costs of performing the VES while maintaining the accuracy of the calculations.

The possibility of reduction of probability is determined based on prior information about the structure of the soil in the relevant geographical area (for example, it is unacceptable for mountainous terrain where it is known that the resistance of the lower layers of rocks will be an order of magnitude greater than the resistance of the upper sedimentary rocks, i.e. $\rho^* \geq 10$).

In general, the dependence of the resistance of the EA on its geometric dimensions is nonlinear in nature, and with a conditional infinite increase in the size of the EA the value of the resistance is included in the "saturation" [6, 9]. The analogy with the dependence of the K_{VES} coefficient on the diagonal of the EA, which in turn determines the required sounding depth, seems logical. Taking into account the graphs presented (see Fig. 3), the $K_{VES}(D)$ function was obtained for the studied ranges of values with a given probability (see Fig. 4):

- $\rho^* \in [0.05; 10]$, which corresponds to the probability of falling into the range $p_{EA} = 0.99$;
- $\rho^* \in [0.05; 5]$, which corresponds to $p_{EA} = 0.98$;
- $\rho^* \in [0.05; 2]$, which corresponds to $p_{EA} = 0.95$.

The obtained graphs allow to determine the required sounding depth, depending on the maximum size of the EA and the probability of falling ρ^* in the range according to expression (1).

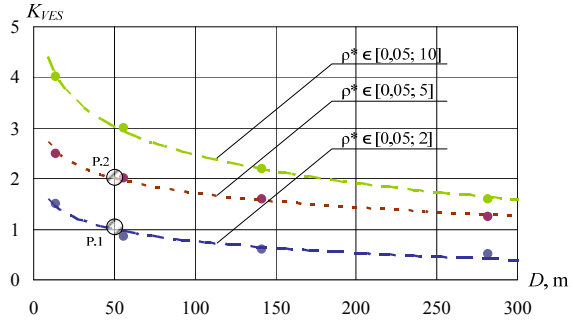

Fig. 4. Dependence of the sounding coefficient on the size of the EA

In addition, the analysis of the obtained data shows that there are such soil ratios and sizes of EAs for which the sounding depth required does not exceed the maximum size of the EA (D): these are substations at those EAs $D \geq 50$ m (according to Fig. 1 their 61 %) for $p_{EA} = 0.95$.

Taking into account the statistics (see Fig. 1, 2), the probability of finding such a substation p_{LD} is:

$$p_{LD} = 61\ \%\cdot 0.95/100\ \% = 0.58.$$

Taking into account the above, the following algorithm of determination of H_{VES} is proposed when conducting VES in the framework of electromagnetic diagnostics of the state of the EAs of operating substations of 35 kV class (provided there is no prior information about the soil structure):

1) to determine the maximum size of the EA using the induction method (for example, D = 50 m);

2) to consider that the soil has a relative SER value in the range $\rho^* \in [0.05; 2]$ (see P.1 in Fig. 4: $K_{VES} = 1$, hence $H_{VES} = D$);

3) the soil is sounded by means of the Wenner installation [3-5] at a maximum inter-electrode distance equal to D;

4) approximate interpretation of VES results is performed;

5) depending on the obtained value of SER in item 4 the following options are possible:

- if $0.05 \le \rho^* \le 2$, then we believe that the sounding depth is sufficient;
- if $2 < \rho^* \le 5$ or $\rho^* > 5$, then to determine the required sounding depth according to the corresponding curve of Fig. 5 and expression (1), to increase the inter-electrode distance and to carry out additional measurements (for example, if $\rho^* = 4.5$, then the required sounding depth has increased to $2D$ – see P.2 in Fig. 4);

6) if necessary, the results of the VES are re-interpreted and the value of ρ^* obtained is evaluated.

Conclusions.

1. On the basis of the analysis of statistical data on the results of electromagnetic diagnostics of substations with a voltage of 35 kV, the probabilistic dependence of the required depth of sounding on the ratio of specific resistances of the soil and the size of the EA was determined.

2. It is found that there are soil ratios and sizes of the EAs for which the required depth of sounding does not exceed the maximum size of the EA. Taking into account statistics, the probability of finding such substations is 0.58.

3. An algorithm for determining the minimum required depth of sounding depending on the size of the diagonal of the EA of the substation and the ratio of SER of soil layers is developed.

REFERENCES

1. *Pravyla ulashtuvannja elektroustanovok* [Electrical Installation Regulations]. Kharkiv, Fort Publ., 2017. 760 p. (Ukr).

2. Baranov M.I., Buriakovskyi S.G., Rudakov S.V. The tooling in Ukraine of model tests of objects of energy, aviation and space-rocket engineering on resistibility to action of pulsed current of artificial lightning. *Electrical engineering & electromechanics*, 2018, no.4, pp. 45-53. **doi: 10.20998/2074-272X.2018.4.08**.

3. *Natsional'nyy standart Ukrayiny. SOU 31.2-21677681-19:2009. Viprobuvannya ta kontrol' prystroyiv zazemlennya elektroustanovok. Tipova instruktsiya* [National Standard of Ukraine SOU 31.2-21677681-19:2009. Test and control devices, electrical grounding. Standard instruction]. Kyiv, Minenergovugillya Ukrayiny Publ., 2010. 54 p. (Ukr).

4. Koliushko D.G., Rudenko S.S. Analysis of methods for monitoring of existing energy objects grounding devices state at the present stage. *Electrical engineering & electromechanics*, 2019, no.1, pp. 67-72. **doi: 10.20998/2074-272X.2019.1.11.**

5. Koliushko D.G., Rudenko S.S., Koliushko G.M. Analysis of electrophysical characteristics of grounds in the vicinity electrical substation of Ukraine. *Electrical engineering & electromechanics*, 2015, no.3, pp. 67-72. (Rus). **doi: 10.20998/2074-272X.2015.3.10.**

6. Kostruba S.I. *Izmerenie elektricheskih parametrov zemli i zazemlyayushchih ustrojstv* [Measurement of electrical parameters of the earth and grounding device]. Moscow, Energoatomizdat Publ., 1983. 168 p. (Rus).

7. Koliushko G.M., Koliushko D.G., Rudenko S.S. On the problem of increasing computation accuracy for rated parameters of active electrical installation ground grids. *Electrical engineering & electromechanics*, 2014, no.4, pp. 65-70. (Rus). **doi: 10.20998/2074-272X.2014.4.13**.

8. Kolechitsky E.S., Medvedev V.T. Estimation of the size of the current spreading zone in the area of grounding conductors. *Energetik*, 2015, no.10, pp. 17-20. (Rus).

9. Borisov R.K., Gorshkov A.V., Zharkov Y.V. *Zazemliaiushchie ustroistva elektroustanovok (trebovaniia normativnykh dokumentov, raschet, proektirovanie, konstruktsii, sooruzhenie): spravochnik* [The grounding system of electrical installations (regulatory requirements, calculation, design, construction: Handbook]. Moscow, Publishing House MEI, 2013. 360 p. (Rus).

Received 16.09.2019

D.G. Koliushko[1], *Candidate of Technical Science, Senior Research Scientist,*
S.S. Rudenko[1], *Candidate of Technical Science, Senior Research Scientist,*
L.V. Asmolova[1], *Candidate of Technical Science, Associate Professor,*
T.I. Tkachova[2], *Research Scientist,*
[1] National Technical University «Kharkiv Polytechnic Institute», 2, Kyrpychova Str., Kharkiv, 61002, Ukraine,
e-mail: nio5_molniya@ukr.net
[2] National Science Center «Kharkov Institute of Physics and Technology»,
1, Akademicheskaya Str., Kharkov, 61108, Ukraine.

How to cite this article:
Koliushko D.G., Rudenko S.S., Asmolova L.V., Tkachova T.I. Determination of the soil sounding depth for the earthing resistance calculation of substations 35 kV. *Electrical engineering & electromechanics*, 2020, no.1, pp. 52-55. **doi: 10.20998/2074-272X.2020.1.08.**

UDC 621.316.925 **doi: 10.20998/2074-272X.2020.1.09**

V.F. Syvokobylenko, V.A. Lysenko

MULTIFREQUENCY PROTECTING METHOD AGAINST EARTH-FAULTS OF PHASE IN THE COMPENSATED ELECTRIC NETWORKS

Introduction. A significant proportion of earth faults in 6 - 35 kV networks is a transient and short-lived process, which is followed by an electric arc. Problem. In such cases, earth-fault protection that responds to steady-state current and voltage is not able to operate properly. Also, the use of the Petersen coil to compensate for the capacitive earth fault current complicates the protection function because it significantly reduces the single phase earth fault current in steady state. Purpose. To develop selective single-phase earth faults protection algorithm using harmonic components that occur in zero-sequence currents and voltage in the transient process. Method. A mathematical model of the power supply system is applied to study the frequency components of currents and voltage of zero sequence in compensated electrical networks with phase-to-earth faults, and a mathematical model is used to test the operation of the developed protection algorithm. The results showed that, the reactive power for harmonic components of the frequency greater than 100 Hz, which are separated from the current and voltage of zero sequence in compensated electrical networks on the damaged feeder, is positive regardless of the degree of compensation of the capacitive current. That may be the basis of the principle of directional protection. Originality. Phase-to-earth fault selective protection algorithm has been developed. In that algorithm, first derivatives of currents and voltages of zero sequence are found, to reduce the influence of aperiodic components. And then, by using of the Fourier transform, a number of harmonic orthogonal components are extracted from them. Reactive power is calculated for each of frequency component and their total sum is found. If that sum excess of threshold, the relay will make a decision. The reliability of the developed protection algorithm is confirmed by the results of mathematical modeling and verification of the test sample at the laboratory stand and by means of field signals that were recorded by digital loggers at the substations. References 10, table 1, figures 6.

Key words: **electrical network, earth fault protection, zero sequence current and voltage, Fourier transform, frequency spectrum.**

За допомогою математичної моделі компенсованої електричної мережі виконано аналіз струмів і напруг нульової послідовності при замиканнях фази на землю і показано, що в них під час перехідного процесу виникають вищі гармонійні складові, які обумовлені розрядом ємностей ушкодженої фази, дозарядом ємностей неушкоджених фаз, а також зростанням струму реактора в нейтралі мережі. Показано, що незалежно від ступеня компенсації реактором ємнісного струму промислової частоти, реактивна потужність для гармонічних складових струмів і напруг з частотою в два рази і більше промислової, є додатною для ушкодженого приєднання і від'ємною для неушкоджених. Це прийнято за основу в розробленому методі захисту направленої дії, в якому при замиканнях фази на землю спочатку визначають похідні струмів і напруг нульової послідовності, що зменшує вплив аперіодичних складових і підсилює складові вищих гармонік, а потім за допомогою перетворення Фур'є знаходять комплексні значення для ряду найбільш впливових гармонійних складових, більших за першу. За допомогою отриманих складових струмів і напруг для кожної частоти знаходять реактивну потужність, і якщо їх сума перевищує задану, то спрацьовує вихідний орган захисту. Достовірність розробленого методу захисту підтверджено результатами математичного моделювання і перевіркою роботи дослідного зразка на лабораторному стенді. Бібл. 10, табл. 1, рис. 6.

Ключові слова: **електрична мережа, захист від замикань на землю, струм і напруга нульової послідовності, перетворення Фур'є, частотний спектр.**

С помощью математической модели компенсированной электрической сети выполнен анализ токов и напряжений нулевой последовательности при замыканиях фазы на землю и показано, что у них во время переходного процесса возникают высшие гармонические составляющие, которые обусловлены разрядом емкостей поврежденной фазы, дозарядом емкостей неповрежденных фаз, а также ростом тока реактора в нейтрале сети. Показано, что независимо от степени компенсации реактором емкостного тока для промышленной частоты, реактивная мощность, рассчитанная для выделенных гармонических составляющих токов и напряжений с частотой в два раза и более промышленной, положительная для поврежденного присоединения и отрицательная для неповрежденных. Это принято за основу в разработанной защите направленного действия, в которой при замыканиях фазы на землю сначала определяют производные токов и напряжений нулевой последовательности, что уменьшает влияние апериодических составляющих и усиливает гармонические составляющие, а затем с помощью преобразования Фурье находят комплексные значения для ряда наиболее влиятельных гармонических составляющих, больших первой. С помощью полученных составляющих токов и напряжений для каждой частоты находят реактивную мощность, и если их сумма превышает заданную, то срабатывает выходной орган защиты. Достоверность разработанной защиты подтверждена результатами математического моделирования и проверкой работы опытного образца на лабораторном стенде. Библ. 10, табл. 1, рис. 6.

Ключевые слова: **электрическая сеть, защита от замыканий на землю, ток и напряжение нулевой последовательности, преобразования Фурье, частотный спектр.**

The relevance of the problem and its relation to the applied tasks. 6-10 kV electrical networks operating in the grounded neutral mode are the basis of power supply systems for industrial enterprises, power plants, cities. Given the large length and widespread of such networks, the problem of protecting networks from the most common damage of insulation – single-phase earth faulting – is urgent. A large proportion of earth faults is a transient and short-term process that is accompanied by an electric arc. In such cases, a ground fault protection device that responds to steady-state current and voltage is

not able to operate properly. Also, the use of the Petersen coil to compensate for the capacitive earth fault current complicates the operation of the protection devices as it significantly reduces the single-phase earth fault current in steady state.

Review of publications and shortcomings of known solutions. The problem of the analysis of transients in networks with earthed neutral in order to create an effective algorithm for protection against unstable earth faults is being actively investigated in Europe and around the world [1-3]. In particular, the work [3] investigates the aperiodic component of the transient of a single-phase earth fault and analyzes its influence on the work of known methods of protection against such earth fault. Much attention is paid to the peculiarities of mathematical modelling of the electric arc in the place of damage and methods of classification of different types of damage [4, 5]. In [6], methods of filtering the signals of current and voltage sensors are investigated, and attention is paid to testing them using real signals recorded by the logger at an operating substation. In [7], methods for the identification of single-phase earth faults are developed and the sensitivity of such methods under conditions of high resistance at the fault location is analyzed. Mathematical models of electrical networks are studied, which also include models of relay protection devices [8, 9]. The search for optimal parameters of mathematical methods of signal processing of primary sensors and settings for the operation of systems of protection against single-phase earth fault [6, 10] is carried out. There are also known attempts to use different types of neural network-type «black box» methods to protect against single-phase earth-faulting, but in our opinion, the simpler approaches are not exhausted, the most attractive being the analysis and use of different frequency components in currents ($3i_0$) and the voltage ($3u_0$) of the zero sequence.

The goal of investigation. Using a mathematical model to study the harmonic composition of currents and voltages of zero sequence in compensated electrical networks at phase-to-earth faults and to develop a method of selective protection by using harmonic components that occur in currents and voltages of zero sequence in transients.

Main material and results obtained. In works [8, 9], for selective protection against phase-to-earth short circuits, it is proposed to use frequency filters to select from the zero sequence current $3i_0$ and zero sequence voltage $3u_0$ components of one of the frequencies, for example, 200 or 300 Hz and to provide selectivity of the protection operation in the direction of the calculated reactive power the effect on which of the reactor at these frequencies is significantly attenuated. In this paper, to increase the sensitivity of the protection, we consider the possibility of the simultaneous use of currents and voltages for several frequencies found through the Fourier transform.

To study the harmonic composition of the currents $3i_0$ and the voltage $3u_0$ of the zero sequence, we use the mathematical model described in [8]. We apply it, for example, to a compensated electrical network consisting of a 110 kV transmission line, a step-down transformer, which is connected to a 6 kV section with three cable lines, phase capacities in each of which are respectively 3.8 μF and 12 μF. The network neutral is grounded through a reactor with a resonant inductance of 0.142 H. The results of simulation of deaf and arc single-phase earth fault (SEF) under different modes of reactor tuning showed that the currents $3i_0$ and voltage $3u_0$ at the beginning of the transient contain aperiodic and periodic components with different damping constants which are caused by discharge of capacities of damaged phases, recharge of capacities of intact phases as well as an increase in reactor current in network neutral. The duration of this transient is approximately the period of power frequency (20 ms). Comparison of the Fourier spectra for the currents $3i_0$ and voltages $3u_0$, as well as for their derivatives $p(3i_0)$ and $p(3u_0)$, showed that the harmonic amplitudes and the calculated values of the reactive power by means of the derivatives are almost an order of magnitude greater and are expedient to use their in protection. The nature of the change in time of the derivatives of the current and the voltage of the zero sequence at SEF is shown in Fig. 1. The differentiation operation significantly reduces the aperiodic components and enhances the higher frequency components. The numerical calculation of the orthogonal component of signals using the derivatives $p(3i_0)$ and $p(3u_0)$ is performed by (1) for three discrete instantaneous values of current (voltage) x_{n-2}, x_{n-1}, x_n for the step of calculation, for example $h = 0.625$ ms and for frequency $\omega = 314$ s^{-1}.

$$\frac{d}{dt}(x) = px = \frac{1}{2\omega h}(3x_{n-2} - 4x_{n-1} + x_n). \qquad (1)$$

The Fourier spectrum (Fig. 2) is calculated for the data shown in Fig. 1 and from which an array of $N = 32$ discrete elements is formed over time of 0.02 s.

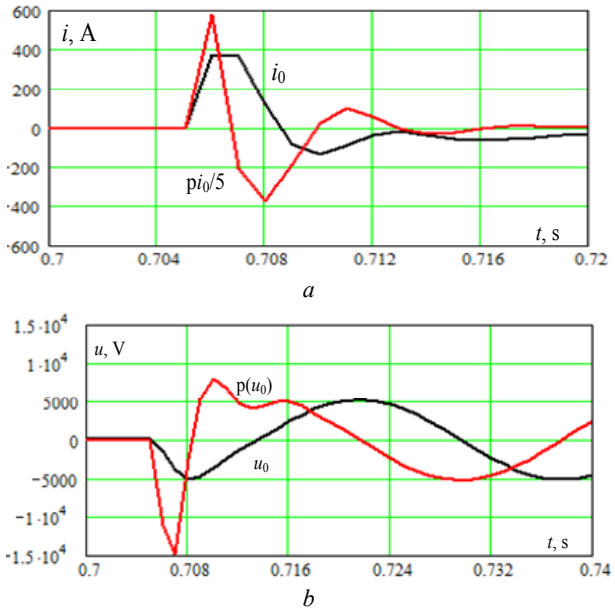

Fig. 1. Nature of the change in time of the zero sequence current and the derivative of this current (*a*), the voltage of the zero sequence and the derivative of this voltage (*b*) at SEF

From the numerical data obtained using the *fft*(*y*) function of MathCAD and shown in Fig. 2, it follows that the most influential harmonics are in the frequency range of 150-500 Hz.

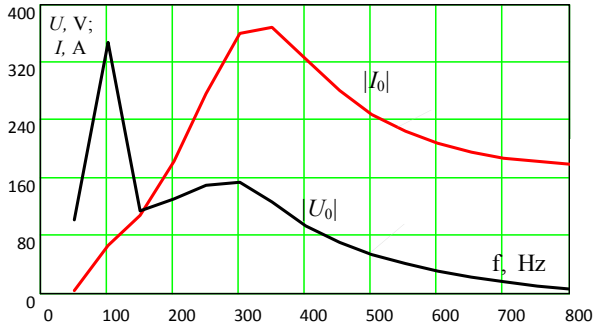

Fig. 2. Fourier spectrum for current and voltage derivatives of the zero sequence at SEF

The calculations for each k-th harmonic of reactive power using the complex values of currents and voltages obtained by the Fourier transform are performed according to the expressions (2):

$$q_k = i_{\alpha k} \cdot u_{\beta k} - i_{\beta k} \cdot u_{\alpha k};$$
$$p(\vec{i_0})_k = i_{\alpha k} - j i_{\beta k}; \quad (2)$$
$$p(\vec{u_0})_k = u_{\alpha k} + j u_{\beta k}.$$

The results of the calculation using the Fourier transform of the amplitudes of currents and voltages, reactive and active powers for the harmonics of multiples of the first one (f_0 = 50 Hz) in the range from 1 to 9 are shown in Table 1.

The data (Table 1) are shown for the reactor resonance tuning mode. According to these data, it is advisable to use for the protection harmonics with multiplicities 3, 4, 5, 6, for which the reactive power values are maximum. Calculations for reactor overcompensation modes have shown that the reactive power for harmonics 1, 2 can be negative and therefore it is undesirable to use these harmonics.

Table 1

Results of the calculation of reactive and active powers and amplitudes of harmonic components for derivatives of currents and voltages

f/f_0	I, A	U, V	Q, kVA	P, kW
1	66.15	5196	226	–259
2	106.6	1715	182.8	3.058
3	181.3	1957	354.5	11.22
4	277.0	2234	618.8	6.941
5	360.0	2287	822.7	–37.46
6	367.4	1900	692	–95.31
7	324.0	1406	441	–11.32
8	280.0	1044	273	–104
9	246.0	796	177	–85.48

Based on the obtained calculation data, a method of selective protection was developed, the block diagram of the algorithm of which is shown in Fig. 3 and in which there are: analog-to-digital converters – ADC, Fourier transform units – FFT, units of determination of derivatives – d/dt, multiplication units – X, summation unit – Σ, comparators for comparison of voltage amplitudes $3u_0$ with set value for frequency 50 Hz and the total reactive power Q_T for selected harmonics with set value U_T, logic elements OR, AND, as well as the output organ Relay.

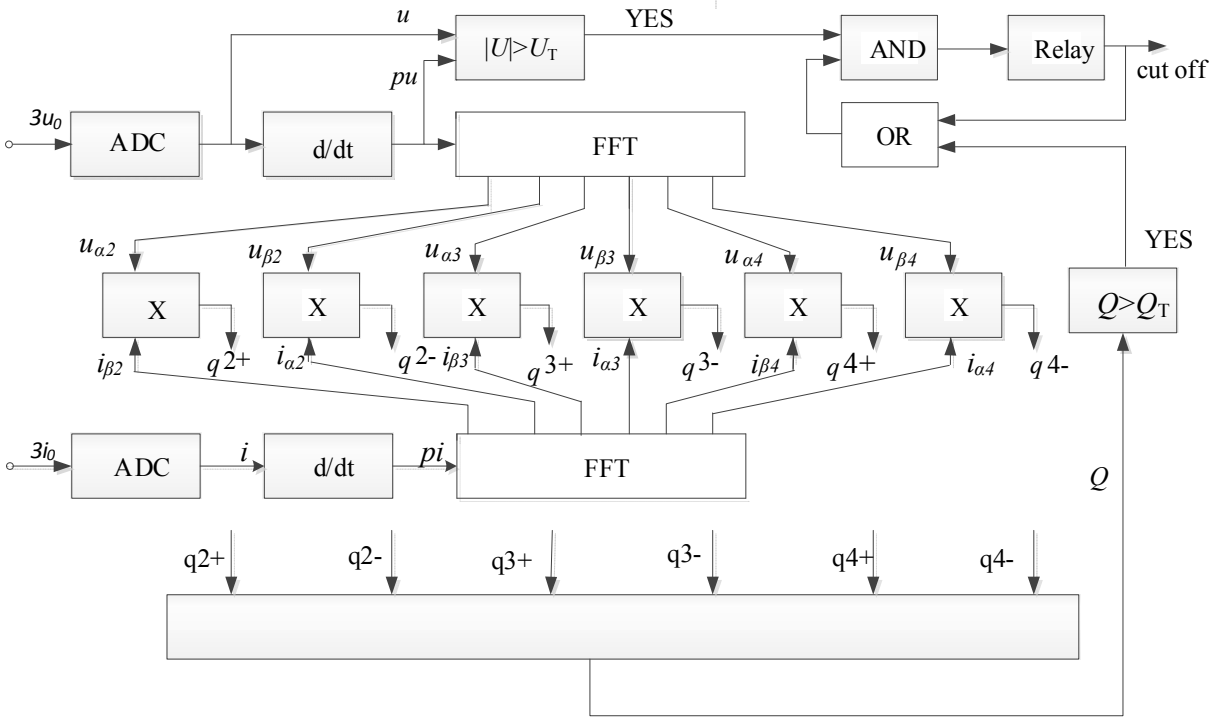

Fig. 3. Block diagram of the multifrequency method of selective earth-fault protection in compensated networks

The actuation organ is triggered if the voltage amplitude $3u_0$ exceeds the set value U_T which is 10-15% of the nominal value. The amplitude of this voltage is calculated from the orthogonal components that are obtained from the ADC and d/dt units and then calculated as $\sqrt{u_n^2 + (pu_n)^2}$.

The relay input signals – the current $3i_0$ and voltage $3u_0$ after ADC and d/dt differentiation units are fed to the Fourier transform units in which for given frequencies f_2 –

f_n complex values of harmonic components for currents (sine $i_{\beta 2}$, $i_{\beta 3}$,… and cosine $i_{\alpha 2}$, $i_{\alpha 3}$,…) and for voltages (sine $u_{\beta 2}$, $u_{\beta 3}$,… and cosine $u_{\alpha 2}$, $u_{\alpha 3}$,…) are calculated. Based on these values for each of the frequencies, in the respective units of multiplication X the positive (q^+) and negative (q^-) values of the reactive power are calculated. For each frequency they are found as:

$$q^+ = u_\beta \cdot i_\alpha; \quad q^- = u_\alpha \cdot i_\beta; \quad q = q^+ - q^-.$$

In the general mathematical model of the compensated electrical system and the protection relay, a software module for the implementation of the Fourier transform and the determination of the total reactive power of the higher harmonics f (the third through the sixth ones) are shown in Fig. 4.

$$\begin{aligned}
&Fur(FI, FU) := \\
&\quad I \leftarrow FI \\
&\quad U \leftarrow FU \\
&\quad N \leftarrow rows(U) \\
&\quad for \;\; f \in 3..6 \\
&\qquad Ico_f \leftarrow \sum_{n=1}^{N} I_n \cdot cos\left[\frac{2 \cdot \pi \cdot f}{N} \cdot (N-n)\right] \\
&\qquad Isi_f \leftarrow \sum_{n=1}^{N} I_n \cdot sin\left[\frac{2 \cdot \pi \cdot f}{N} \cdot (N-n)\right] \\
&\qquad Uco_f \leftarrow \sum_{n=1}^{N} U_n \cdot cos\left[\frac{2 \cdot \pi \cdot f}{N} \cdot (N-n)\right] \\
&\qquad Usi_f \leftarrow \sum_{n=1}^{N} U_n \cdot sin\left[\frac{2 \cdot \pi \cdot f}{N} \cdot (N-n)\right] \\
&\qquad Q_f \leftarrow \frac{2^2}{N^2} \cdot \left(Ico_f \cdot Usi_f - Isi_f \cdot Uco_f\right) \\
&\quad Q \leftarrow \sum_{f=3}^{6} Q_f
\end{aligned}$$

Fig. 4. MathCAD software module for Fourier transform realization in the protection relay against SEF

The results of the mathematical modelling of the protection method in the case of SEF show that the total reactive power of the harmonics depends on the instantaneous value of the phase voltage at the time of the fault. The highest value of reactive power occurs when the phase voltage (u_f) reaches the amplitude value (Fig. 5,*a*,*c*), and the least one – when reaching the zero value (Fig. 5,*b*,*d*). These power values (Fig. 5,*c*,*d*) are more than an order of magnitude and to be taken into account when selecting the set value for the comparator Q_T.

The results of the mathematical simulation of the relay operation at arc short circuits to the ground, the first of which arose at the amplitude value of the phase voltage, and the second one at zero, are shown in Fig. 6. Character of change of voltage $3u_0$ – in Fig. 6,*a*, of the current $3i_0$ and its derivatives $p(3i_0)$ – in Fig. 6,*b* and of the contacts of the relay output organ – in Fig. 6,*c*. In both cases, a clear relay operation was obtained.

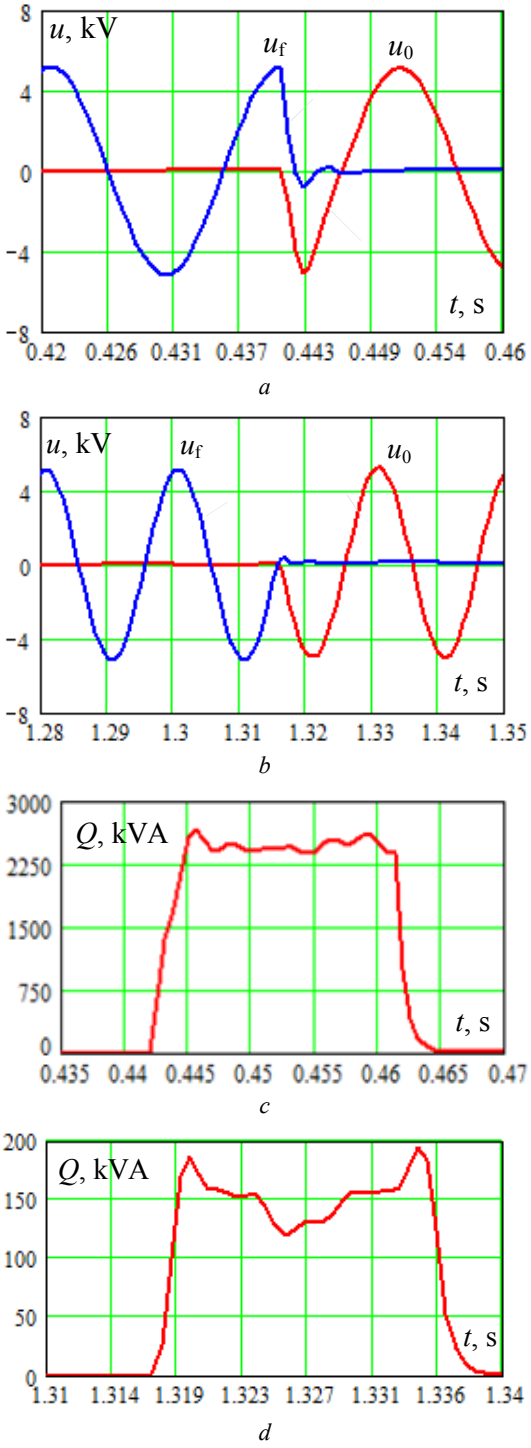

Fig. 5. Results of calculations of reactive power (*c*, *d*) at occurrence of SEF at maximum (*a*) and minimum (*b*) values of phase voltage

The simulation of the operation of the protection relay under the conditions of five-fold undercompensation and overcompensation of the capacitive current, as well as at SEF in the protection zone and outside the protection zone, confirmed the correct and reliable operation of the relay.

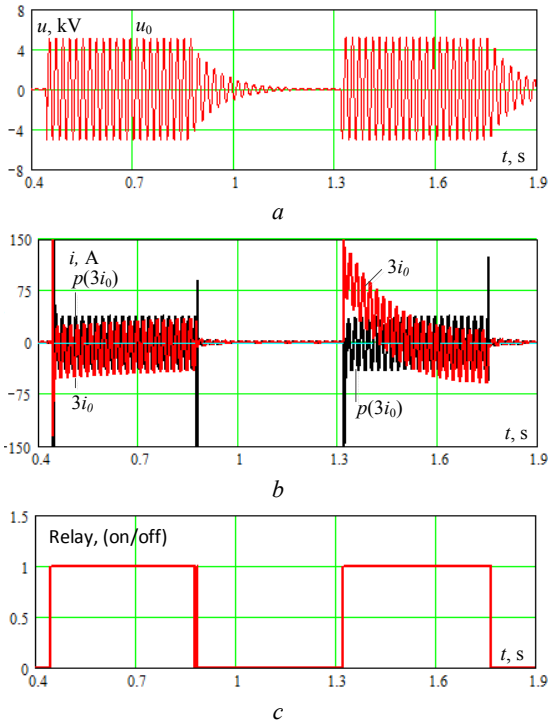

Fig. 6. Results of modelling the behavior of the protection relay at SEF with different aperiodic components in $3i_0$

The prototype of protection according to the algorithm shown in Fig. 3 was implemented on the basis of microcontroller STM32F4Discovery. Its satisfactory operation in the case of SEF was obtained on the physical model of the compensated electrical network with voltage of 0.4 kV, as well as inputting current and voltage signals of zero sequence which were recorded by digital loggers in the real network at SEF.

The results of simulations and experiments confirm the possibility of implementation of the developed protection in the operating electrical networks.

Conclusions.

1. The results of mathematical modelling show that in compensated electrical networks at phase-to-earth fault, the reactive power of the damaged connection, which is found using harmonic components extracted from the current and voltage of zero sequence for frequencies greater than 100-150 Hz, is positive regardless of the degree compensation of the capacitive current by the reactor, which can be the basis for the operation of selective protection.

2. A method of selective protection of the electrical network against phase-to-earth fault has been developed, using which, in order to reduce the influence of aperiodic components, first the derivatives of currents and voltages of the zero sequence are obtained, and then by means of the Fourier transform, a number of harmonic orthogonal components are extracted from each of them. which the reactive power is calculated and their total sum is found, and if it exceeds the specified one, the output organ is triggered.

3. The reliability of the developed method of selective protection is confirmed by the presented results of mathematical modelling and verification of the prototype operation at the laboratory stand, as well as by means of field signals recorded by digital registrars at SEF at operating substations.

REFERENCES

1. Shafiq M., Kiitam I., Taklaja P., Kütt L., Kauhaniemi K., Palu I. Identification and location of PD defects in medium voltage underground power cables using high frequency current transformer. *IEEE Access*, 2019, vol.7, pp. 103608-103618. **doi: 10.1109/ACCESS.2019.2930704.**

2. Marciniak L. General earth fault protection for MV networks using wavelet decomposition and Bayesian criterion. *E3S Web of Conferences*, 2019, vol.84, p. 02007. **doi: 10.1051/e3sconf/20198402007.**

3. Habrych M. Comparative performance study of the Hall sensor based directional ground fault protection in MV mining network with ineffective earthing. *Przegląd Elektrotechniczny*, 2016, no.8, pp. 251-254. **doi: 10.15199/48.2016.08.65**.

4. Kavaskar S., Mohanty N.K. Detection of high impedance fault in distribution networks. *Ain Shams Engineering Journal*, 2019, vol.10, no.1, pp. 5-13. **doi: 10.1016/j.asej.2018.04.006.**

5. Torres V., Guardado J.L., Ruiz H.F., Maximov S. Modeling and detection of high impedance faults. *International Journal of Electrical Power & Energy Systems*, 2014, vol.61, pp. 163-172. **doi: 10.1016/j.ijepes.2014.03.046.**

6. Daqing Hou. Detection of high-impedance faults in power distribution systems. *2007 Power Systems Conference: Advanced Metering, Protection, Control, Communication, and Distributed Resources*, Clemson, SC, 2007, pp. 85-95. **doi: 10.1109/PSAMP.2007.4740902.**

7. Marciniak L. Identyfikacja zwarć doziemnych wysokorezystancyjnych w sieciach średnich napięć. *Przegląd Elektrotechniczny*, 2015, no.8, pp. 185-189. (Pol). **doi: 10.15199/48.2015.08.45.**

8. Syvokobylenko V.F., Lysenko V.A. Mathematical modeling of new algorithms for single-phase earth faults protection in a compensated electrical network. *Problemele Energeticii Regionale*, 2019, no.1-2(41), pp. 1-11. **doi: 10.5281/zenodo.3239135.**

9. Syvokobylenko V.F., Lysenko V.A. Microprocessor selective protection from the phase to the earth fault in electric networks with Petersen coil in neutral. *Technical Electrodynamics*, 2019, no.2, pp. 54-62. (Rus). **doi: 10.15407/techned2019.02.054.**

10. Marciniak L. Określenie nastaw zabezpieczenia ziemnozwarciowego z falkowymi kryteriami działania. *Przegląd Elektrotechniczny*, 2014, no.6, pp. 261-264. (Pol). **doi: 10.12915/pe.2014.06.52.**

Received 11.10.2019

V.F. Syvokobylenko[1], *Doctor of Technical Science, Professor,*
V.A. Lysenko[1], *Candidate of Technical Science,*
[1] Donetsk National Technical University,
2, Shybankova Square, Pokrovsk, Donetsk region, 85300, Ukraine,
e-mail: svf1934@gmail.com, viktor.lysenko@donntu.edu.ua

How to cite this article:
Syvokobylenko V.F., Lysenko V.A. Multifrequency protecting method against earth-faults of phase in the compensated electric networks. *Electrical engineering & electromechanics*, 2020, no.1, pp. 56-60. **doi: 10.20998/2074-272X.2020.1.09.**

UDC 621.3 **doi: 10.20998/2074-272X.2020.1.10**

M. Dehghani, Z. Montazeri, O.P. Malik, K. Al-Haddad, J. M. Guerrero, G. Dhiman

A NEW METHODOLOGY CALLED DICE GAME OPTIMIZER FOR CAPACITOR PLACEMENT IN DISTRIBUTION SYSTEMS

Purpose. Shunt capacitors are installed in power system for compensating reactive power. Therefore, feeder capacity releases, voltage profile improves and power loss reduces. However, determination optimal location and size of capacitors in distribution systems is a complex optimization problem. In order to determine the optimum size and location of the capacitor, an objective function which is generally defined based on capacitor installation costs and power losses should be minimized According to operational limitations. This paper offers a newly developed metaheuristic technique, named dice game optimizer to determine optimal size and location of capacitors in a distribution network. Dice game optimizer is a game based optimization technique that is based on the rules of the dice game. References 27, tables 3, figures 3.
Key words: **capacitor placement, dice game optimizer, distribution systems, optimization algorithm.**

Цель. Шунтирующие конденсаторы в энергосистеме устанавливаются для компенсации реактивной мощности. Следовательно, снижается емкость фидера, улучшается профиль напряжения и снижаются потери мощности. Однако определение оптимального местоположения и размера конденсаторов в системах распределения является сложной задачей оптимизации. Чтобы определить оптимальный размер и расположение конденсатора, целевую функцию, которая обычно определяется на основе затрат на установку конденсатора и потерь мощности, следует минимизировать в соответствии с эксплуатационными ограничениями. Данная статья предлагает недавно разработанный метаэвристический метод, называемый оптимизатором игры в кости, для определения оптимального размера и расположения конденсаторов в распределительной сети. Оптимизатор игры в кости – это игровой метод оптимизации, основанный на правилах игры в кости. Библ. 27, табл. 3, рис. 3.
Ключевые слова: **размещение конденсаторов, оптимизатор игры в кости, системы распределения, алгоритм оптимизации.**

Introduction. Capacitor banks are widely used in distribution systems for power loss reducing, voltage profile improving, feeder capacity releasing, reactive power compensating and power factor correcting. To get the maximum profit, capacitors should be optimally placed in distribution systems. Therefore, optimal place of capacitors should be determined with the help of an optimization technique. There are different objective functions and several solving methods for capacitor placement problem. These suggested objective functions are: minimize the power loss, minimize the capacitor installation cost, improve the voltage profile, reduce the burden on existing lines, maximize the network stability, and etc [1]. In general, capacitor placement problem is a hybrid optimization problem which should be effectively solved by a superior optimization technique. These techniques can be divided into four classes: analytical, numerical programming, heuristic and artificial intelligence techniques [2]. Heuristic techniques are quick and practical tools, which reduce the total search space and can result in a solution close to the optimal place of the capacitor with confidence [3]. In recent decade, metaheuristic algorithms have received a significant attention to solve the optimal capacitor bank placement problem. Compared with the common search techniques that require continuity, convexity and differentiability of the problem under investigation, metaheuristic algorithms do not require the derivative information and use stochastic rules to solve the problem. in this regard, capacitor placement problem has been solved by metaheuristic algorithms such as: genetic algorithm (GA) [4], immune system (IS) algorithm [5], particle swarm optimisation (PSO) [6], tabu search (TS) [6], memetic algorithm (MA) [7], graph search algorithm [8], teaching–learning-based optimization (TLBO) [9], and ant colony (AC) [10]. Other algorithms are also proposed to solve the capacitor replacement problem such as spring search algorithm (SSA) [11, 12], orientation search algorithm (OSA) [13], Donkey Theorem Optimization (DTO) [14], Following Optimization Algorithm (FOA) [15], binary orientation search algorithm [16], and group optimization (GO) [17].

Paper contribution and purposes.

Due to the sufficiency of the metaheuristic techniques in optimization problems, in this study, the performance of a newly suggested metaheuristic technique which named dice game optimizer (DGO) is evaluated on capacitor placement problem. DGO is a game-based algorithm, which simulates rules of dice game and the searchers are a set of players.

This study proposes the dice game optimizer to obtain the optimal CBs placement and sizing in distribution systems. The proposed method aims to realize the following benefits:

1) studying the penetration of CBs to enhance the technical and economic issues of distribution systems;

2) technical objective is power loss reduction;

3) economic issue is considered as minimizing the costs of CBs;

4) applying the proposed method to standard radial distribution system;

5) increasing the awareness of the importance of penetration of CBs for enhancing the operation of electrical systems.

The rest of this paper has been organized as follows. Capacitor placement problem is defined In Section 2. DGO is introduced in section 3. Section 4, presented simulated results, and finally conclusion is given in Section 5.

Problem formulation.

Objective function.

Since the major object of capacitor placement is to reduce the total losses and bring the buses voltages within the permissible bound while minimizing the total cost, so the objective function is defined as

$$OF = k_p P_{loss} + \sum_{j=1}^{n} k_j^c Q_j^c , \quad (1)$$

where OF is the total cost of the distribution network (\$), k_p is the equivalent cost per unit of power loss (\$/kW), P_{loss} is the power loss of the distribution network (kW), n is the number of buses, Q_j^c is the size of the capacitor installed at bus j and k_j^c is the corresponding cost per kVar.

Power loss calculation.

In an assumed Π model of the network in which I branch is attached to k bus in one hand and to the m bus on the other hand, k bus is closer to the root bus that is the net power goes from k to m bus. Fig. 1 represents the power flow through the series impedance of the branch.

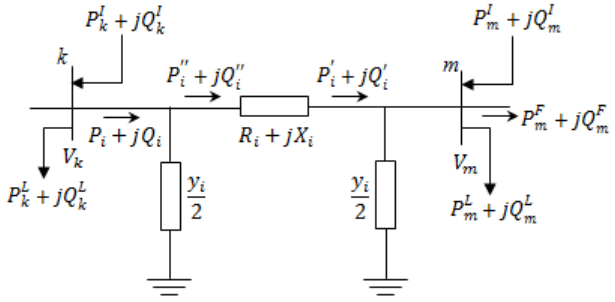

Fig. 1. Π model of a network

These flows are represented in (2) and (3), elaborately

$$P_i' = P_m^L + P_m^F - P_m^I , \quad (2)$$

$$Q_i' = Q_m^L + Q_m^F - Q_m^I - V_m^2 \frac{y_i}{2} , \quad (3)$$

where L, F and I subscripts represents the load, the flow and the injection respectively. Branch i let the power flow near bus k. This passage can be formulated as

$$P_i = P_i'' = P_i' + R_i \frac{P_i'^2 + Q_i'^2}{V_m^2} , \quad (4)$$

$$Q_i = Q_i'' - V_k^2 \frac{y_i}{2} = Q_i' + X_i \frac{P_i'^2 + Q_i'^2}{V_m^2} - V_k^2 \frac{Y_i}{2} . \quad (5)$$

In order to calculate the power flow quantity in each branch of tree, it is computed recursively in a backward/anti clock-wise direction. Thus, the bus m complex voltage is computed as

$$V_m = \left[V_k - \frac{P_i'' R_i + Q_i'' X_i}{V_k^*} \right] - j \left[\frac{P_i'' X_i - Q_i'' R_i}{V_k^*} \right] . \quad (6)$$

The strategy of finding the magnitude and angle of all buses voltages of the tree is to compute this complex voltage in a forward direction.

This computation is done iteratively again and again till the voltage difference at loop breaking points (breaking points of the tree) is placed within the acceptable limit. Hence the branch I active power loss (P_{Li}) is measured as

$$P_{Li} = P_i'' - P_i' = R_i \frac{P_i'^2 + Q_i'^2}{V_m^2} . \quad (7)$$

Accordingly, quantities of the system net active power loss is

$$P_L = \sum_{i=1}^{N} P_{Li} . \quad (8)$$

Dice Game Optimizer [18]. Optimization algorithms is applied by researchers in various science such as energy [19, 20], power engineering [21-23], energy carriers [24, 25] and protection [26].

DGO is a game based optimization algorithm, which simulates rules of the old game named dice game. In DGO the initial position of the players is created randomly on the playing field (problem definition space).

In (9), the position «*d*» of player «*i*» is shown as x_i^d

$$X_i = \left(x_i^1, ..., x_i^d, ..., x_i^n \right). \quad (9)$$

After the formation of the system, the rules are specified. Players compete with each other to determine the winner according to the rules of the game.

Calculation of each player's score.

In order to simulate the score of each player, a fitness function is used. It assigns higher score to the player with a better location. This parameter is computed according to

$$Score_i = \frac{fit_i - fit(player_{best})}{\sum_{j=1}^{N} fit_j - fit(player_{worst})} , \quad (10)$$

where $Score_i$ is the score of player I, fit_i is the value of the fitness function, N is the number of players, $player_{best}$ is the position of the best player and $player_{worst}$ is the position of the worst player.

These positions are indicated as

$$player_{best} = \text{location of } \min(fit_j) \,\&\, j \in \{1:N\} , \quad (11)$$

$$player_{worst} = \text{location of } \max(fit_j) \,\&\, j \in \{1:N\} . \quad (12)$$

Tossing dice for each player.

At this stage of the game each player tosses a dice once. A dice number is a discrete number between 1 and 6 that represents the number of player's guide of each player. The number of dice for each player is specified as

$$Dice_i = K \,\&\, K \in \{1\,2\,3\,4\,5\,6\} , \quad (13)$$

where $Dice_i$ is the dice number for i-th player. This number is specified by K.

Selection of the Guide's players for each player.

For each player, based on the number of dice (K), guide players are selected randomly among the players. These players are specified as

$$X_{Guide_i}^k = X_1 : X_K , \quad (14)$$

where $X_{Guide_i}^k$ is the position guide player number k of player «*i*».

Update of the position of each player.

Now $X^{i,d}$ is calculated as

$$X^{i,d} = X_0^{i,d} + \sum_{k=1}^{Dice_i} \left(r_k \left(X^{i,d} - X_{Guide_i}^{k,d} \right) sign\left(Score_i - Score_{Guide_k} \right) \right), \quad (15)$$

where r_k is the random number with normal distribution in the interval [0–1] and $Score_{Guide_k}$ is the score of guide player number k.

Simulations and results. The case study that is considered in this paper is a 12.66 kV and 33-bus distribution network shown in Fig. 2. The total active and reactive loads of this system are 3715 kW and 2300 kVar, respectively. In this network, the power losses are 201.8925 kW. The system information has been adopted from [27]. The standard capacitors information is shown in Table 1. The performance of DGO is compared by the results obtained by PSO, which this comparison is specified in Table 2.

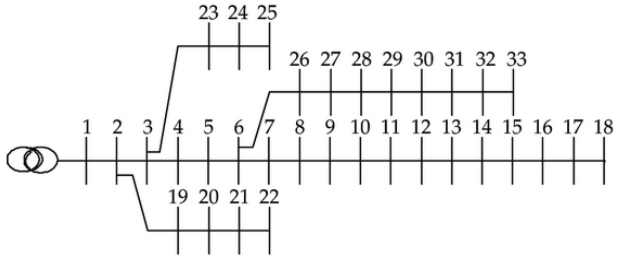

Fig. 2. Schematic of the 33-bus radial network

Table 1

Standard capacitors information

j	1	2	3	4	5	6
Q_j^c, kVar	150	300	450	600	750	900
k_j^c, $/kVar	0.5	0.35	0.253	0.22	0.276	0.183

Table 2

The simulation results of DGO and PSO

Index	Uncompensated	Algorithm	
		DGO	PSO
Annual cost, $	33917.94	22573.54	22861.93
Network loss, kW	201.8925	131.5359	132.4847
Net saving, $	N.A	11344.40	11056.01
Avg. time, s	N.A	53.43	58.39

Over 30 independent runs, the best performance of DGO is 22573.54 $ while PSO reaches to 22861.93 $. It is clear that DGO gives better results than PSO. In solve the capacitor placement by DGO, the power losses are 131.5359 kW while in the solve the capacitor placement by PSO the power losses are 132.4847 kW. Table 3 lists the installed kVar at each bus of the network.

Table 3

Optimal capacitor placement results

DGO		PSO	
Bus number	Capacitor (kVar)	Bus number	Capacitor (kVar)
11	600	2	900
24	450	7	450
30	600	15	300
33	300	29	450
–	–	31	450

Based on the DGO result, the value of the installed capacitor at buses 11, 24, 30 and 33 is 600, 450, 600 and 300 kVar, respectively. In this case, the 33-bus distribution network is compensated by 1950 kVar of capacitor. According to the PSO result, the value of installed capacitor at compensated buses 2, 7, 15, 29 and 31 is 900, 450, 300, 450 and 450 kVar, respectively. This means that the 33-bus distribution network is compensated by 2550 kVar of capacitor. Voltage profile of 33-bus distribution network shown in Fig. 3.

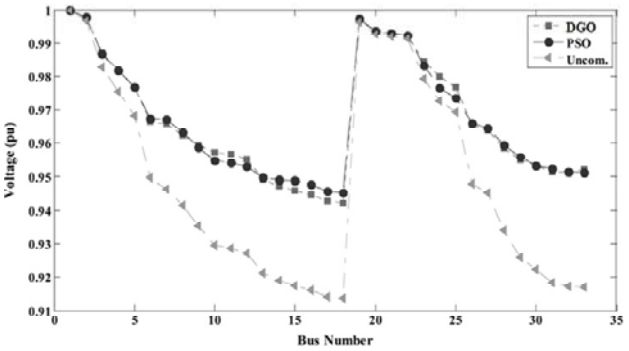

Fig. 3. Voltage profile of the 33-bus radial network

Conclusion. This paper proposes a new methodology for capacitor placement in distribution networks in order to power loss reduction and modify the voltage profile. The proposed methodology, which has applied here, is based on a new metaheuristic optimization technique, named dice game optimizer. In the simulation, it is looked that the results obtained by dice game optimizer are more precise than the results reported in the current literature. The convergence rate of dice game optimizer is good and it is looked that dice game optimizer solves the problem in less computational time than the other investigated techniques. As regard dice game optimizer is an efficient and rather simple algorithm, it would be suggested for various applications of power system engineering problems.

REFERENCES

1. Aman M.M., Jasmon G.B., Bakar A.H.A., Mokhlis H., Karimi M. Optimum shunt capacitor placement in distribution system – A review and comparative study. *Renewable and Sustainable Energy Reviews*, 2014, vol. 30, pp. 429-439. **doi: 10.1016/j.rser.2013.10.002**.

2. Ng H.N., Salama M.M.A., Chikhani A.Y. Classification of capacitor allocation techniques. *IEEE Transactions on Power Delivery*, 2000, vol. 15, no. 1, pp. 387-392. **doi: 10.1109/61.847278**.

3. Da Silva I.C., Carneiro S., de Oliveira E.J., de Souza Costa J., Pereira J.L.R., Garcia P.A.N. A heuristic constructive algorithm for capacitor placement on distribution systems. *IEEE Transactions on Power Systems*, 2008, vol. 23, no. 4, pp. 1619-1626. **doi: 10.1109/tpwrs.2008.2004742**.

4. Haghifam M.-R., Malik O.P. Genetic algorithm-based approach for fixed and switchable capacitors placement in distribution systems with uncertainty and time varying loads. *IET Generation, Transmission & Distribution*, 2007, vol. 1, no. 2, p. 244. **doi: 10.1049/iet-gtd:20045267**.

5. Shyh-Jier Huang. An immune-based optimization method to capacitor placement in a radial distribution system. *IEEE Transactions on Power Delivery*, 2000, vol. 15, no. 2, pp. 744-749. **doi: 10.1109/61.853014**.

6. Lee C.-S., Ayala H.V.H., dos S. Coelho L. Capacitor placement of distribution systems using particle swarm optimization approaches. *International Journal of Electrical*

Power & Energy Systems, 2015, vol. 64, pp. 839-851. **doi: 10.1016/j.ijepes.2014.07.069**.

7. Mendes A., Franca P.M., Lyra C., Pissarra C., Cavellucci C. Capacitor placement in large-sized radial distribution networks. *IEE Proceedings – Generation, Transmission and Distribution*, 2005, vol. 152, no. 4, p. 496. **doi: 10.1049/ip-gtd:20059015**.

8. Carlisle J. C., El-Keib A.A. A graph search algorithm for optimal placement of fixed and switched capacitors on radial distribution systems. *IEEE Transactions on Power Delivery*, 2000, vol. 15, no. 1, pp. 423-428. **doi: 10.1109/61.847284**.

9. Sultana S., Roy P.K. Optimal capacitor placement in radial distribution systems using teaching learning based optimization. *International Journal of Electrical Power & Energy Systems*, 2014, vol. 54, pp. 387-398. **doi: 10.1016/j.ijepes.2013.07.011**.

10. Kaur D., Sharma J. Multiperiod shunt capacitor allocation in radial distribution systems. *International Journal of Electrical Power & Energy System*s, 2013, vol. 52, pp. 247-253. **doi: 10.1016/j.ijepes.2013.03.026**.

11. Dehghani M., Montazeri Z., Dehghani A., Nouri N., Seifi A. BSSA: Binary spring search algorithm. *2017 IEEE 4th International Conference on Knowledge-Based Engineering and Innovation (KBEI)*, Dec. 2017. **doi: 10.1109/kbei.2017.8324977**.

12. Dehghani M., Montazeri Z., Dehghani A., Seifi A. Spring search algorithm: A new meta-heuristic optimization algorithm inspired by Hooke's law. *2017 IEEE 4th International Conference on Knowledge-Based Engineering and Innovation (KBEI)*, Dec. 2017. **doi: 10.1109/kbei.2017.8324975**.

13. Dehghani M., Montazeri Z., Malik O.P., Ehsanifar A., Dehghani A. OSA: Orientation Search Algorithm. *International Journal of Industrial Electronics, Control and Optimization*, 2019, vol. 2, pp. 99-112.

14. Dehghani M., Mardaneh M., Malik O.P., NouraeiPour S.M. DTO: Donkey Theorem Optimization. *2019 27th Iranian Conference on Electrical Engineering (ICEE)*, Apr. 2019, pp. 1855-1859. **doi: 10.1109/iraniancee.2019.8786601**.

15. Dehghani M., Mardaneh M., Malik O. FOA: Following Optimization Algorithm for solving power engineering optimization problems. *Journal of Operation and Automation in Power Engineering*, 2020, vol. 8, iss. 1, pp. 57-64. **doi: 10.22098/JOAPE.2019.5522.1414.**

16. Dehghani M., Montazeri Z., Malik O.P., Dhiman G., Kumar V. BOSA: Binary Orientation Search Algorithm International. *Journal of Innovative Technology and Exploring Engineering*, 2019, vol. 9, iss. 1, pp. 5306-5310. **doi: 10.35940/ijitee.A4215.119119.**

17. Dehghani M., Montazeri Z., Dehghani A., Malik O.P. GO: Group Optimization. *Gazi University Journal of Science*, 2020, vol. 33.

18. Dehghani M., Montazeri Z., Malik O.P. DGO: Dice Game Optimizer. *Gazi University Journal of Science*, 2019, vol. 32, pp. 871-882. **doi: 10.35378/gujs.484643**.

19. Dehghani M., Montazeri Z., Malik O.P. Energy commitment: a planning of energy carrier based on energy consumption. *Electrical engineering & electromechanics*, 2019, no.4, pp. 69-72. **doi: 10.20998/2074-272X.2019.4.10.**

20. Montazeri Z., Niknam T. Optimal utilization of electrical energy from power plants based on final energy consumption using gravitational search algorithm. *Electrical engineering & electromechanics*, 2018, no.4, pp. 70-73. **doi: 10.20998/2074-272X.2018.4.12**.

21. Dehbozorgi S., Ehsanifar A., Montazeri Z., Dehghani M., Seifi A. Line loss reduction and voltage profile improvement in radial distribution networks using battery energy storage system. 2017 *IEEE 4th International Conference on Knowledge-Based Engineering and Innovation (KBEI)*, Dec. 2017. **doi: 10.1109/kbei.2017.8324976**.

22. Dehghani M., Mardaneh M., Montazeri Z., Ehsanifar A., Ebadi M.J., Grechko O.M. Spring search algorithm for simultaneous placement of distributed generation and capacitors. *Electrical engineering & electromechanics*, 2018, no.6, pp. 68-73. **doi: 10.20998/2074-272X.2018.6.10.**

23. Dehghani M., Montazeri Z., Malik O.P. Optimal sizing and placement of capacitor banks and distributed generation in distribution systems using spring search algorithm. *International Journal of Emerging Electric Power Systems*, 2020, vol. 21. **doi: 10.1515/ijeeps-2019-0217**.

24. Dehghani M., Montazeri Z., Ehsanifar A., Seifi A.R., Ebadi M.J., Grechko O.M. Planning of energy carriers based on final energy consumption using dynamic programming and particle swarm optimization. *Electrical engineering & electromechanics*, 2018, no.5, pp. 62-71. **doi: 10.20998/2074-272X.2018.5.10**.

25. Montazeri Z., Niknam T. Energy carriers management based on energy consumption. *2017 IEEE 4th International Conference on Knowledge-Based Engineering and Innovation (KBEI)*, Dec. 2017. **doi: 10.1109/kbei.2017.8325036**.

26. Ehsanifar A., Dehghani M., Allahbakhshi M. Calculating the leakage inductance for transformer inter-turn fault detection using finite element method. *2017 Iranian Conference on Electrical Engineering (ICEE)*, May 2017. **doi: 10.1109/iraniancee.2017.7985256**.

27. Baran M.E., Wu F.F. Network reconfiguration in distribution systems for loss reduction and load balancing. *IEEE Transactions on Power Delivery*, 1989, vol. 4, no. 2, pp. 1401-1407. **doi: 10.1109/61.25627**.

Received 24.12.2019

M. Dehghani[1]*, Candidate of Power Engineering, PhD Student,*
Z. Montazeri[1]*, Candidate of Power Engineering, PhD Student,*
O.P. Malik[2]*, Doctor of Power Engineering, Professor,*
Kamal Al-Haddad[3]*, FIEEE, FRSC, FACE, Professor,*
Josep M. Guerrero[4]*, Doctor of Power Electronics, Professor,*
G. Dhiman[5]*, Doctor of Computer Engineering, Assistant Professor,*
[1] Department of Electrical and Electronics Engineering,
Shiraz University of Technology, Shiraz, Iran,
e-mail: adanbax@gmail.com, Z.Montazeri@sutech.ac.ir
[2] Department of Electrical Engineering,
University of Calgary, Calgary Alberta Canada,
e-mail: maliko@ucalgary.ca
[3] École de technologie supérieur,
University of Quebec, Montreal, Canada,
e-mail: kamal.al-haddad@etsmtl.ca
[4] Department of Energy Technology,
Aalborg University, Aalborg, Denmark,
e-mail: joz@et.aau.dk
[5] Department of Computer Science,
Government Bikram College of Commerce,
Patiala, Punjab 147004, India,
e-mail: gaurav.dhiman@thapar.edu

How to cite this article:
Dehghani M., Montazeri Z., Malik O.P., Al-Haddad K., Guerrero J. M., Dhiman G. A new methodology called dice game optimizer for capacitor placement in distribution systems. *Electrical engineering & electromechanics*, 2020, no.1, pp. 61-64. **doi: 10.20998/2074-272X.2020.1.10.**

UDC 629.423 **doi: 10.20998/2074-272X.2020.1.11**

H.V. Omelianenko, L.V. Overianova, A.S. Maslii

GEOMETRIC AND ELECTROPHYSICAL PARAMETERS OF ARMATURE WINDING OF ELECTROMECHANICAL CONVERTER OF INERTIAL ENERGY STORAGE FOR SUBURBAN TRAINS

Purpose. *To establish analytical expressions of machine constant and electromagnetic parameters for a specific circuit of the armature winding of an electromechanical converter of an inertial energy storage device, which is a DC electric machine with a semiconductor switch and excitation from permanent magnets.* ***Methodology.*** *For research the theory of electrical circuits is used to create a mathematical model of the processes of electromechanical energy conversion in an inertial storage device. The plots method is used to find the mutual inductance of the armature winding coils, which are presented in the form of infinitely thin single-turn contours of rectangular shape, located in three-dimensional space.* ***Results.*** *Mathematical models of the processes of electromechanical energy conversion in an inertial storage device are obtained reflecting the relationship between the exchange energy and drive power with geometric and electrophysical parameters of both the energy accumulator and the system of its electromechanical converter. A connection of the parameters of machine constant, active and inductive resistances with the configuration, wiring diagram and the geometric dimensions of the armature winding has been established. The wiring of sections in the phase of the armature winding depends on the required value of the voltage and current of the machine. The possibility of regulating the voltage of the drive by switching on and off the working phases of the system of electromechanical converter, as well as by changing the angle of the load is shown.* ***Originality.*** *Mathematical models are obtained that relate the indicators of the energy of exchange and the power of the drive to the geometrical and electro physical parameters of both the energy accumulator and the system of its electromechanical converter. A feature of these models is operating with an average value of induction and machine constants when determining the electromotive force and electromagnetic moment.* ***Practical value.*** *Recommendations are developed for determining the machine constant and electromagnetic parameters of electromechanical inertial energy storage devices. This allows to evaluate the properties of devices of this type in the modes of storage and delivery of energy during their operation on board the rolling stock.* References 7, table 1, figures 5.

Key words: **inertial electromechanical energy storage, electromechanical converter, armature winding, machine constants, active resistance, inductive resistance.**

Мета. *Встановлення аналітичних виразів машинних постійних і електромагнітних параметрів для специфічної схеми обмотки якоря електромеханічного перетворювача інерційного накопичувача енергії у вигляді оберненої електричної машини постійного струму з напівпровідниковим комутатором і збудженням від постійних магнітів.* ***Методика.*** *Для проведення досліджень використана теорія електричних кіл, метод ділянок для знаходження взаємної індуктивності котушок обмотки якоря.* ***Результати.*** *Встановлено зв'язок параметрів машинних постійних, активного та індуктивного опорів з конфігурацією, схемою з'єднання і геометричними розмірами обмотки якоря.* ***Наукова новизна.*** *Для специфічних схем якірних обмоток системи електромеханічного перетворення енергії інерційних накопичувачів знайдені аналітичні вирази машинних постійних і електромагнітних параметрів, які визначають показники енергії обміну і потужності накопичувача.* ***Практичне значення.*** *Розроблені рекомендації щодо визначення машинних постійних і електромагнітних параметрів інерційних електромеханічних накопичувачів енергії дозволяють оцінити властивості пристроїв такого типу на борту рухомого складу.* Бібл. 7, табл. 1, рис. 5.

Ключові слова: **інерційний електромеханічний накопичувач енергії, електромеханічний перетворювач, обмотка якоря, машинні постійні, активний опір, індуктивний опір.**

Цель. *Установление аналитических выражений машинных постоянных и электромагнитных параметров для специфической схемы обмотки якоря электромеханического преобразователя инерционного накопителя энергии в виде обращенной электрической машины постоянного тока с полупроводниковым коммутатором и возбуждением от постоянных магнитов.* ***Методика.*** *Для проведения исследований использована теория электрических цепей, метод участков для нахождения взаимной индуктивности катушек обмотки якоря.* ***Результаты.*** *Установлена связь параметров машинных постоянных, активного и индуктивного сопротивлений с конфигурацией, схемой соединения и геометрическими размерами обмотки якоря.* ***Научная новизна.*** *Для специфических схем якорных обмоток системы электромеханического преобразования энергии инерционного накопителя найдены аналитические выражения машинных постоянных и электромагнитных параметров, которые определяют показатели энергии обмена и мощности накопителя.* ***Практическое значение.*** *Разработанные рекомендации по определению машинных постоянных и электромагнитных параметров инерционных электромеханических накопителей энергии позволяют оценить свойства устройств такого типа на борту подвижного состава.* Библ. 7, табл. 1, рис. 5.

Ключевые слова: **инерционный электромеханический накопитель энергии, электромеханический преобразователь, обмотка якоря, машинные постоянны, активное сопротивление, индуктивное сопротивление.**

Introduction. The use of energy storage devices, both in the traction network and on the rolling stock of railways, is one of the effective means of saving energy resources and protecting the environment. Of the four types of storage devices known to date that are suitable for these purposes (two-layer capacitors, lithium-ion batteries, flywheels, and superconducting magnets), only the first three types are now implemented [1-3]. Moreover, on the prototype suburban rolling stock – only of inertial type, which is an aggregate that consists of a

cylindrical flywheel connected on one shaft with a synchronous electric machine [4].

A more compact design of the inertial electromechanical energy storage device (IEMESD) takes place when the electromechanical converter, representing a DC machine with a thyristor switch, is located inside a hollow cylindrical flywheel. The design of such a storage device was previously developed at NTU «KhPI» for the traction network of the subway [5]. However, its parameters and performance are selected in such a way as to interact with the load – the traction network, as a rule, with insignificantly changing voltage.

The operation of IEMESD on electric rolling stock (ERS) is characterized by other conditions for the process of energy exchange between the storage device and the load – traction motors. Here, in the braking and acceleration mode of the ERS, significant changes in the nature and level of voltages on the traction motors and the storage device take place. The use of IEMESD on rolling stock makes it possible to utilize the braking energy and use it after that to accelerate the train, which provides an efficient energy-saving technology of electric transport. The accumulated energy circulates in the traction electric drive system, which saves up to 30% of the energy spent on traction [6].

Therefore, the study of the parameters of such drives in the conditions of their operation on the ERS is today a promising direction.

In the papers, the authors investigate IEMESD which is a combination of a flywheel and an electromechanical energy conversion system (EMECS), which is taken as a reversed DC electric machine with a semiconductor switch on IGBT transistors and excitation from permanent magnets (Fig. 1). Along with the magnetic system of the inductor, the configuration, connection diagram, and geometrical dimensions of the armature winding are decisive in obtaining the required power of EMECS.

The goal of the work is the establishment of analytical expressions of machine constants and electromagnetic parameters for specific circuits of armaturer windings of an electromechanical converter of an inertial energy storage device.

The mathematical model of EMECS storage device. A mathematical model of the processes of electromechanical energy conversion in EMECS connects its geometric and electrophysical parameters with power and energy indicators, and also determines the operating properties of EMECS in various operating modes.

An expression relating the rotational speed of the rotor n_n to the geometric and electromagnetic parameters of the storage device is obtained on the basis of the equation of equilibrium of moments.

The relationship between the voltage u_n and the current i_n in EMECS as a component of the instantaneous values of electromagnetic power is obtained from the equations of equilibrium of voltages in the armature winding.

The mathematical model that describes the processes in the EMECS of the storage device in the modes of energy storage and delivery has the form:

$$\begin{cases} \dfrac{dn_n}{dt} = \dfrac{C_{mn} B_{sr} i_n}{\pi/30\, J}; \\ \dfrac{di_n}{dt} = \dfrac{u_n - C_{en} B_{sr} n_n \sin\theta - R_n i_n}{L_n}, \end{cases} \quad (1)$$

$$\begin{cases} \dfrac{dn_n}{dt} = -\dfrac{C_{mn} B_{sr} i_n}{\pi/30\, J}; \\ \dfrac{di_n}{dt} = \dfrac{C_{en} B_{sr} n_n \sin\theta - u_n - R_n i_n}{L_n}, \end{cases} \quad (2)$$

where C_{mn}, C_{en} are the machine constants; B_{sr} is the average value of magnetic flux density; J is the moment of inertia of the flywheel; θ is the load angle between the axis of the magnetic field of the inductor and the magnetic field created by the armature current; R_n, L_n are the resistance and inductance of the winding.

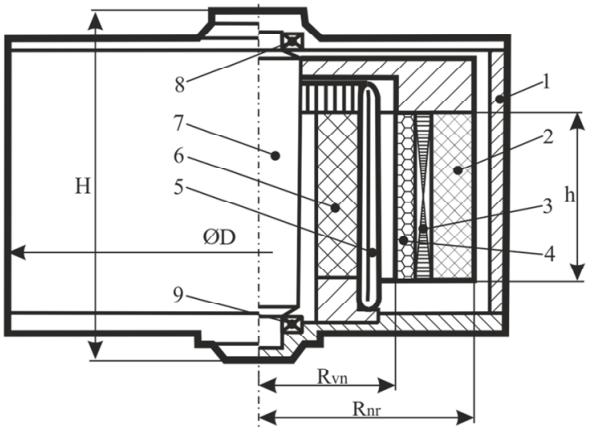

a

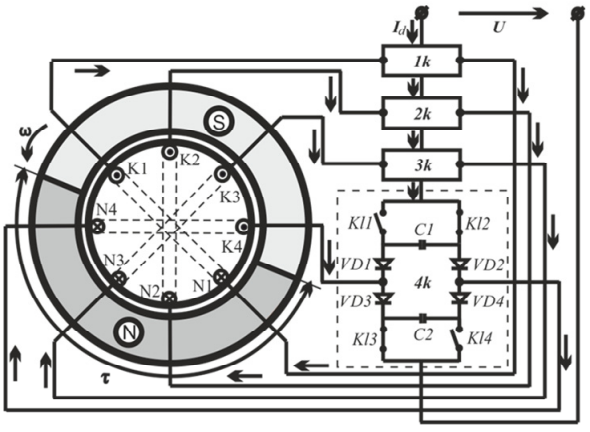

b

Fig. 1. Inertial energy storage:
a) battery design; *b*) EMECS scheme:
1 – vacuum casing; 2 – flywheel; 3 – ferromagnetic screen; 4 – permanent magnets; 5 – armature winding; 6 – stator housing; 7 – shaft; 8, 9 – bearing units; H, D – overall height and diameter of the storage device; R_{vn}, R_{nr} – inner, outer radii of the flywheel, h – height of the flywheel; ω – rotor speed; τ – pole division;
1*k*…4*k* – switches; *Kl1*, *Kl2*, *Kl3*, *Kl4* – keys;
VD1, *VD2*, *VD3*, *VD4* – diodes; *C1, C2* – capacitors;
I_d – source current; U – voltage at the terminals

The storage device parameters included in relations (1), (2) are determined by the shape and dimensions of its

rotor and stator, inductor excitation system, circuit and configuration of the armature winding, and the level of electromagnetic and mechanical loads of all the listed drive components.

The paper pays attention to establishing the connection of the parameters C_{mn}, C_{en}, L_n and R_n with the configuration, connection diagram and geometric dimensions of the armature winding.

The configuration and connection diagrams of the armature winding of EMECS. The armature winding, being the determining element of the EMECS of the storage device, must satisfy the following requirements:

- provide the specified values of load voltage and current at the terminals of the machine, corresponding to the required power;
- provide satisfactory conditions for changing the direction of current flow in phases, that is, the switching process;
- possess the necessary mechanical, electrical and thermal strength, with a minimum consumption of material, as well as manufacturability.

The main element of the armature winding here, as in conventional DC machines, is the section, which consists of one or a number of series-connected turns. The active sides of the section are located in two layers of slots under the poles of different polarity at a distance of pole division τ. According to the external shape of the contours, the windings can be wave and loop.

The sections of the windings having electric and magnetic symmetry, the adjacent sides of which are located in different layers of the same slot, connecting either counter-series or counter-parallel, form the phase of the winding. The connection diagram of the sections in the phase of the armature winding depends on the required voltage and current of the machine.

Each phase is connected as a load in the diagonal of the bridge current inverters, which, in turn, connected in series, form the armature winding.

For example, Fig. 2 shows the windings of the wave and loop types, the phases of which are formed by counter-sequential connection of sections. Here the ends of the sections *K*1, *K*2, *K*3, *K*4 are connected in series with the ends of the sections *K*5, *K*6, *K*7, *K*8, respectively, and the beginning of the sections *N*1 and *N*5, *N*2 and *N*6, *N*3 and *N*7, *N*4 and *N*8 are connected as a load to the diagonal of the inverters bridge type *1*, *2*, *3* and *4*, respectively.

In Fig. 3 windings of wave and loop types are shown, the phases of which are formed by counter-parallel connection of sections. Here, the beginnings of sections *N*1, *N*2, *N*3, *N*4 are combined into nodes by the ends of sections *K*5, *K*6, *K*7, *K*8, respectively, and the ends of sections *K*1, *K*2, *K*3, *K*4 also into nodes with the beginnings of sections *N*5, *N*6, *N*7, *N*8, respectively . By nodes *N*1 *K*5 and *K*1 *N*5, *N*2 *K*6 and *K*2 *N*6, *N*3 *K*7 and *K*3 *N*7, *N*4 *K*8 and *K*4 *N*8 the phases are connected as a load in the diagonal of bridge inverters *1*, *2*, *3* and *4*, respectively.

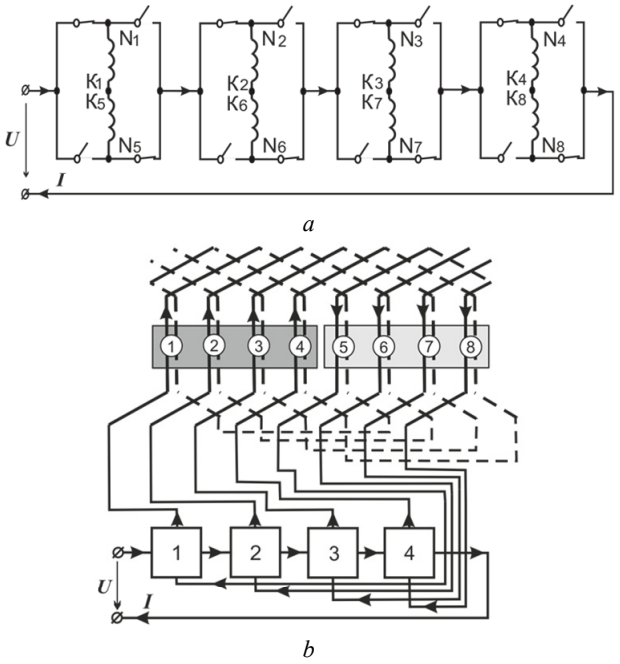

Fig. 2. Counter-series connection of phases (*a*), and wave type winding (*b*)

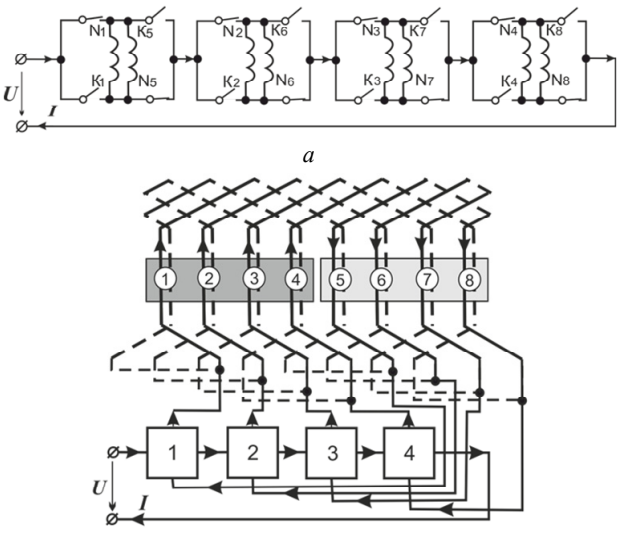

Fig. 3. Counter-parallel connection of phases (*a*), and loop type winding (*b*)

From the above circuits it is obvious that:

- circuits of winding made of sections of the wave and loop type, practically do not differ from each other;
- when phases are formed from sections at their serial connection, it is possible to obtain higher voltage at the input of the machine than with parallel connection, and with parallel connection – a higher current;
- the number of sections in the winding phase is determined by the number of poles of the machine.

Such winding connection circuits make it possible to regulate the voltage during the operation of the storage device by switching on and off the operating phases of the EMECS, as well as by changing the load angle θ.

Analytical determination of machine constants and electromagnetic parameters. The machine constant C_{en} is determined based on the expression for the

instantaneous value of the EMF induced in rectilinear conductors of length l_{ef} moving in the magnetic field with the value of B_{sr} with velocity V

$$e = 2B_{sr}l_{ef}V\,. \tag{3}$$

The effective conductor length here is determined by the formula

$$l_{ef} = \frac{2pwN_f l_a}{a}\,, \tag{4}$$

where $2p$ is the number of poles; w is the number of turns in the section; N_f is the number of phases; l_a is the active length of the armature winding; a is the number of parallel branches in phase.

Expressing the linear velocity V through the rotor speed n_n

$$V = \frac{p\tau n_n}{30}\,, \tag{5}$$

and substituting (4), (5) in (3), we obtain

$$e = \frac{0{,}13p^2wN_f\tau l_a}{a}B_{sr}n_n\sin\theta\,. \tag{6}$$

Relationship

$$C_{en} = \frac{2p^2wN_f\tau l_a}{15a}\,, \tag{7}$$

which is determined only by the geometric parameters of the machine and does not depend on the modes of its operation, we call the machine constant C_{en}.

The machine constant C_{mn} is determined from the expression for the electromagnetic torque

$$M_{em} = F_e\frac{D_a}{2}\,, \tag{8}$$

where D_a is the diameter of the armature; F_e is the equivalent force acting on an effective conductor of length l_e with current i_a in the magnetic field B_{sr}

$$F_e = B_{sr}l_e i_a\,, \tag{9}$$

where $i_a = I/a$ is the current in the parallel phase branch.

The effective conductor length is defined as

$$l_e = 2pwN_f l_a\,. \tag{10}$$

After substituting (10) and (9) into (8), we obtain

$$M_{em} = \frac{2pwN_f l_a D_a}{a}B_{sr}I\,. \tag{11}$$

Relationship

$$C_{mn} = \frac{2pwN_f l_a D_a}{a}\,, \tag{12}$$

determined only by the geometric parameters of the machine and independent of the modes of its operation, we call the machine constant C_{mn}.

The active resistance R_n and inductance L_n of the EMECS are determined by summing these parameters for individual phase elements, the equivalent circuits of which are shown in Fig. 4. Since the parameters indicated in this Figure significantly depend on the geometry of the winding sections, one of the important questions for us was the following: what calculation configuration to replace the real configuration of the section? We took a rectangle with sides $2a$ and $2b$ as the calculation configuration. Moreover, side $2b$ was taken equal to the pole division τ. The equivalence of the calculation configuration and the real one was provided by increasing the side of rectangle $2a$ by two lengths of the difference between the length of the frontal part of the armature winding l_b and the pole division τ

$$l_b = \frac{1}{2}\mathrm{tg}\left(\arcsin\frac{(\Delta_l + b_l)Z_P}{2\pi R_l}\right), \tag{13}$$

where Δ_l is the distance between the frontal parts of two adjacent coil sides; b_l is the width of the coil side in the frontal part; Z_P is the number of slots of the armature; R_l is the radius of the circle on which the frontal part of the winding is located.

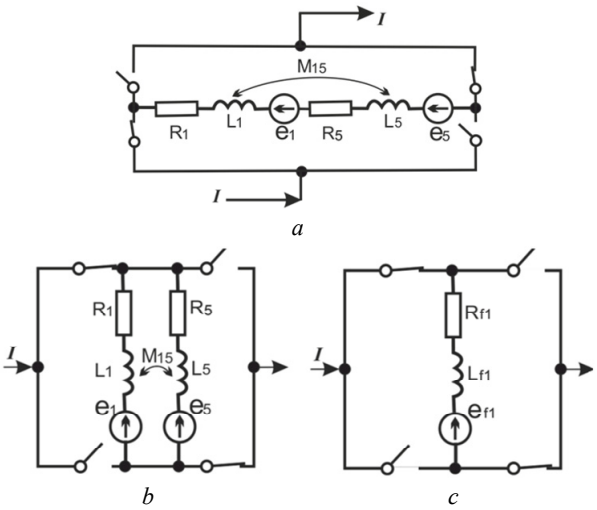

Fig. 4. Equivalent circuit of:
a – two winding sections connected in series and belonging to the same phase; *b* – two winding sections connected in parallel and belonging to the same phase;
c – phase winding; R_1, R_5 – active resistance of sections; L_1, L_5 –inductance of sections; e_1, e_5 – EMF of sections; M_{15} – mutual inductance of sections of one phase; R_{f1}, L_{f1}, e_{f1} – equivalent active resistance, inductance, EMF of the phase, respectively

Thus, to calculate the active resistance and inductance in the equivalent circuits of the armature winding, a rectangle with dimensions $2a\times2b$ was taken as a section. Side $2b$ was assumed equal to pole division, and side $2a$ was determined as the reduced length of the armature

$$l'_a = l_a + 2(l_b - \tau)\,. \tag{14}$$

The calculation of the active resistance for the armature winding at a parallel branches and cross-section s_a of the effective copper conductor of the winding with specific resistance ρ is carried out according to the following formula

$$R_n = \rho\frac{N_f 2pwl'_a}{s_a a^2}\,. \tag{15}$$

As for the inductance of both the phase and the winding as a whole, both the intrinsic and mutual inductances of the coils of the armature winding contribute to its value.

The winding phase inductance is determined as

$$L_f = N_k L_k + N_k\sum_{k=1}^{Nk-1}M_{k,k+Nf}\,, \tag{16}$$

where N_k is the number of coils in phase; L_k is the intrinsic inductance of the coil; $M_{k,k+Nf}$ is the mutual inductance of the coils in phase.

The intrinsic inductance of the coil is determined according to the formula

$$L_k = \frac{2\mu_0}{\pi} w^2 (a+b)\left[\ln\frac{8ab}{h_1+h_2} - \frac{b}{a+b}\times \right.$$
$$\times\left(0{,}693 + \ln\left(b+\sqrt{a^2+b^2}\right)\right) - \frac{a}{a+b}\times$$
$$\times\left(0{,}693 + \ln\left(a+\sqrt{a^2+b^2}\right)\right) + \frac{2\sqrt{a^2+b^2}}{a+b} - \quad (17)$$
$$\left. -0{,}5 + 0{,}224\frac{h_1+h_2}{a+b}\right];$$

where h_1 are h_2 are the height and width of the cross-section of the coil section; $\mu_0 = 4\pi\cdot10^{-7}$ H/m is the magnetic constant.

Parameters a and b are determined as:

$$a = \frac{l'_a}{2};\ b = \frac{\tau}{2}.$$

To find the mutual inductance of the winding coils, we represent them in the form of infinitely thin single-turn rectangular-shaped contours located in 3D space XYZ and offset from each other by a distance of x_s, y_s, z_s along the x, y, and z axes, respectively [7].

Connecting the beginning of the Cartesian coordinate system with the geometric center of the contour, which coincides with the middle turn of the first coil of the winding, and assuming that the position of the contour replacing the second coil of the winding is oriented according to the coordinates of its center, we find the mutual inductance between them according to

$$M_{15} = \frac{\mu_0}{4\pi}\oint_{l_1}\oint_{l_2}\frac{dl_1\cdot dl_2}{r}, \quad (18)$$

where l_1 and l_2 are the contours of the first and second winding coils, respectively; r is the distance between the elements dl_1 and dl_2 along the OZ axis.

We use the method of plots. Since the numerator of integrand (18) contains the scalar product of vectors, the terms corresponding to the interaction of the parallel sides of the contours l_1 и l_2 make a non-zero contribution to the mutual inductance. We represent the double contour integral as a sum

$$I = I^{(1)} + I^{(2)}, \quad (19)$$

where $I^{(1)}$ is the sum of the integrals over those rectilinear sections of the contours that are parallel to the x axis; $I^{(2)}$ is the sum of the integrals over the sections parallel to the y axis.

Taking into account the numbering of the contour sections, we can write

$$I^{(1)} = I_{11} + I_{12} + I_{22} + I_{21},$$
$$I^{(2)} = I_{33} + I_{34} + I_{44} + I_{43},$$

where I_{mn} are the integrals over rectilinear parallel sections of the contours, and here the index m corresponds to the number of the section of the contour of the first winding, and the index n corresponds to the number of the section of the second winding. All these integrals have a general form

$$I_{mn} = \int_{\alpha_1}^{\beta_1}\int_{\alpha_2}^{\beta_2}\frac{d\varepsilon_1\cdot d\varepsilon_2}{\sqrt{(\varepsilon_2-\varepsilon_1)^2+\Delta^2+Z^2}}, \quad (20)$$

where α_1, β_1, α_2, β_2 are the limits of integration; $\varepsilon_1=x_1$, $\varepsilon_2=x_2$ are the integration variables for sections parallel to the x axis; $\varepsilon_1=y_1$, $\varepsilon_2=y_2$ are the integration variables for sections parallel to the y axis; Δ – for sections parallel to the x axis is taken as the difference of the y coordinates, for sections parallel to the y axis is taken as the difference of the x coordinates.

Assuming that the distance along the Z axis between the coils is known and $\Gamma=\Delta^2+Z^2$, integral (20) can be represented as

$$I_{mn} = (\alpha_2-\alpha1)\ln\left[(\alpha_2-\alpha_1)+\sqrt{(\alpha_2-\alpha_1)^2+\Gamma}\right] - \sqrt{(\alpha_2-\alpha_1)^2+\Gamma} -$$
$$-(\alpha_2-\beta_1)\ln\left[(\alpha_2-\beta_1)+\sqrt{(\alpha_2-\beta_1)^2+\Gamma}\right] + \sqrt{(\alpha_2-\beta_1)^2+\Gamma} -$$
$$-(\beta_2-\beta_1)\ln\left[(\beta_2-\beta_1)+\sqrt{(\beta_2-\beta_1)^2+\Gamma}\right] + \sqrt{(\beta_2-\beta_1)^2+\Gamma} +$$
$$+(\beta_2-\alpha_1)\ln\left[(\beta_2-\alpha_1)+\sqrt{(\beta_2-\alpha_1)^2+\Gamma}\right] - \sqrt{(\beta_2-\alpha_1)^2+\Gamma}.$$

The limits of integration for the integrals I_{mn} are presented in Table 1, where k is the number of the integral.

Table 1

Integral parameter values

I_{mn}	α_1	β_1	α_2	β_2	Δ	k	j	Sign
I_{11}	$-a$	a	x_s-c	x_s+c	y_s+d-b	1	1	+
I_{12}	$-a$	a	x_s-c	x_s+c	y_s-d-b	2	1	–
I_{22}	$-a$	a	x_s-c	x_s+c	y_s-d+b	3	1	+
I_{21}	$-a$	a	x_s-c	x_s+c	y_s+d+b	4	1	–
I_{33}	$-b$	b	y_s-d	y_s+d	x_s-c+a	1	2	+
I_{34}	$-b$	b	y_s-d	y_s+d	x_s+c+a	2	2	–
I_{44}	$-b$	b	y_s-d	y_s+d	x_s+c-a	3	2	+
I_{43}	$-b$	b	y_s-d	y_s+d	x_s-c-a	4	2	–

In view of Table 1, instead of formula (18) we can write

$$M_{15} = \frac{\mu_0}{4\pi}\sum_{j=1}^{2}\sum_{k=1}^{4}(-1)^{k+1}I_k^{(j)}. \quad (21)$$

Based on the obtained relations, we find the terms of mutual inductances in formula (16) using the example of a four-phase two-pole machine with counter-parallel connection of the armature phase coils.

The magnetic coupling diagram of this winding is shown in Fig. 5,*a*. The mutual inductance between the sections of the winding is presented in the form of two components: slot M_{pch} and frontal M_{lch}. If the contribution of the slot part in the creation of mutual induction flows between the sections is obvious, then the contribution of the frontal parts is clearly illustrated in Fig. 5,*b*.

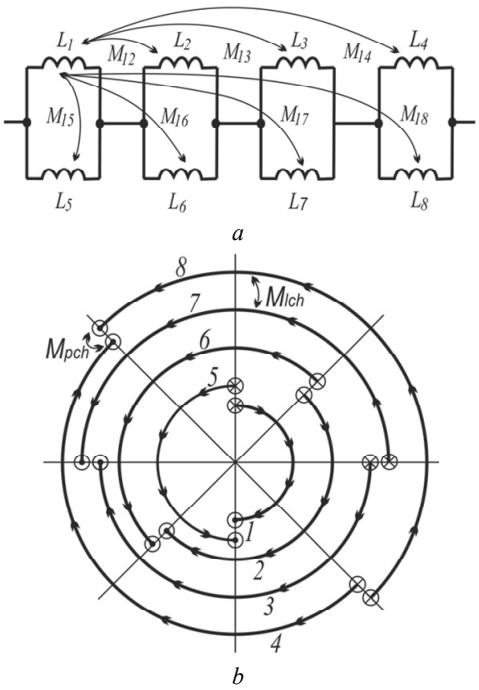

Fig. 5. Full magnetic connections of the coils of the armature winding (*a*), connections in the frontal parts (*b*)

Assuming that the proportion of mutual induction between the frontal parts of the sections is proportional to the length of their mutual overlap, we obtain the following results. Firstly, it is obvious that when finding the inductance of the armature winding phase, only the flows of mutual induction of the slot parts of adjacent coils are affected, and the frontal parts do not participate. Secondly, when finding the total inductance of one coil of the armature winding, the mutual induction coefficients of the frontal parts are compensated, and the total inductance of the coil is defined as

$$\begin{aligned} M_{1\Sigma} &= \frac{3}{4}M_{lch} - \frac{2}{4}M_{lch} + \frac{1}{4}M_{lch} + \\ &2M_{pch} - \frac{1}{4}M_{lch} - \frac{2}{4}M_{lch} - \frac{3}{4}M_{lch}. \\ M_{1\Sigma} &= 2M_{pch} \end{aligned} \tag{22}$$

As a result, for the case of counter-parallel and counter-series connection of the coils, the expressions of the equivalent phase inductance, respectively, take the form:

$$L_{fpr} = \frac{L_k + 2w^2 M_{pch}}{N_k}; \tag{23}$$

$$L_{fps} = N_k\left(L_k + 2w^2 M_{pch}\right). \tag{24}$$

Equivalent inductances of the winding of the machine as a whole with counter-series and counter-parallel connection of coils in phase, respectively, equal to:

$$L_{Mps} = N_f N_k\left(L_k + 2w^2 M_{pch}\right), \tag{25}$$

$$L_{Mpr} = \frac{N_f\left(L_k + 2w^2 M_{pch}\right)}{N_k}. \tag{26}$$

Results obtained. Using the example of a four-pole electric machine of a test storage device, it is proposed to establish a connection between the parameters of the machine constants C_{mn} and C_{en}, the inductance L_n and the active resistance R_n with the configuration, connection diagram, and geometric dimensions of the armature winding using the analytical expressions obtained above.

As the initial data for the IEMESD test model, we take the value of energy that is released during stopping electrodynamic braking of the ER2T electric train section, consisting of head and motor cars, weighing 117 tons from speed of 45 km/h to 0 km/h on a horizontal track section 675 m long. This value corresponds to the exchange energy of the designed storage system. For two traction motors, it is 5.2 MJ. The system of electromechanical energy conversion should provide the issuance and reception of electrical energy at maximum voltage of 700 V and rated current of 400 A.

Based on the level of exchange energy of the storage device and the installation volume allocated for the storage system on the rolling stock of a suburban electric train, we take the following geometric dimensions of the flywheel: the outer radius of the rotor is 0.225 m, the inner radius is 0.11 m, the height is 0.335 m. The rotor speed is 18550 rpm.

Based on the obtained relationships, geometric and electromagnetic parameters were found for the electromechanical energy conversion system of the test storage device. This is a four-pole machine with a loop winding, made according to the circuit of counter-series connection of coils in phase, with the following geometric parameters: diameter of the armature is 0.214 m; active armature length is 0.255 m; the number of phases is 4; the number of coils in phase is 4; the number of turns in the coil is 2; coil dimensions excluding the frontal part are 0.253×0.168 m; coil cross-section is 80 mm^2; «offset» of the frontal part of the coil is 0.075 m. The geometric constants C_{mn} и C_{en} are obtained: 1.75 m^2 and 0.182 m^2, respectively, as well as the active resistance of 0.005 Ω and the equivalent inductance of $3.05\cdot10^{-5}$ H.

When choosing the geometric dimensions and winding connection diagrams, it is necessary to be guided by the following: obtaining high voltage value is possible by forming phases from counter-series connected coils, and of significant current by their counter-parallel connection. If it is necessary to obtain the required power components, it is also possible to realize mixed connection of the coils in phase. The number of coils in the phase must be a multiple of the number of poles of the machine. In view of the fact that the stator does not contain ferromagnetic, the armature winding should be positioned closer to its outer surface, that is, to the source of the magnetic field.

Conclusions.

1. The developed mathematical model of the inertial electromechanical energy storage device reflects the relationship of its indicators of exchange energy and power with the geometric and electrophysical parameters of both the energy storage and the electromechanical converter system. A feature of the model is the operation of machine constants in determining the electromotive force and electromagnetic torque. The mathematical model allows further study of the operating modes of the inertial electromechanical energy storage device as part of

the traction drive in the braking and acceleration modes of the electric rolling stock.

2. A relationship has been established between the geometrical dimensions of the coils, as well as the circuits of their connection when forming the armature winding with such parameters as the values of machine constants, active resistance and inductance of both individual phases and the armature winding as a whole.

3. It is shown that obtaining the required power components (current and voltage) of the electromechanical energy conversion system is provided by the formation of phases from counter-series or from counter-parallel connected adjacent coils of the armature winding, the number of which in phase must be a multiple of the number of poles of the inductor.

4. The proposed specific winding connection circuits make it possible to regulate the voltage during the storage device operation by switching on and off the operating phases of the electromechanical energy conversion system, as well as by changing the load angle θ.

REFERENCES

1. Doki T., Takahara E., Yamada J. A study for electric double layer capacitor series connection for railway traction. *Proc. of IEE 2003 Japan Industry Appl. Soc. Conf*., 2003, vol. 3, pp. 179-182.

2. Sameshima H., Ogasa M., Yamamoto T. On-board characteristics of rechargeable lithium ion batteries for improving energy regenerative efficiency. *Quarterly Report of RTRI*, 2004, vol. 45, no. 2, pp. 45-52. **doi: 10.2219/rtriqr.45.45**.

3. Witthuhn M. Schwungradspeicher in Diesel triebfahrzeugen. *Elektrische bahnen*, 2002, no. 3, pp. 110-113. (Ger).

4. Lenhard D., Engel B., Langwost J., Söffker C. Elektrische Ausüstung des Triebyuges LIREX Baureihe 618/619 für DB Regio. *Elektrische Bahnen*, 2000, no. 8, pp. 279-289. (Ger).

5. Omelianenko V.I., Omelianenko G.V. Electromechanical energy converter of inertial storage for traction power supply networks. *Russian Electromechanics*, 2001, no. 4-5, pp. 67-74. (Rus).

6. Omelyanenko V.I., Ryabov E.S., Overyanova L.V. Local train with electromechanical inertial energy storage unit. *Vestnik VELNII*, 2014, no. 2(68), pp. 89-102. (Rus).

7. Dzenzerskii V.A., Omelianenko V.I., Vasiliev V.I., Matin V.I., Sergeev S.A. *Vysokoskorostnoi magnitnyi transport s elektrodinamicheskoi levitatsiei* [High-speed magnetic transport with electrodynamic levitation]. Kyiv, Fiz.-mat. i tekh. lit. Publ., 2001. 479 p. (Rus).

Received 17.09.2019

H.V. Omelianenko[1]*, Candidate of Technical Science, Associate Professor,*
L.V. Overianova[1]*, Candidate of Technical Science, Associate Professor,*
A.S. Maslii[2]*, Candidate of Technical Science, Associate Professor,*
[1] National Technical University «Kharkiv Polytechnic Institute», 2, Kyrpychova Str., Kharkiv, 61002, Ukraine,
e-mail: omeljanenkgalina@i.ua; overanova@ukr.net
[2] Ukrainian State University of Railway Transport, 7, Feierbakh Square, Kharkiv, 61050, Ukraine,
e-mail: a.masliy@ukr.net

How to cite this article:
Omelianenko H.V., Overianova L.V., Maslii A.S. Geometric and electrophysical parameters of armature winding of electromechanical converter of inertial energy storage for suburban trains. *Electrical engineering & electromechanics*, 2020, no.1, pp. 65-71. **doi: 10.20998/2074-272X.2020.1.11.**

Матеріали приймаються за адресою:
Кафедра "Електричні апарати", НТУ "ХПИ", вул. Кирпичова, 21, м. Харків, 61002, Україна
Електронні варіанти матеріалів по e-mail: a.m.grechko@gmail.com

Довідки за телефонами: +38 050 653 49 82 Клименко Борис Володимирович
+38 067 359 46 96 Гречко Олександр Михайлович

Передплатний індекс: 01216